This is to certify that the
dissertation entitled

Sensing and Manipulation in a Nano-Bio Environment Using
Atomic Force Microscopy Based Robotic System

presented by

Guangyong Li

has been accepted towards fulfillment
of the requirements for the

Ph.D. degree in Electrical Engineering

Major Professor's Signature

12/14/06

Date

DATE DUE	DATE DUE	DATE DUE

SENSING AND MANIPULATION IN A NANO-BIO ENVIRONMENT USING ATOMIC FORCE MICROSCOPY BASED ROBOTIC SYSTEM

By

Guangyong Li

A DISSERTATION

Submitted to
Michigan State University
in partial fulfillment of the requirements
for the degree of

DOCTOR OF PHILOSOPHY

Department of Electrical and Computer Engineering

2006

ABSTRACT

SENSING AND MANIPULATION IN A NANO-BIO ENVIRONMENT USING ATOMIC FORCE MICROSCOPY BASED ROBOTIC SYSTEM

By

Guangyong Li

Although manipulation of nano-entities by atomic force microscopy (AFM) has been studied for more than a decade, researchers are still afflicted with the lack of visual feedback during manipulation. In this research, by linking a haptic device to the AFM tip, an atomic force microscope is modified into a nano-robot that can manipulate objects on nanoscale. The operation of manipulation is assisted by an augmented reality interface that includes both force and visual feedback in real time. The force feedback is realized through the haptic device. The real-time visual feedback is achieved by locally updating the AFM image based on physical models and real-time force information as well as local scan information. During manipulation, an operator can control the tip motion and feel the real-time 3-D interaction forces and simultaneously observe the real-time changes of the nano-environment at video frame rate via the augmented reality interface. The AFM based nano-robotic system enhanced by augmented reality enables us to simultaneously image, sense, and manipulate nano-objects *in situ*. The nano-robotic system becomes an effective nano-assembly machine that can fabricate nano-devices and nano-sensors. The ability of AFM to work under liquid condition enables this nano-robotic system to operate surgery of single cell and manipulate bio-molecules on nanometer scale under living condition. This research also investigates the sensing ability of the AFM based nano-robotic system. By functionalizing the AFM tip with specific antibodies, the targeted

receptors on cells' membrane are able to be identified, recognized, and labelled. In this technique, antibodies are tethered to the AFM tip through a spacer to form a strong but flexible bond. Due to the flexibility of the spacer, the antibody bonded to the AFM tip has much more chances to interact with the antigen (receptor) on cells' surface. The single receptors can be easily identified by the phase image obtained from the interleave mode lift-up scan method. The success of this research work provides a useful tool to study locations, structures, and molecular dynamics of cellular membrane proteins with respect to their roles in drug effectiveness.

Curiosity is one of the permanent and certain characteristics of a vigorous mind.

Few things are impossible to diligence and skill. Great works are performed not by strength, but perseverance.

–Samuel Johnson

to my wife, my parents

ACKNOWLEDGMENTS

I would like to thank the dissertation committee chair Dr. Ning Xi for his guidance and assistance throughout the course of this study. He encouraged me to constantly strive for this research to be its best. I am grateful to his support during my study at Michigan State University that makes this dissertation possible. I would also like to thank dissertation committee member Dr. Donna H. Wang for her expertise, time, and laboratory resource. Appreciation is also extended to all other dissertation committee members Dr. Tim Hogan, Dr. Dean Aslam, and Dr. Fathi Salem for their assistance and insightful comments and suggestions.

Special thanks are given to Ms. Mengmeng Yu, Mr. Ali Saeed, and Mr. Mathew Prokos who participated in the development of the augmented reality interface. Without their efforts, this work would be much less shining. Special thanks are also given to Dr. Jianping Li who helped me prepare experimental samples. I would also like to acknowledge the help from my colleagues, Mr. Jiangbo Zhang and Dr. Heping Chen, who had worked with me in many experiments.

Finally, I would like to express my most profound appreciation to my wife Jin Su, who gives me constant support, understanding, encouragement, and an abundance of love. I deeply appreciate all that she has done for me.

TABLE OF CONTENTS

LIST OF FIGURES

CHAPTER 1

Introduction

1.1 Motivation

The advance of nanotechnology in the past decade has made the engineering of nano-devices and nano-systems possible. Eventually, nanometer-scale devices or systems will become prevalent in all aspects of our lives. For instance, implantable nano-electrical-mechanical-systems (NEMS) or artificial cells are envisioned to replace cells damaged by today's incurable diseases, and to extend human life expectancy. However, the cellular functional mechanism has to be fully understood before any artificial cells become possible. In last few decades, SEM (scanning electron microscope) and TEM (transmission electron microscope) have played important roles in the cellular study. Even today they are still the indispensable equipments for cellular research in most laboratories. For example, SEM can provide detailed morphological structures of the cells and TEM can obtain a finer morphological details and acquire the cellular information on molecular level.

Although EMs (electron microscopes) are the most powerful microscopes, their several disadvantages preclude their application in the cellular research from living

condition. For example, EMs need very high vacuum environment for proper operation; The sample of SEM has to be coated with a conductive layer to avoid the charge dwelling problem; And the sample of TEM has to be cut into thin sections to allow the electrons to pass through. These stringent requirements and destructive sample preparations make any sample examination by EMs in living condition impossible.

As we enter into the post-genomic era, increased attentions have been directed to characterization of structure and function of biomolecules. Understanding the location, structure, and molecular dynamics of these molecules is of fundamental importance to elucidate their functions. To gain insights into how these biomolecules operate, advanced technologies are required for gaining information on the level of single molecules. The atomic force microscope (AFM) [1] would be one of such novel tools for the task. AFM was initially developed as an instrument mainly used for surface science research. Research efforts in the past few years indicate that AFM is also a potentially powerful tool for biochemical and biological research especially in cellular biology [2]. Such rapid expansion of AFM application in cellular biology is ascribed to the fact that AFM offers several advantages over other conventional techniques used in biological study such as SEM and TEM. For instances, AFM is capable of working in several environments including air, vacuum, and liquid. Most importantly, it can study the cells when they are still alive. Figure 1.1 shows working range of several common techniques used in biomedical and biological research. The image resolution from AFM often exceeds that from SEM and parallels to that from TEM.

Besides its high resolving power in imaging, lenient demands on working condition, and few requirements for sample preparation, AFM has the most significant potential to become an operating tool that can perform the operation of single cell surgery.

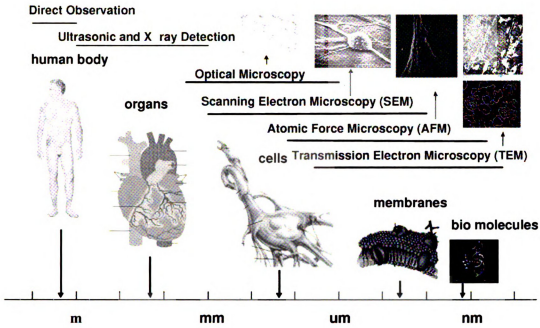

Figure 1.1. The working span of several common techniques used for biomedical research including OM (optical microscopy) SEM, AFM, and TEM.

Since the AFM tip is physically touching the sample during imaging, the AFM probe is equivalent to a robot arm with both sensing and manipulation functionalities.

The unique capability of AFM to directly observe single molecules in their native environments has provided insights into the interaction of proteins that form functionality assemblies. Although high-resolution images can provide some detailed conformal information of molecules, they may not provide information related to any specific protein. Because the interaction between ligands and receptors is highly specific and possesses a high degree of spatial and orientational specificity, the technique to functionalize an AFM tip with specific molecules makes investigation of single specific molecule possible. The modified AFM probe becomes specifically sensitive to the targeted molecules. It can be employed to recognize the individual bio-molecules *in situ* and observe their behaviors in living condition.

Combining its capability to distinguish specific bio-molecules *in situ* with its potential to modify the cell under living condition, the AFM could become the most powerful tool in cellular research ever. However, in order to implement these functionalities and integrate them together, many obstacles and snags have to be diagnosed and then either to remove them by improving the existing technology or to circumvent them by introducing new technology.

In this research, an AFM based nano-robotic system with both force and visual feedback is developed by introducing the augmented reality technology. The techniques for imaging living cells will be improved in order to achieve high resolution image of cells in living condition. A probe functionalization technique is also introduced with perspective to recognize the individual bio-molecules *in situ* under living condition. The ultimate goal is to construct an innovative tool that can perform both sensing and manipulation in a bio-nano environment under certain circumstances.

1.2 Review of Literature

AFM plays a very important role in the advance of nanotechnology. AFM is one of the major driving tools in nanotechnology research. It is not a coincidence between the emerging of AFM and the booming of nanotechnology. Its advent is one of the milestones in nanotechnology research.

The primary application of AFM is surface imaging. Its probe scans the surfaces of materials to produce topographical maps with lateral resolutions down to 0.3nm. The images from AFM are used to determine roughness, grain size, and features on the nanoscale. It can be used to investigate a wide range of materials, including

semiconductors, non-conducting surfaces, biological samples, high-resistivity materials, insulators, conducting samples, and features of microelectronic devices. Since its invention in 1986, enormous research has either concentrated on AFM itself or focused on its applications. Here, the literature germane to nanomanipulation, living cell imaging, and probe functionalization will be reviewed.

1.2.1 Nano-Manipulation

The major motivation for AFM based manipulation in recent studies is the imperative demand for suitable tools in fabrication of nanodevices. The conventional lithography is not possible to extend to the nanoscale due to the physical limitation, i.e., the size of the feature pattern is limited by the half wavelength of the ultraviolet used in the lithography, which is about 200nm.

Self-assembly is often considered as a possible solution for nanofabrication. During self-assembly molecules can join together through chemical bonding or small particles can aggregate through the van der Waals force or the electrical charge force [3]. However, only regular or symmetric patterns such as a monolayer can be fabricated from self-assembly. Further modification of the surface is not only necessary but also inevitable because many potential nano-structures and nano-devices have asymmetric patterns, which cannot be manufactured directly through self-assembly.

Recent AFM based studies show that AFM based nano-lithography is an alternative tool for the popular E-beam nano-lithography often used in fabrication of nanodevices and masks. AFM based nano-lithography includes dip-pen lithography [4], AFM tip-induced oxidation [5] and others. However, these techniques are limited by their low yield and inflexibility to materials. Many nanoscale materials with unique mechanical, electrical, optical, and chemical properties have a variety of po-

tential applications in nano-devices, nano-sensors, and NEMS. For instance, carbon nanotubes (CNTs) are such kind of materials that have drawn much attention during the last decade. In order to make these nanomaterials useful in nanotechnology applications, the ability to manipulate them in a controllable manner is fundamental and crucial. Unfortunately, manipulation of nanomaterials thus far has proven to be very difficult because there are only a few existing techniques to bring nano entities together and to assemble them into patterns as specified by a designer.

Nanomanipulation using AFM has attracted much attention among researchers since Eigler and Schweizer at IBM Almaden Laboratory demonstrated that they have positioned 35 Xenon (Xe) atoms to spell out the "IBM" pattern on a Nickel (111) surface using a STM (scanning tunneling microscope, a sibling of AFM) under ultra high vacuum and at very low temperature (about 4K) [6]. Various kinds of manipulation schemes have been developed in last decade. Using AFM, thin oxide structures have been rearranged on the underlying surface by increasing the applied load while scanning [7]. The sled-type motion of C_{60} islands during imaging has been studied in [8]. In [9], it was demonstrated that AFM can be used to deliberately move gold clusters on a smooth surface. Applications of AFM to manipulate and position nanometer-sized particles with nanometer precision were discussed in [10]. Using AFM to construct arbitrary patterns of gold nanoparticles was reported in [11]. However, all these results were obtained by playing with the existing AFM system without significant modification. It is not hard to imagine that these manipulation schemes are only conceptual demonstrations instead of real applications.

The AFM-based nanomanipulation is much more complicated and difficult than the AFM-based nano-lithography because it is not necessary to relocate the nano-objects on a surface in nano-lithography, while nano-objects have to be repositioned

by the AFM tip during nanomanipulation. An effective way to guarantee the success of manipulation is through an interactive way between the users and the atomic force microscope (AFM) images [11, 12]. The operator monitors the AFM scanning. A command is generated by the operator to push the nano-object as long as the tip pass through the object. Obviously, it is a slow process and very inefficient operation. The manipulation may fail quite often due to the position error caused by the deformation of the cantilever during manipulation. The experience of the operator is usually the major determining factor for the success of the manipulation.

By introducing a virtual environment of the samples, nanomanipulation using the AFM becomes easier. Besides 3-D synthetic visual feedback, a 1-DOF (degree of freedom) haptic device had also been constructed in [13] for haptic display. However, the 1-DOF force feedback may provide spurious force feeling because the manipulation force is mainly in the lateral direction instead of normal direction. In [14], the AFM is also connected to a Phantom^{TM} stylus (a haptic device form Sensable Inc.). In imaging mode, the topography data from AFM are sent to the Phantom^{TM}, and the operator can "feel" the topography of the sample. In manipulation mode, the Phantom^{TM} can be used to move the tip over the surface while keeping the internal normal force feedback on. However, it is still not clear whether the mapping from topography information to force information is helpful or not to the operation.

1.2.2 Imaging Living Cells

Atomic force microscopy has been proven to be an efficient and powerful technique for surface science research. Astonishingly, it has been extended to the more complex field of biology shortly after its advent. Research efforts in the past few years have made atomic force microscope a potential powerful tool for biological and biomedical research, especially for cellular biology. Unfortunately, the image formed by AFM

is based on the contact force between the tip and the sample, which is suitable for hard surface but inept at soft surface like cells.

Traditionally, the contact mode AFM (refer to Chapter 2 for details) was the most often routine. However, it suffers from several disadvantages: First, the normal force applied to the membrane results in large deformation of the cell, making it hard to obtain any high resolution images of living cells [15]. Second, lateral or shear force exerted by the tip causes surface features to be swept aside or smeared out [15]. Third, The AFM tip may be coated unevenly with nonrigid molecules associated with living cells including cellular debris, metabolic products, and cellular secretion in a highly uncontrollable and uneven fashion resulting in the deterioration of AFM image quality over time [16].

Several approaches have been investigated to obtain high resolution images of soft biological materials. Cells become stiff after chemical fixation [17]. However, this circumstance is not the living condition anymore. Although a high spatial resolution is possible, its significance is highly depreciated by its non-living nature. At low temperature, cells stiffen and high-resolution imaging becomes feasible [18]. The improvement in this condition is slim and this condition can hardly be called physiological. To reduce cell surface deformation and cantilever contamination in "authentic" physiological condition, the applied cantilever loading forces needs to be much smaller than what is available commercially, which remains as a current technical challenge. In [19], it was reported that it is possible to image living cells in contact mode with forces as low as 20-50 pN. In this range, indentation of the surface by the tip was generally less than 10 nm, giving access to the cell surface topography. However, detailed analysis reveals that it is impossible to maintained such a small contact force for stable imaging due to all kinds of unpredictable noise

and the slow response of AFM controllers.

Another solution is to use TMAFM (tapping mode AFM, refer to Chapter 2 for details) in liquid, which in theory gives a substantial improvement in imaging quality and stability over standard contact mode [20]. Due to viscoelastic properties of the plasma membrane, the cell may harden when responding to externally applied high frequency vibration and hence is less susceptible to deformation. Moreover, with this imaging mode, the cantilever oscillates at its resonant frequency and is only in intermittent contact with the cell surface. As a result, the destructive shear force is minimized [15]. In practice, the tip of an AFM tends to get more contaminated and lose resolution with time while operating in contact mode, especially when imaging adsorbable biological molecules. In contrast the tip tends to recover after picking up contaminants in the tapping mode. Presumably, the accumulated material is vibrated off or left on the surface when the tip taps. Therefore, high-resolution imaging of subcellular structures is theoretically feasible with the TMAFM.

However, submersion in a liquid significantly changes the oscillatory behavior of the cantilevers. For example, the resonance frequencies in water are lower than those in air by up to a factor of 5 for the most commonly used cantilevers; Quality factors in water are of order 1, compared with 10–100 in air [21]. The lowered and poorly defined resonance of cantilevers in aqueous solution makes high-resolution tapping mode imaging a technical challenge. While in principle tapping mode tends to minimize the tip-sample interaction force, contact mode in practice often provides better resolution for a given application such as when imaging relatively hard cells [22].

1.2.3 Single Receptor Recognition

Although membrane proteins are the main drug targets, the study of cell membrane proteins *in situ* on molecular level is difficult due to the current technical limitations. The recent development of atomic force microscopy (AFM) opens a new way to study the functionalities of cell membrane proteins. By immobilizing samples on a very flat surface such as mica, individual bio-molecules can be observed by AFM. For example, the major intrinsic proteins have been immobilized on a freshly cleaved mica surface by incubating with carboxypeptidase at room temperature overnight [23]. The mica surface was silanzied in a solution of 2% 3-aminopropy-trithoxysilane in toluene for 2 hours [24] or by exposing it to the vapor of 3-aminopropy-trithoxysilane for several minutes [25].

Although it is possible to observe the topographical image of membrane proteins in a well-prepared flat surface like mica, identification of distinct proteins only from the topographical information is challenging. The solution has to resort to functionalizing the AFM probe by certain kind of molecules such that the AFM probe possesses high sensitivity to specific molecules. Functionalization of AFM tips by chemically and biologically coating with molecules, e.g. biotin-avidin pairs [26, 27] and antigen-antibody pairs [28, 24], has opened a new research direction for studying interactions of molecules on the molecular level.

In their study in [26], a silicon nitride AFM tip was functionalized with avidin. By immobilizing the biotin on an agarose bead, the rupture force between the biotin from the bead and the avidin from the tip was measured using the force modulation mode (refer to Chapter 2 for details). When the tip was retracted, it detached from the surface in a series of discrete jumps with each corresponding to breakage of one or more biotin-avidin bindings. The total jump-off force was expected to

consist of an integral multiple of single rupture force. Therefore, by constructing a histogram of rupture forces, the single pair unbinding force was measured. The rupture force has been calibrated from 160 pN for avidin-bioton pair to 260 pN for streptavidin-biotin pair [29]. As understanding and interpretation of these initial studies on the measurements of rupture forces by AFM have improved, more investigators reproduced and extended the avidin-biotin findings by determining the bond strength of other examples of receptor-ligand pairs. These studies of AFM binding have been given an extensive overview by Willemensen et al [30].

Rupture forces representing biomolecular specific interactions can be exploited as a contrast parameter to create images in which the individual biomolecules can be recognized. It has been proven that single receptors can be recognized by an AFM tip functionalized with antibody through a force mapping technique [31, 30] on very flat surfaces such as mica. In their study, the functionalized tip was raster-scanned over the surface while a force-distance curve was generated for every pixel. From the force distance curve, the surface parameters such as stiffness and adhesion force was extracted either by online in real time or by off-line analysis. The individual receptors were recognized through these so called adhesion mode AFM. However, the adhesion AFM image obtained by this method has low lateral resolution and the work is extremely time-consuming.

Another way to recognize specific proteins like receptors is to use the tapping-mode phase imaging (refer to Chapter 2 for details). It can differentiate between areas with different properties regardless of their topographical nature [32, 33]. The phase angle is defined as the phase lag of the cantilever oscillation relative to the signal sent to the piezo driving the cantilever. Theoretical simulations and experiments of the cantilever dynamics in air have shown that phase contrast arises from differences in the energy

dissipation between the tip and the sample [32, 33]. The phase shift due to the tip-sample interaction, which involves energy dissipation, is the displacement of the non-contact solution to higher phase shifts and the periodic contact solution to lower phase shift values. The more dissipative features will appear lighter in the non-contact regime, whereas they will appear darker in the intermittent-contact regime [34]. When scanning the proteins immobilized on a mica surface using a tip functionalized with its antibody, the tip-sample interaction force will increase as the tip approaches the receptors, thus a significant change of the phase shift will be generated. Since the topographical information is also convoluted to the phase contrast image but with low frequency, a band-pass filter can be used to remove the low frequency topographical information and the high frequency noise. After filtering the phase contrast image, only the receptors' image will be left on the surface. Individual surface receptors have been identified on mica surface using these techniques [35, 36].

1.2.4 Summary

In conclusion, up to now there is no such kind of AFM based nanomanipulation system that can fabricate a single nanodevices or perform manipulation in a nano-bio environment. Achieving high resolution imaging of living cells is not only important for morphological study but also for cellular research on molecular level. However, it is hampered by several obstacles such as cell deformation and tip contamination as well as cell's mobile predisposition. Although individual proteins can be recognized efficiently through the tapping-mode phase imaging by a functionalized tip, biomolecules have to be extracted, purified, and attached to a flat and rigid surface. There are no reports that can detect membrane proteins directly in their native environments.

1.3 Objectives

The goal of this research is to develop an AFM based nano-robotic tool that can perform both sensing and manipulation in a nano-bio environment. In order to achieve this goal, at least two objectives have to be accomplished during the research. The first objective is to develop the nano-robotic system itself which can work in a nano environment and also be able to manipulate the objects in nanoscale size. The next objective is to further improve the system that is applicable to bio-samples in a nano-bio environment, in particular, under living condition. Besides its ability to manipulate nano-objects, to enable the AFM based nano-robotic system to sense bio-molecules is one part of the second objective of the research.

The first objective of this research is to develop a nano-robotic atomic force microscope that can manipulate nano-size entities. In this work, an AFM based nano-robotic system with enhanced augmented reality interface will be developed. By linking a haptic device to the AFM tip, which functions as an end-effector, an atomic force microscope can be modified into a nano-robot that can manipulate objects on nanoscale. A visual feedback based on the physical models and real-time force information can locally update the AFM image in real-time. During manipulation, an operator can control the tip motion and feel the real-time 3-D interaction forces through a haptic system and simultaneously observe the real-time changes of the nano-environment by the real-time visual feedback, which is updated at video frame rate. The real-time visual feedback and force feedback constitute the so-called augmented reality interface. The AFM based nano-robotic system assisted by the augmented reality will enable us to manipulate nano-materials precisely, efficiently, and eventually to fabricate nanodevices and nanosensors. The capability of AFM working under liquid condition makes this nano-robotic system possible on single cell surgery and manipulation of bio-molecules on nanometer scale, e.g. protein and

DNA levels.

Another objective of this research is to develop techniques that use the nano-robotic atomic force microscope to probe single membrane proteins *in situ*. In this work, a technique is going to be developed to recognize single specific receptors in their original location, cell membrane. By functionalizing the AFM tip with antibodies, AFM is able to identify specific types of receptors on cells' membrane. The antibody is tethered to the AFM tip through a spacer to form a strong but flexible binding. Due to the flexibility of the spacer, the antibody bond to the AFM tip has much more chance to interact with the antigen (receptor) on cell's surface. The single receptors can be easily identified by the phase image obtained from the interleave mode lift-up scan method. The success of this research work will provide a useful tool to study locations, structures, and molecular dynamics of cell membrane proteins with respect to their role in drug effectiveness.

1.4 Challenges and Problems

As stated in last section, the goal of this research is to developed an AFM based nano-robotic tool that can perform both sensing and manipulation in a nano-bio environment. In order to achieve the goal, both theoretical research and experimental studies need to be explored. The challenges and problems encountered in this research are addressed as follows.

1.4.1 Nano-Manipulation

In the first objective, an AFM based nano-robotic system is going to be developed. The main problem of previous AFM based manipulation schemes is the lack of real-time visual feedback. The main reason is that the AFM tip used for manip-

ulation is the same tip for imaging. Once it is being taken over for manipulation, there is no image updating anymore. Even though the image updating from AFM is available during manipulation, it is too slow to satisfy the real-time requirement. Therefore, each operation has to be verified by another new image scan before the next operation. Obviously, this scan-design-manipulation-scan cycle is time consuming and makes manipulation inefficient. Thus any methods which can update the AFM image as close as possible to the real environment in real time will help the operator to perform several operations without the need of a new image scan.

The system developed in this research will solve the visual feedback problem by an augmented reality interface which provides both real-time visual and force feedback. Although the force feedback is relatively easy considering AFM itself a force measurement tool, the visual feedback would be a formidable task. The imaging updating during manipulation has to highly rely on the real-time force information, the previously acquired knowledge, and the reliable system models. Namely, the real-time visual feedback during manipulation not only depends on the authentic real-time force information and accurate position control but also highly relies on the previously acquired knowledge of the working environment and the system models. Therefore, before manipulation, the nano-environment has to be analyzed first in order to extract information about the nano-environment as much as possible. The systems models should also be available for all kinds of nano-objects before manipulation. The following problems germane to real-time visual and force feedback need to be solved in accurate, reliable, and feasible manners:

- **Force Calibration and Compensation:** The interaction force applied on AFM tip is only measurable in two dimensions by the lateral channel and the normal channel of the photodiode detector of the AFM. The two-dimensional signal needs to map to three dimensions for force display. Due to the inconsistent

sensitivity of the two channels, the gain of each channel needs to be calibrated individually.

- **Position Compensation:** Due to the flexibility of AFM cantilevers, any manipulation force will cause the deformation of the cantilever, inevitably resulting in a tip position error. Without considering the position compensation, manipulation often fails.

- **Force and Position Transformation:** There are three coordinate spaces in the system: the working space of the AFM tip, the control space of the haptic joystick, and the display space of the visual feedback. All the information are transferred among these spaces back and forth, therefore, their relationship, namely, the transformation matrices have to be derived. The system should be able to accommodate to any situations, for example, different scanning angle and scanning range and etc.

- **Nano-Objects Identification:** In traditional manipulation schemes, the manipulation usually starts immediately after acquiring the first image of the nano-environment from AFM scanning. This could be the major reason for lacking real-time visual feedback during manipulation because they do not fully utilize the affluent information from the first image. By properly analyzing the the first image, abundant information are available, which includes the surface roughness as well as the characteristics and the location of every nano-object. All the pre-acquired information can be restored and retrieved for usage afterward.

- **Motion Behaviors of Nano-Objects**: Because different objects possess different propensities of motion behaviors, their behaviors have to be modelled within the tolerance of visual display. For example, a translational behavior model is usually sufficient to update a nano-particle in the visual feedback but both translational and rotational models are necessary to update a nano-rod in

the visual feedback. The motion behaviors for flexible materials such as carbon nanotubes and DNAs are even more complex.

- **Interaction among Tip, Surface, and Objects**: The behavior models of nano-objects only depict how the nano-objects move under manipulation but do not determine when the nano-objects are ready to move, i.e., how much force is needed to move them. The models of interaction among tip, surface, and objects will resolve this issue. Various situations have to be included in the models considering the varieties of motion behaviors of different nano-objects. For example, a nano-rod may prefer rolling to rotating around a pivot when the surface is flat enough.

1.4.2 Biomolecular Imaging

In another objective of this research, efforts are devoted to develop techniques that can use the nano-robotic atomic force microscope to probe single membrane proteins *in situ*. However, extension of the nano-robotic system into a nano-bio environment is not a trivial task. The softness of living cells makes any high resolution image impossible. Even though, single receptor is possible to be recognized on mica surface with functionalized probe, direct recognition from its original location (cell membrane) is hindered by the surface interference problem. Sensing bio-molecules in a nano-bio environment, especially under living conditions, needs to tackle several key issues as follows:

- **Cell Softness:** Because AFM is innately suitable for examining hard surface but unapt at scanning soft sample, it is extremely difficult to obtain high resolution image of living cells by AFM due to their softness. Without a high resolution image of living cells, any goal to study living cells on molecular level becomes impossible. Therefore, an innovative way to "fix" the cells without

killing them are not only necessary but also crucial in both theory and practice.

- **AFM Probe Functionalization:** The traditional AFM probes are adept in discerning the morphological difference but not capable of discriminating the biological or chemical dissimilarity. In order to improve the sensitivity of the probe to specific bio-molecules, the probe has to be functionalized with certain bio-molecules such as antibodies. The process usually involves lots of bio-chemistry, which is often a challenge for an electrical engineer. Previous research has shown that the antibody can be tethered to the AFM tip through a spacer to form a strong but flexible binding. Due to the flexibility of the spacer, the antibody bond to the AFM tip has much more chance to interact with the antigen (receptor) on cell's surface. The AFM probe now becomes more sensitive to a specific type of bio-molecules. The selectivity is determined by the antibody used in the functionalization.

- **Surface Interference:** With a functionalized probe, the AFM probe becomes more sensitive to certain bio-molecules on cell membrane. It makes the single receptor recognition *in situ* possible. However, difficulties often go beyond our anticipation. The surface interference during imaging is a major snag. The increased interaction between the functionalized tip and the targeted molecules are often submerged by the surface topography. It is not difficult to understand why most research work has to resort to mica which has a very flat surface.

1.5 Organization of This Dissertation

Chapter 2: This Chapter gives the preliminary knowledge of atomic force microscopy which is available elsewhere yet necessary for understanding the rest of the discussions. It includes the history of AFM, the principle of AFM, and the

various operating modes of AFM.

Chapter 3: In this chapter, an AFM based nano-robotic system enhanced by augmented reality is developed. The augmented reality enhanced nano-robotic system is implemented on an existing AFM system. Both visual and force feedback are realized in the system. In order to accurately display the force authentically, the interaction forces applied on tip have been well analyzed and the accurate force information is obtained after force compensation. In order for an accurate position control, a detailed analysis of cantilever deformation has been provided and the appropriate compensation algorithm has been given. All the necessary calibration techniques relevant to the force measurement and position compensation are also provided in this chapter.

Chapter 4: The application of the nano-robotic system to manipulate rigid nano-materials such as nano-particles and nano-rods is demonstrated in this chapter. The physical models for different nano-objects have been developed. Further analysis of the force interaction among tip, object, and sample surface is provided. After the force model is clear, the movement of the nano-objects under manipulation can be easily predicted based on their behavior models. All these models are finally used for implementation of visual feedback in the manipulation mode of the nano-robotic system.

Chapter 4: Further improvement of the reliability of the nano-robotic system by local scan is discussed in this chapter. The local scan strategies and scanning patterns are developed. The local scan has been implemented and intergraded into the manipulation module. The effectiveness of local scan has also been proved by experiments.

Chapter 6: Further application of the nano-robotic system to study properties of DNA molecules is discussed in this chapter. Using the nano-robotic system, the DNA molecules can be accurately positioned and easily modified by pushing, elongating, deforming and cutting. The electrical properties of single DNA molecules are primarily studied by bridging the nano-electrodes with DNA molecules through manipulation.

Chapter 7: In this chapter, the current techniques as well as challenges and difficulties in improving the imaging quality of living cells by AFM are discussed. An example of imaging neurons in living condition is presented. The perspective of the nano-robotic system in the operation of single cell surgery is also discussed.

Chapter 8: In this chapter, techniques and efforts using AFM to probe bio-molecules are introduced and reviewed. The state-of-art techniques for characterizing specific single receptor using the functionalized AFM tip are discussed. An example of studying the angiotensin II type 1 (AT1) receptors expressed in sensory neuronal cells by AFM with a functionalized tip is also given.

Chapter 9: This chapter concludes the research work and speculates the perspectives and potential applications of the nano-robotic system in future research.

CHAPTER 2

Introduction to Atomic Force Microscopy

2.1 Atomic Force Microscope

The atomic force microscope (AFM) is a very high-resolution type of scanning probe microscope (SPM). The AFM was invented by Binnig, Quate and Gerber in 1986 [1], and is one of the foremost tools for imaging and manipulation of matter on nanoscale. The AFM is being used to scan the surfaces of materials to produce topographical maps with lateral resolutions down to nanometer scale and normal resolutions down to atomic level. The images from AFM can determine roughness, grain size, and features of the sample on nanoscale. It is being used to solve processing and materials problems in a wide range of technologies affecting the electronics, telecommunications, biological, chemical, automotive, aerospace, and energy industries. The materials being investigated include thin and thick film coatings, ceramics, composites, glasses, synthetic and biological membranes, metals, polymers, and semiconductors. The AFM is being applied to studies on phenomena such as abrasion, adhesion, cleaning, corrosion, etching, friction, lubrication, plating,

and polishing. By using AFM one can not only image the surface in atomic resolution but also measure the force on nano-newton scale.

The first AFM was made by meticulously gluing a tiny shard of diamond onto one end of a tiny strip of gold foil. In the Fall of 1985, G. Binnig and C. Gerber used the cantilever to examine insulating surfaces. A small hook at the end of the cantilever was pressed against the surface while the sample was scanned beneath the tip. The force between tip and sample was measured by tracking the deflection of the cantilever. This was done by monitoring the tunnelling current of a second tip positioned above the cantilever. Although the design of this prototype is hardly used in today's AFM, it demonstrated the conceptual feasibility of the AFM.

In fact, without the breakthrough in tip manufacture, the AFM probably would have remained a curiosity in many research groups. It was T.R. Albrecht, a fresh graduate student, who first measured the atomic structure of boron nitride using AFM [37] and fabricated the first silicon micro-cantilever [38]. Today the tip-cantilever assembly typically is micro-fabricated from Si or Si_3N_4. After several years the micro-cantilevers have been perfected, and the instrument has been embraced by scientists and technologists. The first AFM used a scanning tunnelling microscope at the end of the cantilever to detect the bending of the lever, but now most AFMs employ an optical lever technique, a device that achieves resolution comparable to an interferometer while remaining inexpensive and easy to use [39, 40, 41].

In general, the AFM consists of a cantilever (probe) with a sharp tip at its end that is used to scan the specimen surface. The probe is typically silicon or silicon nitride with a tip radius of curvature on the order of nanometers. When the tip is brought into proximity of a sample surface, the force between the tip and the

sample leads to deflection of the cantilever according to Hooke's law. Typically, the deflection is measured using a laser spot reflected from the top of the cantilever into an array of photodiodes. If the tip is scanned at a constant height, there would be a risk that the tip would collide with the surface, causing damage. Hence, in most cases a feedback mechanism is employed to adjust the tip-to-sample distance to maintain a constant force between the tip and the sample. At each point, the feedback control signal is recorded. The surface topographical information can be reconstructed from the control signal.

There are two basic types of scanning mechanism. For a scanning stylus atomic force microscope, the probe tip scans above a stationary sample, while in a scanning sample design, the sample is scanned below a fixed probe tip. Figure 2.1 shows the mechanism of scanning sample AFM design. In this configuration, the sample is mounted on a piezoelectric tube, which can move the sample in the z direction for maintaining a constant force, and the x and y directions for scanning the sample. The resulting map of M(x,y) represents the topography of the sample. In the configuration of a scanning stylus atomic force microscope, the probe is mounted on a piezoelectric tube, which can move the tip in Z direction for maintaining a constant force, and the x and y directions for scanning the sample. This kind of configuration brings the benefit of less disturbance to the scanner because the AFM probe is very small while sample may be very big. It also brings another benefit to observe the transparent sample through a inverted optical microscope. The later discussions in this chapter are general to either design, as the relative motion of the tip to the sample is used to generate topographic images.

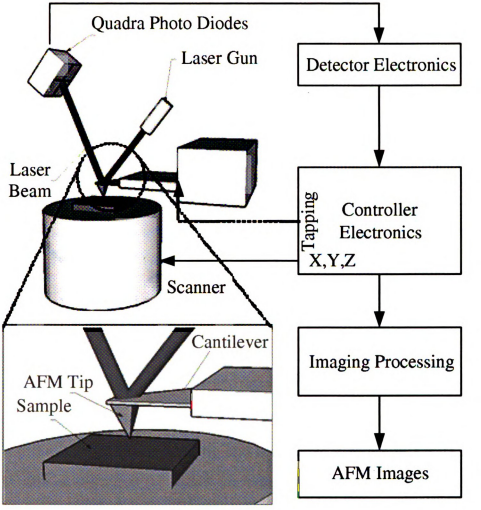

Figure 2.1. The scanning sample configuration of AFM. The scanning probe configuration is similar except that the AFM probe is mounted on the scanner and the sample is fixed.

2.2 Force Analysis of AFM Probe

Atomic force microscope is naturally a force measurement tool. It detects the deflection of the cantilever caused by the interaction between tip and sample surface. Several forces typically contribute to the deflection of an AFM cantilever.

The force most commonly associated with atomic force microscopy is an inter-

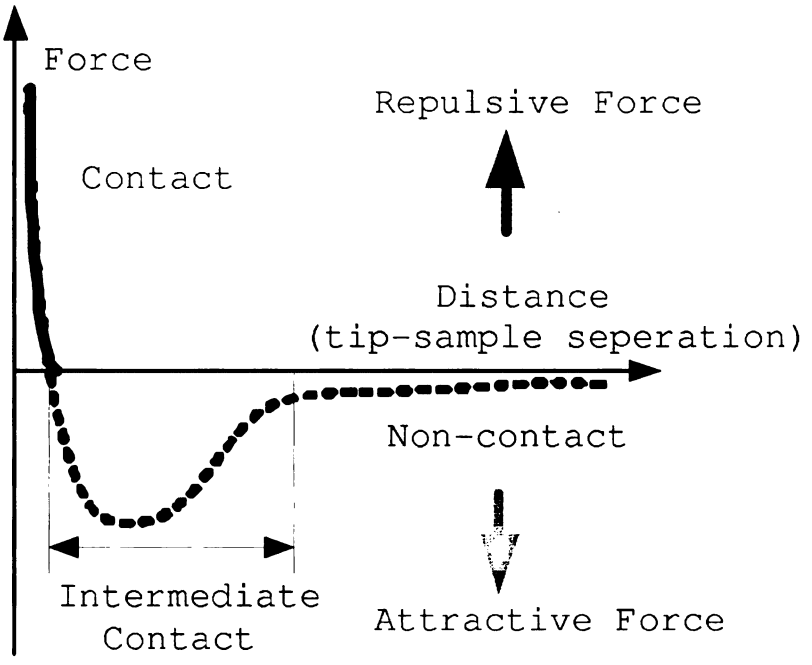

Figure 2.2. Interatomic force vs. distance curve.

atomic force called the van der Waals force. The dependence of the van der Waals force upon the distance between the tip and the sample is shown in Figure 2.2. At the right side of the curve the atoms are separated by a large distance. As the atoms are gradually brought together, they first weakly attract to each other. This attraction increases until the atoms are so close together that their electron clouds begin to repel each other electrostatically. This electrostatic repulsion progressively weakens the attractive force as the interatomic separation continues to decrease. The force goes to zero when the distance between the atoms reaches a couple of angstroms, about the length of a chemical bond. When the total van der Waals force becomes positive (repulsive), the atoms are theoretically in contact. The slope of the van der Waals curve is very steep in the repulsive or the contact regime. As a result, the repulsive van der Waals force balances almost any force that attempts to push the atoms closer together. In AFM this means that when the cantilever pushes the tip against the sample, the cantilever bends rather than force the tip

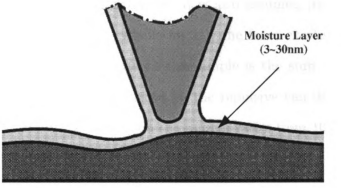

Figure 2.3. A layer of moisture with thickness of 3∼30nm adheres to the surfaces in ambient condition.

atoms closer to the sample atoms. Even if you design a very stiff cantilever to exert large forces on the sample, the interatomic separation between the tip and sample atoms is unlikely to decrease much. Instead, the sample surface is likely to deform.

In addition to the repulsive van der Waals force described above, two other forces are generally present during AFM operation: a capillary force exerted by the thin water layer often present in an ambient environment, and the force exerted by the cantilever itself. Under ambient conditions, sample surfaces are often covered by a layer of adsorbed gases consisting primarily of water vapor and nitrogen which is usually 3-30nm thick (much depending on the ambient condition and materials' surface properties) as shown in Figure 2.3. When the probe touches this contaminant layer, a meniscus forms and the cantilever is pulled by surface tension toward the sample surface. The magnitude of the force depends on the details of the probe geometry, but is typically on the order of 100 nano-Newtons. The capillary force is usually strong enough to hold the tip in contact with the surface.

The force exerted by the cantilever is like the force of a compressed spring. The magnitude and sign (repulsive or attractive) of the cantilever force depend upon the deflection of the cantilever and upon its spring constant. As long as the tip is in contact with the sample, the capillary force should be constant because the distance

between the tip and the sample is virtually incompressible. It is also assumed that the water layer is reasonably homogeneous. The variable force is the force exerted by the cantilever. The total force that the tip exerts on the sample is the sum of the capillary plus cantilever forces, and must be balanced by the repulsive van der Waals force. The magnitude of the total force exerted on the sample varies from 100 nanoNewtons, to the more typical operating range of 1~10 microNewtons.

2.3 AFM Operating Modes

Over the years, several modes of operation of AFM have been developed. The primary modes of operation are contact mode, intermediate contact (tapping) mode, noncontact mode, force modulation mode, and etc. More advanced modes are adding to the AFM technology and some of them have developed into new categories of SPMs such as Lateral Force Microscopy, Electrical and Magnetic Force Microscopy, and etc. Only the primary modes are going to be discussed here and the advanced modes are beyond the scope of this research.

2.3.1 Force Modulation Mode

The force modulation mode is to measure tip-surface interaction from plots of the deflection of the cantilever versus the extension of the piezoelectric scanner. These curves can be used to measure the vertical force that the tip applies to the sample surface and to study the surface properties of the sample. It is sometimes also called Force vs. Distance Curve. During force modulation mode, the scanner stops scanning but drives the tip to move up and down at the same location. The deflection of the cantilever is recorded versus the extension or retraction of the piezoelectric scanner in Z direction. The range of forces that can be measured depends on the stiffness of the cantilever used and can go from tens of pN to hundreds of nN.

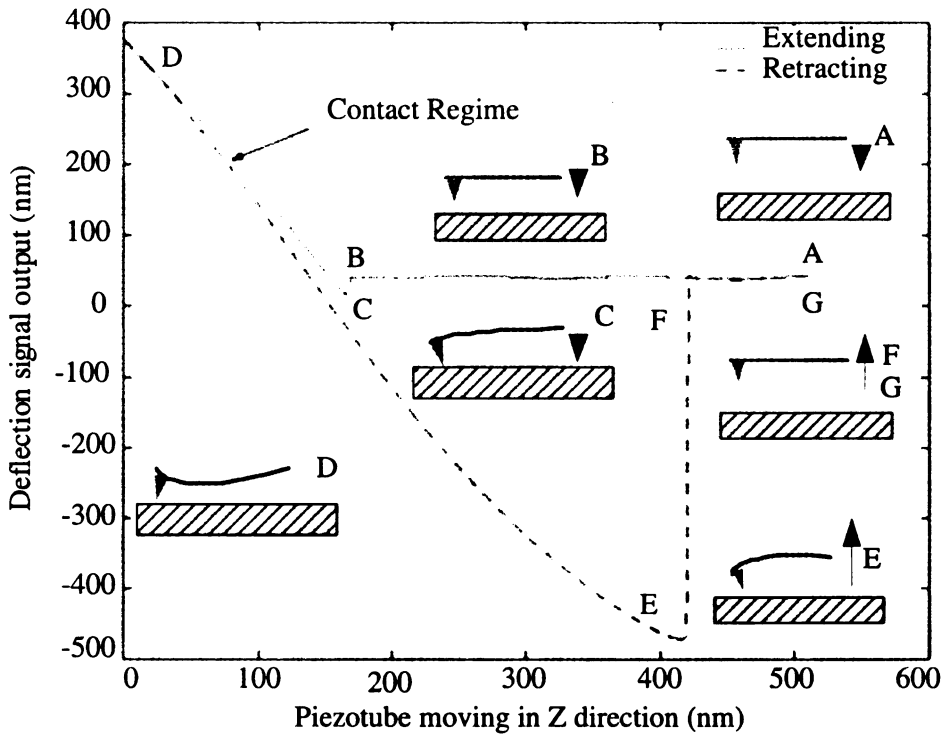

Figure 2.4. AFM force modulation curve

Figure 2.4 shows a typical force modulation mode curve (Force vs. Distance curve) obtained with a soft cantilever on a hard sample. In BC region, the 'jump to contact' is often due to capillary forces from the moisture layer that covers the tip and the sample surface (not present in vacuum). Segment EF shows the jump of the cantilever away from the surface, when the cantilever force exceeds the adhesive forces. The force of point E is the total adhesive force between the probe and the sample. Segments A to D are called the first half cycle of the curve while segments D to G are the second half cycle. The interaction force can be calculated from Equation (2.1) if the spring constant of the cantilever is known.

$$F = k\delta_z \tag{2.1}$$

where F is the normal force, k is the spring constant of the cantilever, and δ_z is the deflection.

2.3.2 Contact Mode

In the contact mode operation, the probe is essentially dragged across the sample surface while the force between the tip and the surface is kept constant during scanning. As the topography of the sample changes, the Z-scanner must move the relative position of the tip with respect to the sample to maintain this constant deflection. Using this feedback mechanism, the topography of the sample is thus mapped during scanning by assuming that the motion of the Z-scanner directly corresponds to the sample topography. To minimize the amount of applied force used to scan the sample, low spring constant ($k \leq 1$ N/m) probes are normally used. However, significant deformation and damage of soft samples (e.g., biological and polymeric materials) often occur in contact mode during imaging in air because significant force must be applied to overcome the effects of surface contamination (e.g., adsorbed moisture). The combination of a significant normal force, the lateral forces created by the dragging motion of the probe tip across the sample, and the small contact areas involved result in high contact stresses that can damage either the sample or the tip or both. To overcome this limitation, contact mode imaging can be performed within a liquid environment, which essentially eliminates problems due to surface moisture so that much lower contact forces can be used. In fact, the ability to image samples in a liquid environment is often a desirable capability of AFM.

From the contact mode scanning, not only a useful topographical map of the surface is obtainable, but another more vivid image, called error map, is also available, which usually contains more details of small features on the surface. The error map is engendered by the limited bandwidth of the control system. When the tip scans the

Figure 2.5. AFM images from contact mode scanning. The left is the topographical map regenerated from the control signal. The right is the error map recorded from the variation of cantilever deflection. The features on the surface are letters "NANOROBOT" inscribed on a polycarbonate surface by the AFM tip.

surface, the surface topography is like the input signal to the system that the control and actuation try to track. The smooth features are corresponding to low frequency signals to track and therefore they are easy to record into the topographical map, while the abrupt features equivalent to high frequency signals are difficult to follow and therefore they are filtered out from the topographical map. In this case, the trace of the cantilever motion does not exactly match the true surface topography, hence the mismatch is detected by variation of the cantilever deflection, which can be recorded into an error map. The error map turns out to be a vivid favorable image that contains the details of small feature on the surface. As shown in Figure 2.5, the error map on the right hand side is much more clear than the topographical map on the left hand side.

2.3.3 Non-contact Mode

To reduce or eliminate the damaging forces associated with contact mode, the cantilever can be oscillated near its first bending mode resonance frequency as the probe is raster scanned above the surface in either non-contact mode or tapping mode.

In non-contact mode, both the tip-sample separation and the oscillation amplitude are on the order of 1 nm to 10 nm, such that the tip oscillates just above the surface contamination layer, essentially imaging the surface of the adsorbed surface moisture. The resonance frequency and amplitude of the oscillating probe decrease as the sample surface is approached due to interactions with van der Waals and other long-range forces extending above the surface. These types of forces tend to be quite small relative to the repulsive forces encountered in contact mode. Either a constant amplitude or constant resonance frequency is maintained through a feedback loop with the scanner and, like in contact mode, the motion of the scanner is used to generate the topographic image. To reduce the tendency for the tip to be pulled down to the surface by attractive forces, the cantilever spring constant is normally much higher compared to contact mode cantilevers. The combination of weak forces affecting feedback and large spring constants causes the non-contact AFM signal to be small, which leads to unstable feedback and requires slower scan speeds than either contact mode or tapping mode. Also, the lateral resolution in non-contact mode is limited by the tip-sample separation and is normally lower than that in either contact mode or tapping mode. In practice, non-contact mode is rarely used considering its technical difficulties. However, it could be a potential solution for imaging very soft materials such as living cell's membrane.

2.3.4 Tapping Mode

The tapping mode is also called dynamic contact mode. Tapping mode tends to be more applicable to general imaging in air, particularly for soft samples, as the resolution is similar to contact mode while the forces applied to the sample are lower and less damaging. In fact, the only disadvantages of tapping mode comparing to contact mode are that the scan speeds are slightly slower and the AFM operation is a bit more complex, but these disadvantages tend to be outweighed by the advantages. In tapping mode, the cantilever oscillates close to its first bending mode resonance frequency, as in non-contact mode. However, the oscillation amplitude of the probe tip is much larger than that in non-contact mode, often in the range of 20 nm to 200 nm, and the tip makes contact with the sample for a short duration in each oscillation cycle. As the tip approaches the sample, the tip-sample interactions alter the amplitude, resonance frequency, and phase angle of the oscillating cantilever. During scanning, the amplitude at the operating frequency is maintained at a constant level (the set-point amplitude) by adjusting the relative position of the tip with respect to the sample. In general, the amplitude of oscillation during scanning should be large enough so that the probe maintains enough energy for the tip to tap through and back out of the surface contamination layer.

Similarly to contact mode scanning, the tapping mode scanning also generates an error map from the cantilever deflection, called TM deflection (total mean deflection, considering that the cantilever is oscillating). Besides the error map, there are more useful image varieties that can be extracted from the tapping mode scanning such as the amplitude image (a variation map of the cantilever oscillating amplitude) and the phase image (a phase lag map between the excitation signal to the cantilever and detected signal from the cantilever). These image types are more complex than the height map and the error map, and are usually difficult to interpret because they

not only relate to surface features but are also affected by the surface properties. Therefore, they are very useful imaging types when studying surface properties.

Tapping mode AFM is the most useful scanning mode for almost all the applications considering its less destructive effects on both samples and tips. The loosely attached nano-objects on the surface are often swept by the tip during contact mode scan but remain intact during tapping mode. Its manifold imaging type is another attractive feature for most users.

Schemes for non-contact and tapping mode operation include frequency modulation and the more common amplitude modulation. In frequency modulation, changes in the oscillation frequency provide information about a sample's characteristics. In amplitude modulation (better known as intermittent contact or tapping mode), changes in the oscillation amplitude yield topographic information about the sample. Additionally, changes in the phase of oscillation under tapping mode can be used to discriminate among different types of materials on the surface.

2.4 Discussions

The primary application of AFM is surface imaging. It scans the surfaces of materials to produce topographical maps with lateral resolutions down to 0.3nm. The images from AFM are used to determine roughness, grain size, and features on nanoscale. It can resolve individual holes, defects (such as pinholes), and atomic clusters. It can be used to investigate a wide range of materials, including semiconductors, non-conducting surfaces, biological samples, high-resistivity materials, insulators, conducting samples, and features of microelectronic devices.

The AFM has several advantages over the scanning electron microscope (SEM). The AFM can produce images of materials as small as 1nm, while the SEM is limited to around 20nm. For example, a single walled carbon nanotude can be facilely examined by AFM while SEM can only deals with the relatively large size multi-walled carbo nanotudes with strenuous efforts. Unlike the electron microscopes which provide a two-dimensional projection or a two-dimensional image of a sample, the AFM provides a true three-dimensional surface profile. Additionally, samples viewed by AFM do not require any special treatments (such as metal coating for SEM and thin sectioning for TEM) that would irreversibly change or damage the sample. While an electron microscope needs an expensive vacuum environment for proper operation, most AFM modes can work perfectly well in ambient air or even a liquid environment. This makes possible to study biological macromolecules and even living organisms.

The main disadvantage of AFM compared with the scanning electron microscope (SEM) is the image size. The SEM can image an area on the order of millimeters by millimeters with a depth of field on the order of millimeters. The AFM can only image a maximum height on the order of micrometers and a maximum scanning area of around 150 by 150 micrometers. At high resolution, the quality of an image is limited by the radius of curvature of the probe tip, and an incorrect choice of tip for the required resolution can lead to image artifacts, sometimes called tip convolution. The AFM also cannot scan images as fast as an SEM, requiring several minutes for a typical scan, while an SEM is capable of scanning at near real-time (although at relatively low quality) after the chamber is evacuated.

The AFM introduced in this chapter is mainly designed for general purpose of imaging. The AFM system in our lab is the so-called Bioscope (Veeco Instruments,

Inc.), which is mainly designed for imaging of bio-samples. It is equipped with a scanner with a maximum X×Y scan range of 90μm×90μm and a Z scan range of 5 μm. Peripheral devices include an optical microscope, a Charge Coupled Device (CCD) camera, and a signal access module through which most real-time signals inside the AFM system are accessible. The inverted optical microscope and the CCD camera help the operator to locate the tip, point the laser beam to the cantilever, and search for the interesting areas on samples. In next chapter, details on how to modify the existing AFM into a nano-robotic system will be provided. After a real-time visual feedback is added to the nano-robotic system, AFM will exceed SEM in most aspects.

CHAPTER 3

Development of AFM Based Nano-Robotic System

3.1 Introduction

Atomic force microscopy has been proven to be a powerful technique to study sample surfaces down to the nanometer scale. Not only can it characterize sample surfaces, it can also modify the sample surface through manipulation. Using atomic force microscope as a nanomanipulation tool is first motivated by the imperative demand for suitable tools in nano-fabrication. However, its lack of real-time visual feedback during manipulation has hindered its wide application.

Most previous nanomanipulation schemes using AFM are operated in a "blind" way. The manipulation pathes of each operation are designed either off line or by an interactive way based on a static AFM image. And then the pathes are downloaded to the AFM system to accomplish the operation in open loop. Whether the operation is successful or not has to be verified by a new image scan. Combining the AFM with virtual reality interface and haptic devices may facilitate the nanomanipulation

by removing the requirement of off-line design, but the operator is still blind. It is because he/she cannot see the real-time changes of the environment through the static virtual reality display even though he/she can feel the tip-surface-object interaction during operation. Therefore, a new image scan is still necessary after each operation. Since the nano-objects can be easily lost or moved to wrong destinations using these schemes, the result of each operation has to be verified by a new image scan before the next operation starts. Obviously, this scan-design-manipulation-scan cycle is very time consuming and inefficient because it usually takes several minutes to obtain a new AFM image. Thus any method which can update the AFM image as close as possible to the real environment in real time will help the operator to perform several operations without the need of a new image scan.

Fortunately, this barrier can be circumvented by the AFM based nano-robotic system developed in this chapter. The nano-robotic system is enhanced by an augmented reality interface, through which not only can the operator feel the real-time 3-D interaction forces but also observe the real-time changes of the nano-environment during nanomanipulation. The augmented reality interface helps the operator to perform several operations without the need of a new image scan, which makes the AFM based nano-assembly feasible and applicable. Because the AFM is capable of operating under liquid condition, the application of the AFM based nano-robotic system can extend to manipulation of bio-nano-entities in their physiological environments. In this chapter, the details to develop the AFM based nano-robotic system are discussed.

3.2 Architecture of the Nano-Robotic System

The main feature of the AFM based nano-robotic system developed in this chapter is the augmented reality interface. The augmented reality interface aims to provide

the operator with both real-time force feedback and real-time visual feedback during manipulation. The mechanism of the nano-robotic system is shown in Figure 3.1. It includes two subsystems which are connected through Ethernet: the AFM system and the augmented reality system.

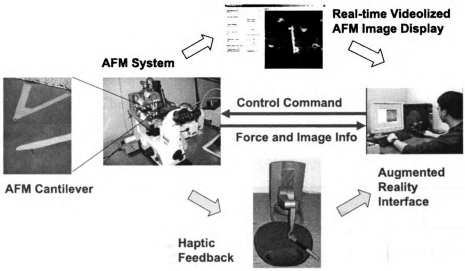

Figure 3.1. The AFM based nano-robotic system. Left: the AFM system including other accessories for imaging functions; Right: the augmented reality interface providing an environment for an operator to simultaneously control the tip motion through a haptic joystick, view the real-time AFM image, and feel the real-time force during manipulation.

The AFM system (Bioscope, Veeco Instruments) is equipped with a scanner with a maximum X×Y scan range of 90μm×90μm and a Z scan range of 5 μm. Peripheral devices include an optical microscope, a Charge Coupled Device (CCD) camera, and a signal access module through which most real-time signals inside the AFM system are accessible. The inverted optical microscope and the CCD camera help the operator to locate the tip, point the laser beam to the cantilever, and search for the interesting areas on samples. The augmented reality interface is generated by a computer with a haptic device (Phantom^{TM} from Sensable

Co.) installed. Through the signal access module, the signals of the deflection and the twisting of the cantilever flow directly into an A/D convertor card inside another computer. The augmented reality interface provides enhanced media for the operator to view the real-time AFM image at video frame rate and feel the force feedback during nanomanipulation. The real-time visual display is a dynamic AFM image of the operating environment which is locally updated based on the pre-acquired environment information, tip-subject interaction model, nano-objects behavior models (refer to Chapter 4), real-time force information, and local scanning information (refer to Chapter 5). Figure 3.2 illustrates how the system updates the AFM image in real time.

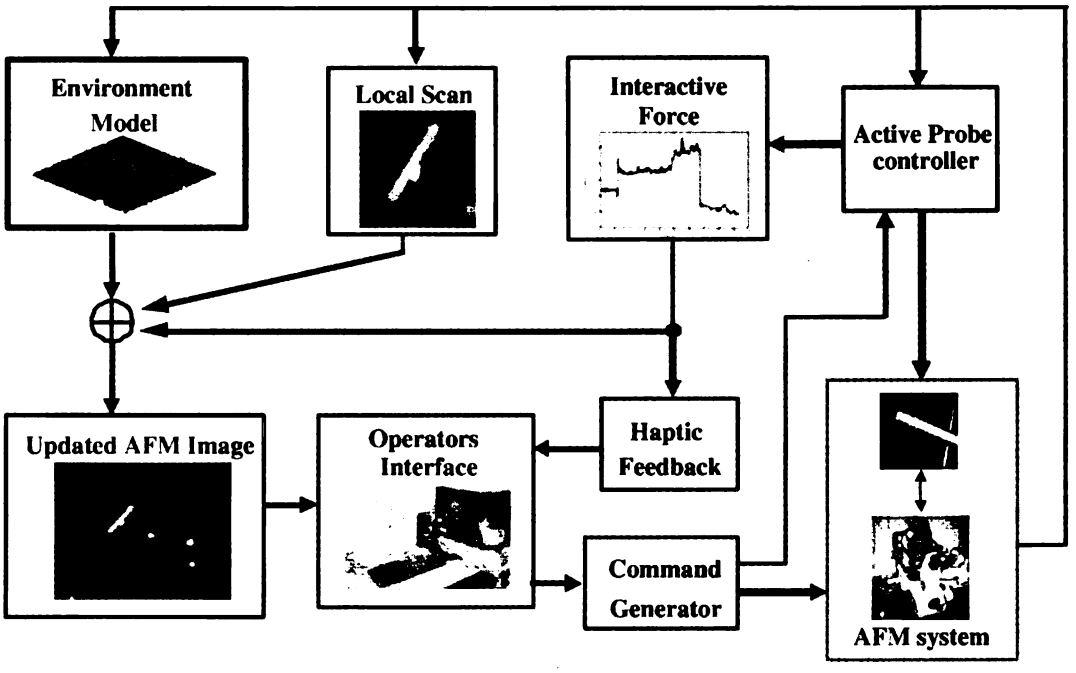

Figure 3.2. The augmented reality system: The bottom right is the AFM system, which includes other accessories for imaging functions; The others are the augmented reality environment which includes the augmented reality interface in the bottom middle and the necessary components for visual feedback.

In order to display the forces with high fidelity, a model of cantilever-tip

interaction with the surface has been developed in Section 3.4. The 3-D interaction forces on the tip are derived from the AFM normal and lateral force signals. Because of the existence of spurious signals in the system during manipulation, an algorithm for force signal compensation is provided in Section 3.5. After compensation, the 3-D force information is fed to the haptic joystick and image updating program. The operator can then feel three dimensional forces which are proportional to the actual forces acting on the cantilever tip. The visual display program also uses this authentic force signal to estimate the motion of nano-objects from their behavior models, which are going to be discussed in next chapter.

As shown in Figure 3.3, the augmented reality interface consists of both real-time force and visual feedback. A haptic device (Desktop Phantom^{TM}, Sensable) serves as the force feedback device. It displays the real-time force information measured from the data acquisition card (NI-DAQ 6104, National Instruments). The Phantom^{TM} also works as a joystick, through which the operator can input the position command. The visual interface is split into two windows. One window is designed for the command and parameters input as well as the locally updated real-time AFM image in two dimensions. The two dimensional image, as shown in the left of Figure 3.3, provides an accurate tip position display relative to the surface on the working plane. The other window, as shown in the right side of Figure 3.3, is the three dimensional display of the real-time AFM image, which is developed based on OpenGL graphic technology. The three dimensional display provides a reality interface, which can emulate the work environment more precisely and vividly.

Before starting the manipulation, a complete AFM image of the working area has to be captured and exported to the augmented reality interface. The AFM image can be displayed in the interface in two dimensions and three dimensions. After loading

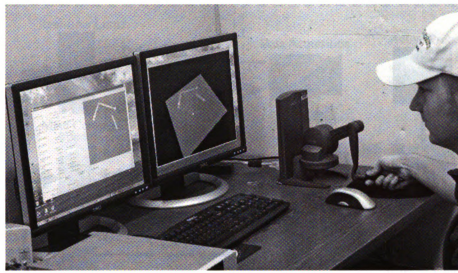

Figure 3.3. The augmented reality enhanced interface.

the file, the augmented reality interface obtains all parameters from the file such as scanning range and scanning angle. After loading the file, an object identification process starts running in order to recognize all the nano-objects and obstacles in the working area and label them correctly. The object identification process is based on an adjustable cutting plane. Anything above the cut plane is considered either as objects or obstacles depending on their size and shape. After the object identification process has been completed, all the information about the nano-objects and the obstacles such as the size and shape are stored and can be retrieved for the real-time image updating during manipulation afterward.

3.3 System Implementation

The implementation mainly includes hardware setup and software development, which are addressed below one by one.

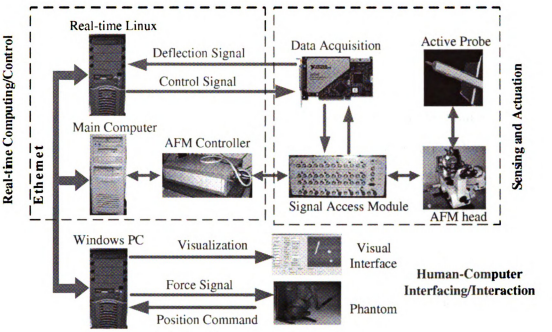

Figure 3.4. The hardware architecture of the AFM based nano-robotic system

3.3.1 Hardware Setup

The hardware architecture of the nano-robotic system is shown in Figure 3.4. The nano-robotic system consists of an existing AFM system, a real-time control module, and a human-computer interface module. The existing AFM system includes a AFM computer, a AFM controller, a signal access module (Veeco Inc., more information available at http://www.veeco.com), and a AFM scanner head. The real-time control module includes a real-time client computer (running on real-time Linux) in which a data acquisition card (National Instruments Inc., more information available at http://www.ni.com) is installed. The human-computer interface module mainly includes a haptic device (Desktop Phantom^{TM} from Sensable Co., more information available at http://www.sensable.com) and an interface client computer (running on Windows XP). The AFM computer is running as a server. The signal flows are also indicated in Figure 3.4. The hardware setup can also be viewed as three modules as shown in Figure 3.4: the real-time computing and control modules, the sensing and

actuation module, and the human-computer interface and interaction module.

3.3.2 Software Development

The interface program was conceived such that the majority of the image data are processed on the interface client computer. The real-time control algorithm and data acquisition are running on the real-time Linux computer. This allows the interface client computer with a computing load as low as possible and the real-time control computer with maximum sampling rate.

The two dimensional display as well as the command user interface is developed based on MFC (Microsoft Foundation Class) as shown in Figure 3.5. Information from the NanoScope software (Veeco Inc.) is exported into ASCII text file format. The three dimensional display is developed by OpenGL graphic technology as shown in Figure 3.6.

For a fully functional system, the force feedback and visual feedback are critical modules in the program. Although the force feedback is relatively easy to implement considering AFM itself a force measurement tool, the visual feedback would be very difficult to achieve. The imaging updating has to rely highly on the real-time force information, the previously acquired knowledge, and the reliable system models. Therefore, a lot of technical details have to be resolved one by one. As stated in Chapter 1, the major problems germane to the force feedback and visual feedback are: force calibration and compensation, position control and compensation, force and position transformation, motion behavior models of nano-objects, and interaction among tip, surface, and objects. This chapter mainly focus on the first three problems while the last two will be solved in next chapter.

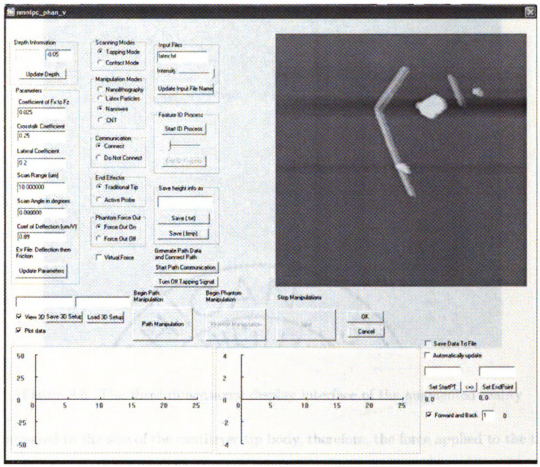

Figure 3.5. The two dimensional display interface of the augmented reality

3.4 Measurement of 3-D Interactive Forces on the Cantilever-Tip

3.4.1 Force Measurement

The objects under manipulation are usually nanoparticles or nanotubes with diameter from tens of nanometer to hundreds of nanometer. The tip height is usually several microns. The tip apex diameter ranges from several nanometer to tens of nanometer. Therefore, the size of nano-objects is usually larger than the tip apex but smaller than the tip body. Since the size of the objects under manipulation is usually small

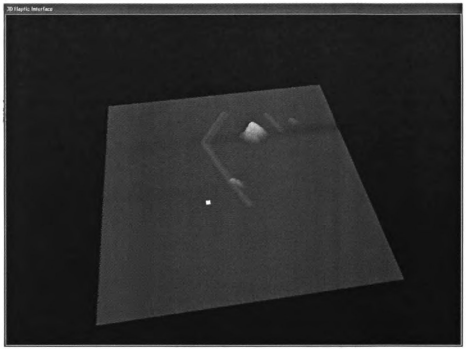

Figure 3.6. The three dimensional display interface of the augmented reality

compared to the size of the cantilever-tip body, therefore, the force applied to the tip by the object can be considered as a point force on the tip apex. The normal force applied to the AFM tip can be calculated from cantilever deflection according to the spring model of the cantilever,

$$F_n = k\delta_z \tag{3.1}$$

where F_n is the pseudo normal force which is defined in Equation (3.5), k is the spring constant of the cantilever, and δ_z is the deflection. Once the deflection and spring constant are known, the normal force can be calculated.

Suppose 3-D forces (F_x, F_y, F_z) are applied to the tip apex as shown in Figure 3.7. These forces engender 3-D torques (τ_x, τ_y, τ_z) on the cantilever with respect to point

O

$$\begin{cases} \tau_x &= F_y h \\ \tau_y &= -F_z l - F_x h \\ \tau_z &= F_y l \end{cases} \tag{3.2}$$

where τ_x causes the cantilever end to twist at an angle θ_x along X axis; τ_y causes the cantilever to bend δ_z in Z direction; and τ_z causes the cantilever to bend δ_y in Y direction.

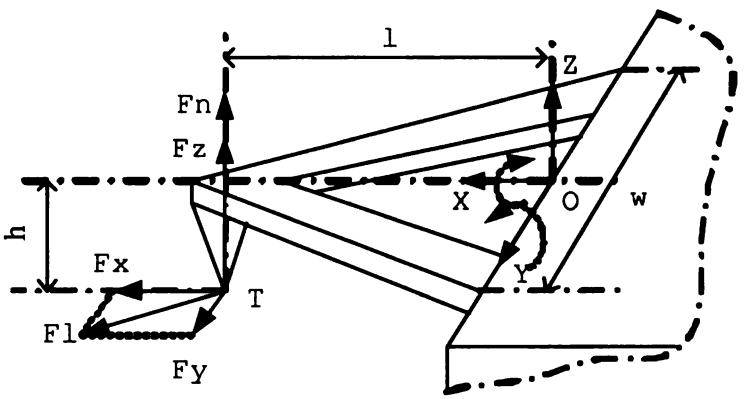

Figure 3.7. The force analysis model of the cantilever: O is the origin of the cantilever frame; w and l are the cantilever width and length respectively; h is tip height which includes the thickness of the cantilever; l is the cantilever length; T is the tip apex.

Using the quad-photodiode detector as shown in Figure 3.8, θ_x and δ_z are obtain-

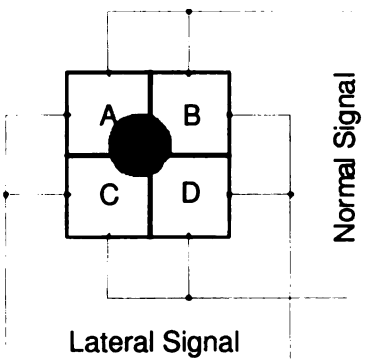

Figure 3.8. The quad-photodiode detector: A, B, C, and D are the signal output of the quad photodiodes

able by (3.3) and (3.4), while δ_y is not measurable,

$$\theta_x = K_l S_l \tag{3.3}$$

$$\delta_z = K_n S_n \tag{3.4}$$

where K_l and K_n are system constants that need to be calibrated, S_n and S_l are the normal signal and lateral signal outputs which are obtained as follows:

$$S_n = \frac{(A+B)-(C+D)}{A+B+C+D} \text{ and } S_l = \frac{(A+C)-(B+D)}{A+B+C+D}$$

K_n can be easily obtained by finding the slope of the force curve in contact region [42], while calibration of K_l is a very difficult task. Since τ_y is caused by both F_z and F_x, a pseudo force F_n along z direction as shown in Figure 3.7 can be defined such that

$$F_n = -\frac{\tau_y}{l} = F_z + \frac{h}{l}F_x \tag{3.5}$$

then according to (3.1) and (3.4), this pseudo force is the normal force measured by

$$F_n = kK_n S_n \tag{3.6}$$

The relationship between the AFM frame and the cantilever frame is determined by following rotational matrix

$$R = \begin{bmatrix} -\cos\psi & \sin\psi & 0 \\ -\sin\psi & -\cos\psi & 0 \\ 0 & 0 & 1 \end{bmatrix} \tag{3.7}$$

where ψ is the scanning angle during imaging. If the tip motion direction in the AFM frame is known as $\vec{V}_{AFM}$, its motion direction in the cantilever frame can be found as

$$\vec{V}_c = R\vec{V}_{AFM}$$

Suppose the tip lateral motion direction has an angle ϕ with respect to the X-axis of the cantilever frame, then the lateral force, F_l, must be opposite to the direction of the tip motion and its amplitude can be found by

$$F_l = F_y / \sin\phi \tag{3.8}$$

where F_y is measured by

$$F_y = \frac{k_l}{h}\theta_x = \frac{k_l K_l}{h} S_l \tag{3.9}$$

here, k_l is the torsional constant of the cantilever. The lateral force in X direction can be calculated by

$$F_x = F_y \tan\phi \tag{3.10}$$

Clearly, when $\phi = 0$, namely the tip motion along X direction in cantilever frame, $F_y = 0$ and F_x becomes unmeasurable in this case. In practice, the force display has to be bounded in order to avoid abnormal force feeling in this singular direction. In summary, the 3-D interaction force on tip in cantilever frame can be measured from the normal and lateral signal by the following equations

$$\begin{cases} F_y &= \frac{k_l K_l}{h} S_l \\ F_x &= -F_y \mathrm{ctan}\phi \\ F_z &= kK_n S_n - \frac{h}{l} F_x \end{cases} \tag{3.11}$$

Then the 3-D forces represented in AFM frame are

$$[F_{px}, F_{py}, F_{pz}]^T = R^{-1}[F_x, F_y, F_z]^T \tag{3.12}$$

By feeding the 3-D forces $[F_{px}, F_{py}, F_{pz}]^T$ to a haptic device, the operator can feel the forces, which are proportional to the actual forces acting on the cantilever.

From Equations (3.6) and (3.9), it is clear that the spring and torsion constants k and k_l, and the system constants K_n and K_l must be calibrated in order to obtain the actual forces acting on the tip by measuring the deflection signal from the quad-photodiodes array. The spring constant k is usually provided by manufacturer or can be calibrated experimentally [43, 44], and the system constant K_n can be calibrated (see Section 3.4.2). Although k_l and K_l cannot be obtained separately, their product, $(k_l K_l/h)$ is obtainable by directly calibrating the relation between the

lateral force and the normal force [45]. There are at least three calibration techniques available now [46, 47, 48]. A simpler method is used in this chapter to calibrated the product $(k_l K_l/h)$..

3.4.2 Calibration of Signal Gain in Normal Direction

The spring constant of the cantilever is usually provided by the manufacture or can be calibrated using several methods [43, 44]. The cantilever used here is standard micro-fabricated V-shaped cantilevers in 200 μm long with 3μm tip height. The spring constant provided by the manufacture is 0.12N/m.

The normal force applied to the AFM tip can be calculated from cantilever deflection according to (3.1. Once the deflection and spring constant are known, the normal force can be calculated. When the tip only move along Z direction, the lateral force becomes zero ($F_x = F_y = 0$). From Equation (3.11) and noting that $F_n = F_z$ in this case, it can be seen that

$$F_z = kK_nS_n$$

therefore, the deflection δ_z can be obtained from the normal signal output as

$$\delta_z = K_nS_n \ : \ K_n = \frac{d\delta_z}{dS_n} \tag{3.13}$$

When the tip contacts a hard surface but the piezo-tube keeps moving down, the change of the cantilever deflection is exactly the same as the movement of the piezo-tube. Therefore, the signal gain in normal direction, K_n, is obtained by finding the slope of the contact region in the force calibration mode of AFM as shown in Figure 3.9. For this cantilever, $K_n = 89$ nm/V.

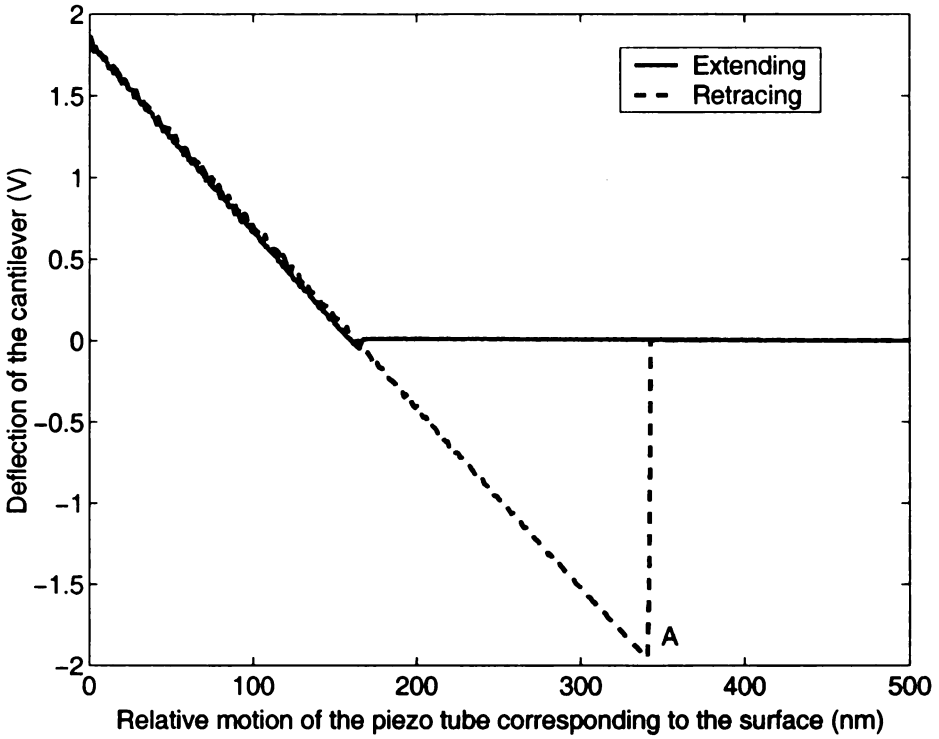

Figure 3.9. AFM force calibration result on glass surface

3.4.3 Calibration of $(k_l K_l/h)$

Although K_l can be estimated as $K_l \approx K_n/l$ (see Subsection 3.6.3), it is very difficult to obtain k_l. Fortunately, it is possible to calibrate the product $(k_l K_l/h)$. If there is a tilted hard surface with slope angle θ as shown in Figure 3.10, the following equation must be satisfied when the tip is sliding up or down along the tilted surface.

$$F_n = N\cos\theta + (\mu N + A)\sin\theta \tag{3.14}$$

$$F_l = N\sin\theta + (\mu N + A)\cos\theta \tag{3.15}$$

$$F_n = N'\cos\theta + (\mu N' + A)\sin\theta \tag{3.16}$$

$$F_l' = N\sin\theta + (\mu N' + A)\cos\theta \tag{3.17}$$

where F_n, F_l, F_l' are the load force and lateral forces respectively measured by AFM (when scanning angle $\psi = 0$, $F_n = F_z$); N, N' are the actual repulsive force from the

titled surface; $f = \mu N + A$ and $f' = \mu N' + A$ are the frictional forces including the frictions μN, $\mu N'$ and the adhesive shear force A. Here μ is the friction coefficient.

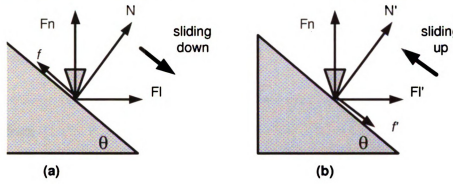

Figure 3.10. Force analysis when the tip is sliding up and down on a tilted surface

Equations (3.14) and (3.15) can be solved as

$$N = \frac{F_n - A\sin\theta}{\cos\theta + \mu\sin\theta} \quad : \quad \frac{\partial N}{\partial F_n} = \frac{1}{\cos\theta + \mu\sin\theta} \tag{3.18}$$

and Equations (3.16) and (3.17) can be solved as

$$N' = \frac{F_n - A\sin\theta}{\cos\theta - \mu\sin\theta} \quad : \quad \frac{\partial N'}{\partial F_n} = \frac{1}{\cos\theta - \mu\sin\theta} \tag{3.19}$$

From (3.15) and (3.17), it can be found that

$$\frac{\partial F_l}{\partial N} = \sin\theta - \mu\cos\theta \qquad \frac{\partial F_l'}{\partial N'} = \sin\theta + \mu\cos\theta$$

Therefore,

$$\frac{\partial F_l}{\partial F_n} = \frac{\partial F_l}{\partial N}\frac{\partial N}{\partial F_n} = \frac{\sin\theta - \mu\cos\theta}{\cos\theta + \mu\sin\theta} \tag{3.20}$$

$$\frac{\partial F_l'}{\partial F_n} = \frac{\partial F_l'}{\partial N'}\frac{\partial N'}{\partial F_n} = \frac{\sin\theta + \mu\cos\theta}{\cos\theta - \mu\sin\theta} \tag{3.21}$$

From (3.11), it can be seen that the measured normal force F_n is

$$F_n = kK_nS_n$$

and the measured lateral force F_y is

$$F_y = \frac{k_lK_l}{h}S_l$$

Noting that $F_l = F_y$ when $\phi = 0$, it is clear that

$$\frac{\partial F_l}{\partial S_l} = \frac{\partial F_l'}{\partial S_l'} = \frac{k_l K_l}{h} \tag{3.22}$$

and

$$\frac{\partial S_n}{\partial F_n} = \frac{1}{kK_n} \tag{3.23}$$

Therefore,

$$\frac{\partial F_l}{\partial F_n} = \frac{\partial F_l}{\partial S_l}\frac{\partial S_l}{\partial S_n}\frac{\partial S_n}{\partial F_n} = \frac{k_l K_l}{h}\frac{\partial S_l}{\partial S_n}\frac{1}{kK_n} \tag{3.24}$$

$$\frac{\partial F_l'}{\partial F_n} = \frac{\partial F_l'}{\partial S_l'}\frac{\partial S_l'}{\partial S_n}\frac{\partial S_n}{\partial F_n} = \frac{k_l K_l}{h}\frac{\partial S_l'}{\partial S_n}\frac{1}{kK_n} \tag{3.25}$$

Finally, $(k_l K_l/h)$ and μ can be found by solving the following two equations

$$\frac{k_l K_l}{h}\frac{\partial S_l}{\partial S_n}\frac{1}{kK_n} = \frac{\sin\theta - \mu\cos\theta}{\cos\theta + \mu\sin\theta} \tag{3.26}$$

$$\frac{k_l K_l}{h}\frac{\partial S_l'}{\partial S_n}\frac{1}{kK_n} = \frac{\sin\theta + \mu\cos\theta}{\cos\theta - \mu\sin\theta} \tag{3.27}$$

Equations (3.26) and (3.27) are nonlinear and they can be solved using the graphic method or other techniques.

Here is an example on how to find $(k_l K_l/h)$ for the cantilever with spring constant of 0.12 N/m.

- First, a titled glass surface was made and then scanned with 270^o scanning angle (the cantilever frame and the AFM frame are overlapped in this case and $\phi = 0$) and 10μm scanning range.
- Second, using the height information from the image, it is very easy to find the glass slope angle $\theta = 9.09^o$.
- Third, applying different load signals by changing the scanning setting point and recording both the applied voltage and detected friction voltage S_l and S_l'

from the friction loop, the plots of S_l and $S_l^{'}$ with respect to S_n are obtained as shown in Figure 3.11.

- Fourth, the slopes of S_l and $S_l^{'}$ with respect to S_n are found as $\partial S_l/\partial S_n = 0.07$ and $\partial S_l^{'}/\partial S_n = 0.02$.

- Finally, $(k_l K_l/h)$ and μ can be obtained by graphically solving (3.26) and (3.27) as shown in Figure 3.12. The results are $(k_l K_l/h) = 37.8\text{nN/V}$ and $\mu = 0.086$.

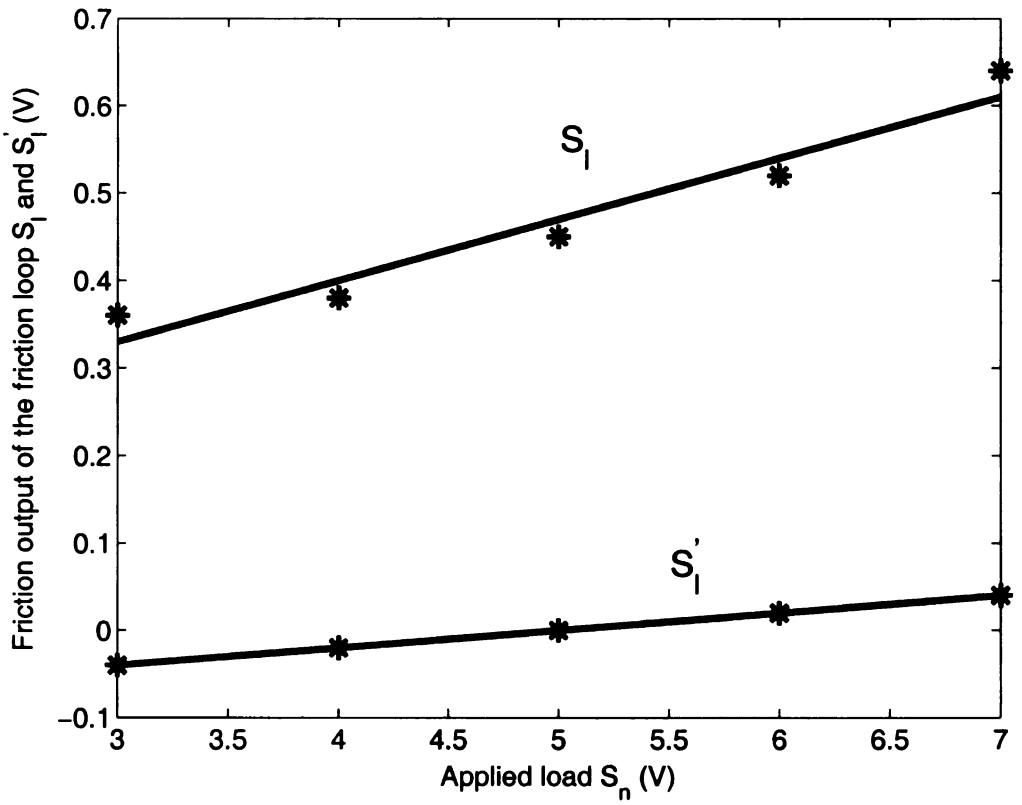

Figure 3.11. S_l and $S_l^{'}$ with respect to S_n. $\partial S_l/\partial S_n = 0.07$ and $\partial S_l^{'}/\partial S_n = 0.02$ respectively.

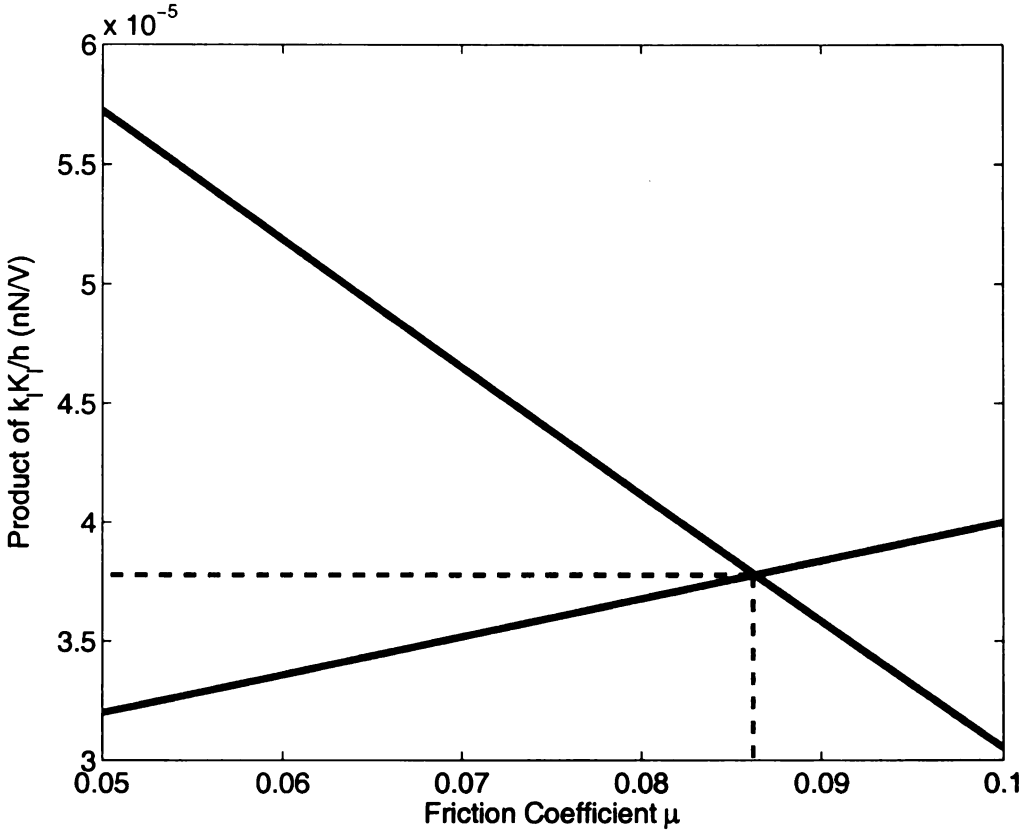

Figure 3.12. Graphic solution of $(k_l K_l/h)$ and μ. The cross point is the solution which shows that $(k_l K_l/h) = 37.8\text{nN/V}$ and $\mu = 0.086$

3.5 Force Compensation

It is usually very difficult to obtain the authentic force signals because force measurements usually contain many kinds of noises and errors. Due to the reflection of the substrate surface, the output of quad-photodiode detector is changing when the tip approaches the substrate surface as shown in Figure 3.13(a). The reflection of the substrate surface changes the original tuning position and creates a false normal force signal. The bow effect of the piezo tube also forms a false lateral force signal as shown in Figure 3.13(b). Figure 3.14 shows a single line scan result in which the tip loses contact with the surface. It can be seen that the reflection of the surface contributes a constant value to deflection signal and the bow effect makes the lateral signal tilted.

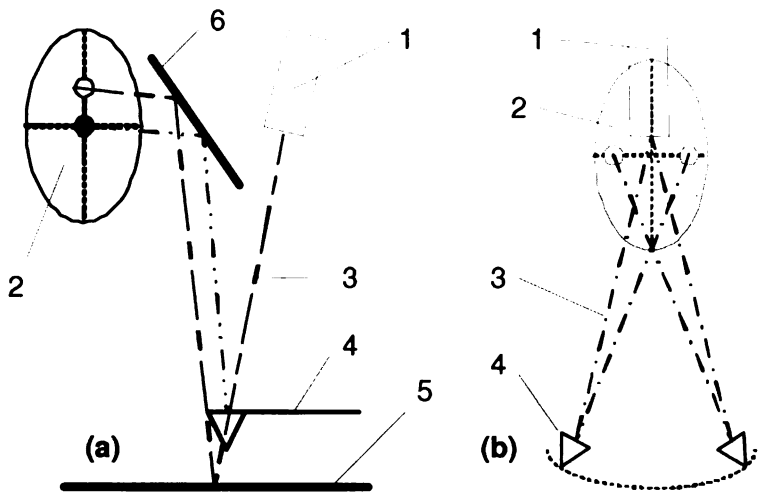

Figure 3.13. The mechanism of spurious forces due to substrate surface reflection and piezo tube bow effect: 1, laser gun, 2, quad-photodiode detector, 3, laser beam, 4, cantilever, 5, substrate surface, 6, mirror.

In addition, significant cross talk from normal direction to lateral direction has been observed. Ideally, the top surface of the cantilever should be perpendicular to the normal direction of the quad-photodiode detector, therefore the optical axis should be parallel with the normal direction of the quad-photodiode detector as shown in Figure 3.15(a). However, due to mounting errors, the optical axis may have a small angle ω with the quad-photodiode detector as shown in Figure 3.15(b). The small angle ω will cause a lateral signal output when the cantilever is bending without twisting. Also, due to tip misalignment during fabrication process, the tip may not be located on the cantilever body axis as shown in Figure 3.16. The tip misalignment is another reason contributing to cross-talk from normal to lateral direction in which cantilever may twist due to only the normal force without any lateral force present on the tip.

In order to obtain high fidelity of the force measurement, the spurious force signals and the cross-talk from normal to lateral channel have to be removed. Based on the analysis, the force signals in normal and lateral direction should be compensated by

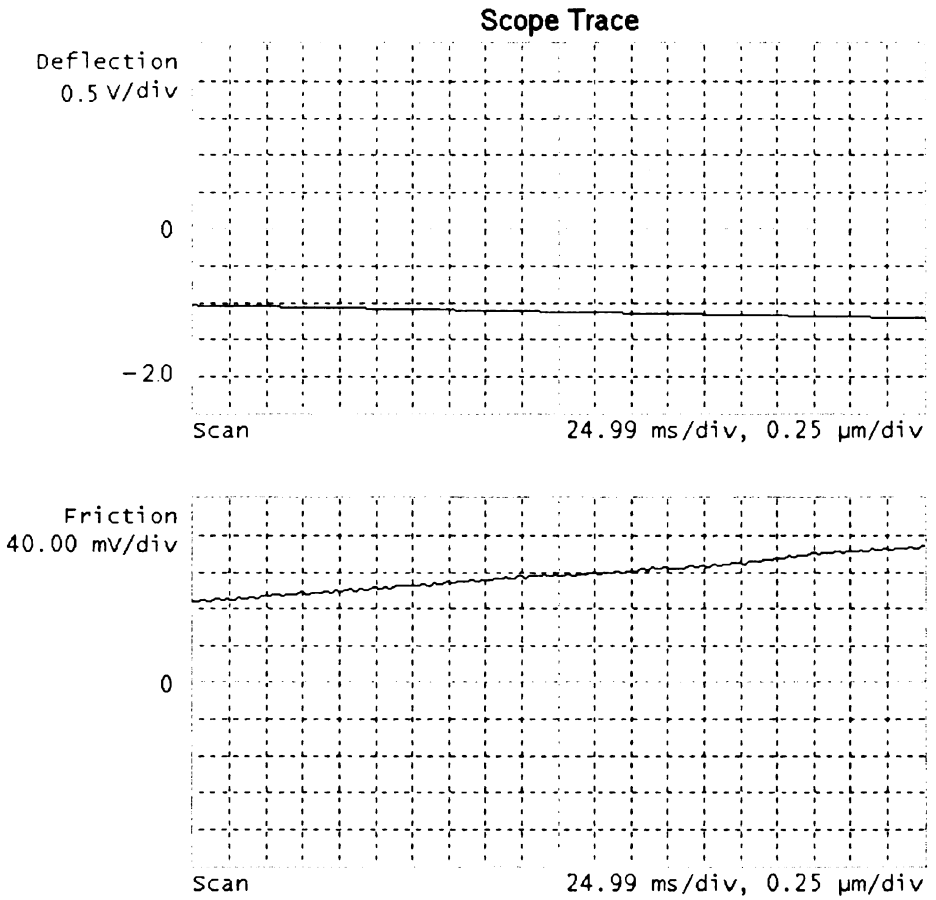

Figure 3.14. Single line free scan above sample surface. Top: deflection signal; Bottom: friction signal. The original of quad-photodiodes output is set at (-2.0,0)V for normal and lateral signal. The deflection setting point is set at 0V for image scanning. After system engaged in imaging mode, let the tip move above until the tip lose contact with the scanning surface. A single line free scan shows that the original point has increased to (-1.2, 0.12)V due to reflection of the sample surface, and also the lateral signal become titled.

following equations

$$\begin{cases} \bar{S}_n &= S_n - A(i,j) \\ \bar{S}_l &= S_l - B(i,j) - \alpha(S_n - A(i,j)) \end{cases} \tag{3.28}$$

where α is the cross-talk coefficient which can be calibrated; $A(i,j)$ and $B(i,j)$ are the compensation matrix for normal and lateral channel respectively, which can be recovered from the deflection and friction images by scanning a substrate surface

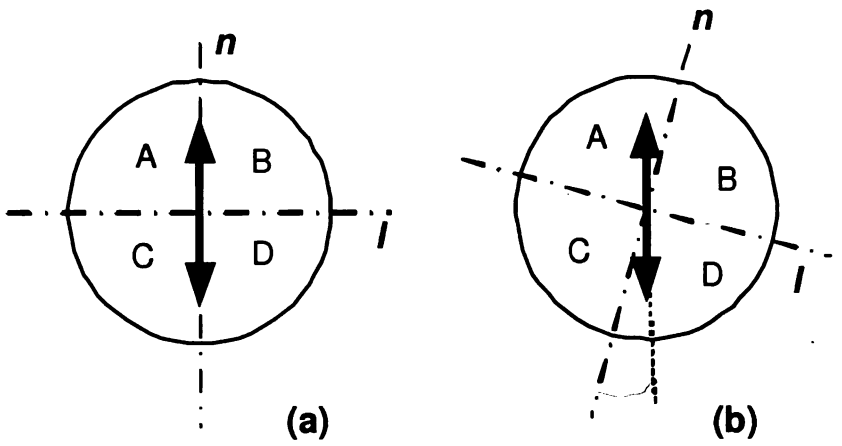

Figure 3.15. Cross-talk from normal to lateral direction, where n and l are the normal and lateral direction of the quad photodiode detector, and A, B, C, D are the photodiode outputs as described before. (a): In ideal case without mounting error, the normal deflection of cantilever will cause the laser spot up and down exactly along the normal direction of the detector. (b) In practice with mounting error, the normal deflection of cantilever will cause the laser spot up and down but twisting an angle ω with the normal direction of the detector. This results in lateral signal output without any lateral force present.

above its actual surface without contact. The indices i and j are determined by

$$\begin{cases} i &= \text{int}((N-1)x/L) + \text{int}(N/2) \\ j &= \text{int}(N/2) - \text{int}((N-1)y/L) \end{cases} \tag{3.29}$$

where L is the scanning range; N is the dimension of compensation matrix as defined before; and int(*) is a rounding function.

By pushing the tip down to a hard surface without lateral movement, the cross-talk coefficient α can be found as the slope of S_l corresponding to the changes of S_n. Figure 3.17 shows an example of one cantilever with spring constant of 0.12N/m, in which the cross-talk coefficient $\alpha = 0.18$.

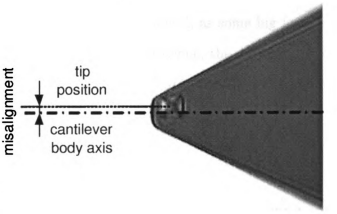

Figure 3.16. The tip is usually not located on the cantilever body axis due to the misalignment during fabrication process

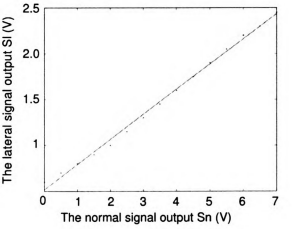

Figure 3.17. The lateral signal output due to the cross-talk from normal direction. The horizontal axis is the S_n signal (V) and the vertical axis is the S_l signal (V)

3.6 Position Control

One issue for AFM based nanomanipulation is the loss of the reference for the working space after changing the cantilever. Landmarks have to be used in order to solve this problem. Practically, there are many landmarks available such as some big features within the working area. Using the inverted optical microscope, the AFM can scan in a big area around the landmark. The working space can be easily recovered by zooming into the original working space.

3.6.1 Position Errors

The positioning precision is the one of the most critical issues in AFM based nanomanipulation. There are many factors which cause position errors, but the following three are the most significant ones.

The first cause of position errors is due to the thermal drift. If the the manipulation is not performed in a controlled environment, the thermal drift is random and sometimes can approach several hundred nanometers from our observation. The position error caused by thermal drift can be compensated using a local scan mechanism. Before starting the manipulation, a quick scan around the object can determine the actual position of the object. For more information about local scan, please refer to Chapter 5.

Another factor that causes the position errors is the bending of the cantilever in normal direction. The bending in normal direction inevitably engenders a lateral displacement along the length direction of the cantilever as analyzed in Section 3.6.2. Using a position compensation algorithm can minimize this effect. The position compensation algorithm is discussed in next section, and the related parameter

calibration methods are discussed in Section 3.6.3 and Section 3.6.4.

The third factor but not the last one causing the position errors is the van der Waals force and electrical static force between the nano-objects. Since the directions (attractive or repulsive) and the magnitudes of these forces are unpredictable, the behavior of objects is very difficult to predict when they are very close. Therefore, a small position error is inevitable.

3.6.2 Position Compensation

Not only is the haptic joystick used for force feedback, it is also used to command the tip to follow the trajectory generated by the operator. By mapping the position information of the joystick and scaling down to the AFM coordinates, the cantilever tip can be controlled to move above or slide on the sample surface. However, the cantilever is a long and thin beam or a triangular sheet bar, any deformation with respect to the original position in imaging mode will cause displacement of the tip both in normal and lateral direction as shown in Figure 3.18. The tip displacement should be proportional to the forces acting on the tip when the cantilever bending angle is very small.

$$\Delta = \hat{C}F \tag{3.30}$$

where $F = [F_x,\ F_y,\ F_z]^T$ are the forces acting on the tip; $\Delta = [\delta x,\ \delta y,\ \delta z]^T$ are the three dimensional displacement of tip position with respect to original position due to external forces; and

$$\hat{C} = \begin{bmatrix} c_{xx} & c_{xy} & c_{xz} \\ c_{yx} & c_{yy} & c_{yz} \\ c_{zx} & c_{zy} & c_{zz} \end{bmatrix}$$

is the gain matrix determined by material property and dimensionality of the cantilever. In practice, it is not a trivial problem to find each element in matrix $\hat{C}$.

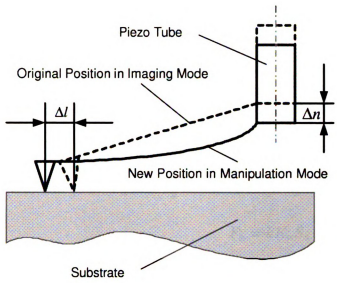

Figure 3.18. The mechanism of lateral displacement due to normal position changing: a Δn moving of the piezo-tube end in normal direction causes Δl tip movement in lateral direction

In [49], the gain matrix for rectangular cantilever has been calculated based on the spring constant and the dimensional size of the cantilever. However, it is almost impossible to obtain exact measurement of these parameters. Therefore, the gain matrix obtained by the estimation of the parameters usually has significant errors. In this research, an analytical method is introduced to find each element of $\hat{C}$ based on experiments.

From (3.2), it can be found that

$$\begin{bmatrix} \tau_x \\ \tau_y \\ \tau_z \end{bmatrix} = \begin{bmatrix} 0 & h & 0 \\ -h & 0 & -l \\ 0 & l & 0 \end{bmatrix} \begin{bmatrix} F_x \\ F_y \\ F_z \end{bmatrix} \tag{3.31}$$

Considering the dimensionality of the cantilever, it can be found that τ_x mainly causes the tip displacement in Y direction; τ_y mainly causes the tip displacement in X and Z direction. The tip displacement in Y direction caused by τ_z is negligible because of the triangular shape of the cantilever. Therefore,

$$\begin{bmatrix} \delta_x \\ \delta_y \\ \delta_z \end{bmatrix} = \begin{bmatrix} 0 & -c_2 & 0 \\ c_1 & 0 & 0 \\ 0 & -c_3 & 0 \end{bmatrix} \begin{bmatrix} \tau_x \\ \tau_y \\ \tau_z \end{bmatrix} \tag{3.32}$$

where c_1, c_2 and c_3 are constants. Combining (3.31) with (3.32) and noting (3.3),

(3.4), (3.5) and (3.9), the relationship between the tip displacement Δ and the forces F_n and F_y is obtained as

$$\begin{bmatrix} \delta_x \\ \delta_y \\ \delta_z \end{bmatrix} = \begin{bmatrix} 0 & 0 & c_2 l \\ 0 & c_1 h & 0 \\ 0 & 0 & c_3 l \end{bmatrix} \begin{bmatrix} 0 \\ F_y \\ F_n \end{bmatrix}$$

where $c_1 h$ and $c_2 l$ are unknown constants, $c_3 l = 1/k$ according to (3.1). According to (3.6) and (3.9), F_n and F_y are determined by

$$F_n = k K_n \bar{S}_n \tag{3.33}$$

$$F_y = \frac{k_l K_l}{h} \bar{S}_l \tag{3.34}$$

Then the tip displacement corresponding to the normal and lateral output signals becomes

$$\begin{bmatrix} \delta_x \\ \delta_y \\ \delta_z \end{bmatrix} = \begin{bmatrix} 0 & 0 & C_2 \\ 0 & C_1 & 0 \\ 0 & 0 & K_n \end{bmatrix} \begin{bmatrix} 0 \\ \bar{S}_l \\ \bar{S}_n \end{bmatrix}$$

here C_1 and C_2 are constants, which need to be calibrated (see Subsection 3.6.3), $\bar{S}_n$ and $\bar{S}_l$ are the true normal and lateral signals after compensation by (3.28). Finally, the new tip position with respect to the origin of AFM frame can be found using

$$\begin{bmatrix} x_t \\ y_t \\ z_t \end{bmatrix} = \frac{D}{L} \begin{bmatrix} x_p \\ y_p \\ z_p \end{bmatrix} + R^{-1} \begin{bmatrix} \delta x \\ \delta y \\ \delta z \end{bmatrix}$$

where D is a scaling constant from the haptic joystick to the AFM frame; L is the scanning range; $[x_p,\ y_p,\ z_p]^T$ is the coordinates of the joystick position; and R is same transformation matrix as defined before in Section 3.4.

3.6.3 Estimation of the Displacement Constant C_1

Calibration of C_1 experimentally is still an open problem but it can be estimated under certain assumptions. Assume the quad-photodiode detector has the same sensitivity

in both normal and lateral directions, i.e., the normal and lateral signal outputs should be equal if the bending angle in normal plane is equal to the twisting angle. Usually the bending and twisting angles are very small, so they can be estimated as

$$\theta \approx \tan\theta \approx \sin\theta$$

The bending angle can be estimated as

$$\theta_z \approx \frac{\delta z}{l} = \frac{K_n}{l} S_n$$

Considering the same sensitivity both in normal and lateral directions, i.e. $S_n = S_l$ when $\theta_z = \theta_x$, and noting that $\theta_x = K_l S_l$, it can be found that

$$K_l \approx K_n / l$$

The displacement in Y direction caused by the twisting angle can be estimated as

$$\delta y \approx \theta_x h = K_l h S_l = \frac{K_n h}{l} S_l$$

Finally, it can be found that $C_1 = K_n h / l$. Since h and l are known, and K_n can be calibrated, then C_1 is obtainable. For the cantilever with 0.12N/m spring constant, the displacement constant C_1 = 1.3nm/V.

3.6.4 Calibration of the Displacement Constant C_2

By inscribing several straight lines on a soft surface on different cantilever bending levels but with the same piezo tube end trajectory, the lateral displacement Δl can be directly measured. After setting the scanning angle to 0 degrees, the AFM frame rotates 180 degree corresponding to the cantilever frame. Therefore, the displacement along the X direction in the cantilever frame is equivalent to the displacement along the negative X direction in the AFM frame. Figure 3.19 shows 4 lines inscribed on a polycarbonate surface using the cantilever with spring constant 0.12N/m at different pushing depths. It can be seen that the displacement increases along the negative X

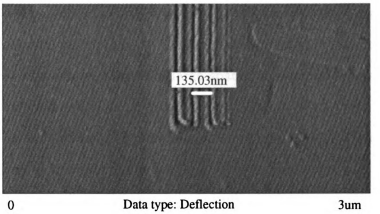

Figure 3.19. The lateral displacement caused by different pushing depths. The lines corresponding to the pushing depth are 2.0, 1.5, 1 and 0.5 μm from left to right. The distance between two neighboring lines is around 130nm.

direction in the AFM frame.

In order to minimize the measurement error, a large separation distance between lines is preferred. This requires a large pushing depth, d, which may cause the saturation of the normal signal output because the maximum normal signal output is only $\pm$10V. Since $K_n = 89\text{nm/V}$, any pushing depth larger than 890nm will cause signal saturation. However, this problem can be solved by introducing a virtual output $\hat{S}_n = d/K_n$, which is equivalent to S_n in analysis. The displacement constant C_2 is finally obtained as

$$C_2 = \frac{\delta x}{S_n} = \frac{\delta x_2 - \delta x_1}{\hat{S}_{n_2} - \hat{S}_{n_1}}$$

where $\delta x_2 - \delta x_1$ is the distance between two lines and $\hat{S}_{n_2} - \hat{S}_{n_1}$ is the virtual signal output difference between two lines. For the cantilever with 0.12N/m spring constant, the displacement constant $C_2 = 23\text{nm/V}$ according to the measured data from Figure 3.19.

3.7 Discussions

Nanomanipulation using Atomic Force Microscope (AFM) has been extensively investigated for many years. Most schemes suffer inefficiency from the lack of real-time visual feedback. The AFM based nano-robotic system developed in this chapter has

solved this problem, but the accuracy is still an issue due to the nonlinearities and uncertainties in nanomanipulation operations. The compensation of drift, creep, hysteresis and some other nonlinearities generating large spatial uncertainties have been studied in [50]. The compensation of these uncertainties improves the accuracy of nanomanipulation to a certain extent, but there are still some other important factors that significantly affect the accuracy of nanomanipulation. The deformation of the cantilever is one of the major nonlinearities that affect the tip position accuracy during manipulation. Although the deformation can be finely modelled and compensated, it is still difficult to accurately control the tip position due to the uncertainty of the deformation.

A soft cantilever can provide sensitive force feeling while pushing nano-objects, but on the other hand, the tip is very easy to slip over the nano-objects due to the flexibility of the cantilever. This makes the nanomanipulation unreliable and inefficient. Figure 3.20(a) shows the process of pushing a nano-object using a soft traditional tip that is not preloaded. Since there is no preloaded force, the tip floats on the surface during manipulation. As shown in Figure 3.20(a), the cantilever starts to bend after hitting the object and the bending will increase with the tip moving ahead. Finally, the bending causes the tip to slip over the object. Figure 3.20(b-d) show the experimental results that verified these analysis. Figure 3.20(b) shows an AFM image of a silver nanowire with length of 2.5 μm and diameter of 120 nm. A silicon nitride probe with a spring constant of 0.57 N/m is used to push the nanowire to follow the trajectory indicated by the arrow without pre-load. Figure 3.20(c) shows the image from a new AFM scan after manipulation. It can been seen that the manipulation failed and the nanowire is still in its original position. Figure 3.20(d) shows the cantilever deflection signal measured with the photodiode sensor. The tip hit the nanowire at $t = 30 second$ and began to push it. The tip

displacement reached a maximum value of $120nm$ at $t = 32second$ and then dropped to zero quickly. This means the tip slipped over the nanowire while pushing.

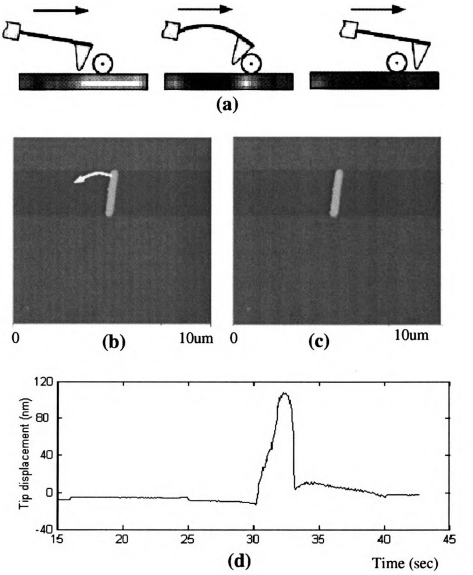

Figure 3.20. Pushing a silver nanowire with an un-preloaded traditional tip (k=0.57 N/m). (a) Schematic illustration of the pushing process. (b) The AFM image of a silver nanowire with length of 2.5 μm and diameter of 120 nm. The scanning range is $10\mu m \times 10\mu m$. (c) The AFM image by a new scan after pushing. (d) Cantilever deflection signal measured from the photodiode sensor.

The traditional way to overcome the tip slipping over the nano-objects is to apply a preloaded normal force on the tip to keep the tip contacting the surface. Figure 3.21(a) shows the process of pushing a nano-object using a preloaded traditional tip. As shown in the figure, the cantilever has a large bending even before touching the object due to the preloaded force. This large bending makes the tip scratch over the surface and thus avoid slipping over the object. However, since the preloaded force is much stronger than the interaction force, the deflection of the cantilever does not change much during manipulation of the object. Therefore, it is difficult to get sensitive force information from the deflection of the cantilever. Experimental results from Figure 3.21(b-d) verify the above analysis. The same tip used in previous experiment is used here to push the same nanowire. Figure 3.21(c) shows the image from a new AFM scan after manipulation. It is observed that the nanowire has been pushed successfully. Figure 3.21(d) shows the deflection signal during manipulation. The silicon nitride probe was preloaded and stuck on the surface at $t = 24second$, and then moved toward the rod. At $t = 33second$, the tip touched the nanowire and began to push it. Obviously, the preloaded force almost saturates the deflection signal and the interaction force between the tip and the object is almost unobservable. It becomes very difficult to feel the actual tip-object interaction force in this situation. Consequently, it is also very difficult to precisely control the tip position in the lateral direction during manipulation because the preloaded force not only causes the cantilever to bend in the normal direction but also causes the tip to move in the lateral direction as analyzed in Section 3.6. Furthermore, the preloaded force wears out the tip quickly and causes contamination easily.

Obviously, a rigid cantilever reduces the deformation significantly if its spring constant is large enough. Unfortunately, as the deformation is reduced, the feedback signal measured from the deformation is also reduced. Since the feedback signal is

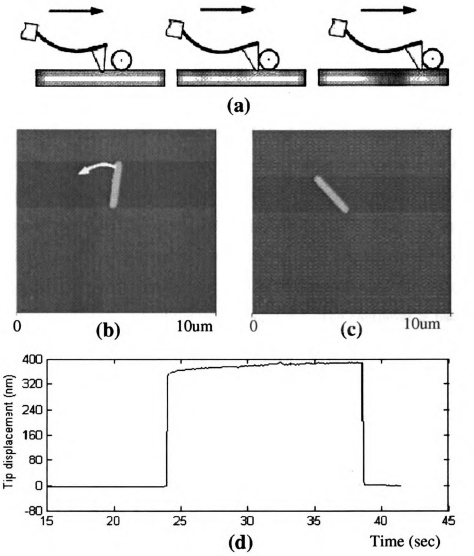

Figure 3.21. Pushing a silver nanowire with a preloaded traditional tip (k=0.57 N/m). (a) Schematic illustration of the pushing process. (b) The AFM image of a silver nanowire with length of 2.5 μm and diameter of 120 nm. The scanning range is 10 $\mu m \times 10$ μm. (c) The AFM image by a new scan after pushing. (d) Cantilever deflection signal measured with the photodiode sensor.

very important for closed-loop haptic nanomanipulation, it is a dilemma whether to use a soft cantilever or a rigid one for nanomanipulation. Fortunately, the invention of the active AFM probe [51, 52, 53] provides a promising way to solve this problem by actively changing the nominal rigidity of the cantilever. The cantilever can be

controlled to be rigid and maintain its straight shape, and thus the deformation of the cantilever is eliminated during manipulation. At the same time, the control signal is used to represent the interaction force, which can not be measured by a rigid cantilever. Hence, the active probe can be used to improve the accuracy of nanomanipulation and the force sensitivity of the haptic nanomanipulation system simultaneously. Figure 3.22 shows how an active probe (spring constant k = 1-5 N/m) works during pushing of a nano-object. In Figure 3.22(a), the active probe moves toward the object in its straight shape. In Figure 3.22(b), the tip of the active probe touches the object and the cantilever is bent by the interaction force. In Figure 3.22(c), a control voltage is applied to the piezo layer on the cantilever to eliminate the bending caused by the interaction force. The cantilever is back to its straight shape and the object is pushed away.

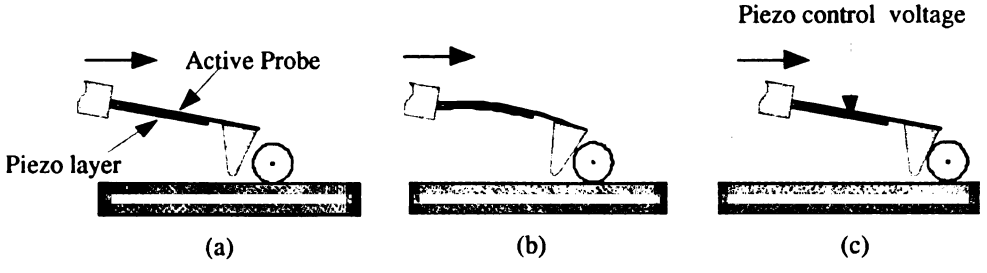

Figure 3.22. Schematic illustration of pushing a nano-object using the active probe

It is important to note that AFM probe needs to push the nano-objects in any random direction. When pushing direction is not in parallel with the axis direction of the cantilever, the manipulation force will not only cause the cantilever to bend in normal direction, but also cause the cantilever to twist around the axis of the cantilever as analyzed in Section 3.4. Since the cantilever is quite rigid in twisting mode, the twisting force is strong enough to twist the cantilever much to affect the accuracy of manipulation. Therefore, it is not necessary to actively control the

twisting. The only difficulty brought by the twisting is that the twisting signal is very difficult to measure. For the nanomanipulation using a soft traditional probe, a preloaded force is needed to press the tip on the surface. The preloaded force causes large friction force between tip and surface. Since the friction force will submerge the twisting force and the deflection force caused by objects during manipulation, the measured twisting signal is very noisy. In the nanomanipulation system using active probe, the control signal represents the deflection force, and the twisting signal from the photodiode represents the twisting force. Since the cantilever is controlled to keep straight and stay above the surface, the friction force between tip and sample surface is reduced significantly. Hence, the twisting force caused by manipulation can be easily measured.

The detailed discussion using active probe control for nanomanipulation can be found in [54]. In the paper the mathematical model of the probe is derived based on the continuous beam theory [55], which has been widely studied to control flexible manipulators [56, 57, 58, 59, 60]. Also an observer based optimal LQR control law is used to control the active probe. The experimental results verified the validity of the model and effectiveness of the controller. Moreover, the nanomanipulation results show that the active probe control during manipulation significantly facilitates the AFM based nanomanipulation, and improves the efficiency of nanomanipulation.

3.8 Summary

In this chapter, an augmented reality enhanced nano-robotic system is developed based on an existing AFM system. By linking the haptic device to the AFM probe, the tip position can be controlled by the operator. The real-time manipulation force information can also be displayed in three dimensions through the haptic device. The

augmented reality interface in the system , especially the visual display interface, has solved the notorious problem of AFM based nanomanipulation–the lack of real-time visual feedback. The real-time visual display is achieved by locally updating the AFM image during manipulation. The updating is based on the real-time force information and internal physical models of the system, which will be discussed in details in next chapter.

In order to accurately display the force information for force and visual feedback, the interaction forces applied to the tip have been well analyzed and the accurate force information is obtained after force compensation. The position control might be the most important issue for AFM based nanomanipulation. In Section 3.6, a detailed analysis of cantilever deformation has been provided and the appropriate compensation algorithm has been given. All the necessary calibration techniques relevant to the force measurement and position compensation are also provided in this chapter.

Finally, further improvement of the system is discussed in Section 3.7. Although the real-time visual feedback provides much more convenience for the operator, control of tip position during nanomanipulation is still an issue because of the deformation of the cantilever caused by the manipulation force. The softness of the conventional cantilevers also causes the failure when manipulating a relatively large and sticky nano-object because the tip can easily slip over the nano-object. In order to overcome these problems, an active atomic force microscopy probe has been proposed to change the cantilever's flexibility or rigidity through different control strategies in imaging and manipulation modes respectively. During the imaging mode, the active probe is controlled to bend up with respect to the interaction force between the tip and samples, thus making the tip response faster to increase the imaging speed. During the manipulation mode, the active probe is controlled to bend down with respect

to the interaction force between the tip and the samples and thus to increase its nominal rigidity to avoid tip slipping over nano-objects. The tip position control becomes very accurate because the active prove behaves like a rigid probe during manipulation and causes less deformation of the cantilever. The control signal serves as a force signal for haptic feedback since the interaction force between the tip and the object is proportional to the control signal.

CHAPTER 4

Nanoassembly Using the AFM Based Nano-Robotic System

4.1 Introduction

In the previous chapter, an augmented reality enhanced nano-robotic system is developed based on an existing AFM system. The augmented reality interface in the system , especially the visual display interface, has solved the notorious problem of AFM based nanomanipulation, the lack of real-time visual feedback. The real-time visual display is achieved by updating the AFM image locally during manipulation based on the real-time force information and internal physical models of the system.

In this chapter several physical models representing the interaction of tip, object, and sample surface will be discussed in details. All these models are essential for the real-time image updating because different nano-objects have different behaviors during manipulation and may need different strategies in order to move them. For simplicity, only rigid materials such as nano-particles and nano-rods will be considered in this chapter. More challenged soft nano-materials such as DNA

molecules will discussed in Chapter 6.

4.2 Manipulation of Nano-Particles

The nano-particle's motion behavior under manipulation may consist of sliding and rolling. Since the size of the particle is small and the shape of nano-particles is usually close to sphere, only the translation behavior of the nano-particles needs to be considered during manipulation in practice. The tip-surface-particle interaction has to be clearly modelled in order to determine whether the particle is moving or not.

In [61], a model of tip-substrate-particle interaction has been presented in a special case that the tip does not contact the substrate surface during manipulation. However, in general case, the tip usually contacts the substrate surface in order to guarantee sufficient pushing force during manipulation. For example, a preloaded force may be applied to the tip to avoid the tip slip over the object. In this section, the interaction among tip, object, and sample surface is modelled as in the general case that is much closer to reality.

4.2.1 Modelling Tip-Surface-Particle Interaction

The nano-particles under manipulation are usually with diameter from tens of nanometer to hundreds of nanometer. The tip height is usually several microns. The tip apex diameter ranges from several nanometer to tens of nanometer. Therefore, the size of nano-objects is usually bigger than the tip apex but much smaller than the tip body. Figure 4.1 shows the tip-particle interaction.

There are three main types of forces shown in Figure 4.1, adhesive, repulsive,

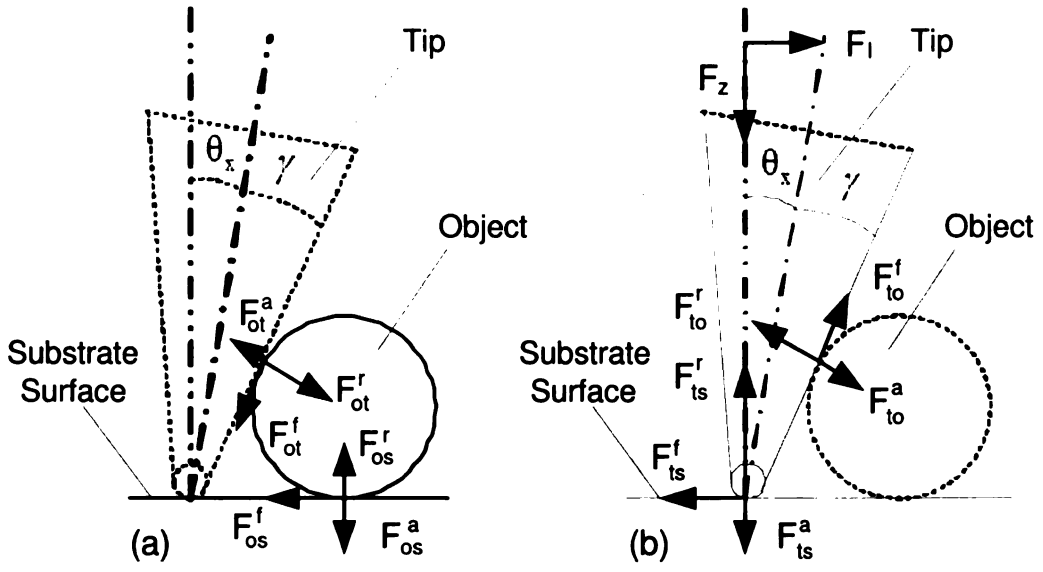

Figure 4.1. The model of tip-particle interaction where θ_x is the twisting of cantilever and γ is the open half angle of the tip apex: (a) the forces applied to the object, all the forces are balanced under equilibrium condition; (b) the forces applied to the tip, the overall effect of these forces is balanced by cantilever reaction, which causes the deformation of the cantilever such as bending and twisting.

and frictional force. The labelling of these forces is chosen in such a way that they are self-explained and can be distinguished easily. The superscript of force F could be one of 'a', 'f' or 'r', which represent 'adhesive', 'frictional', and 'repulsive' respectively. The subscripts could be a combination of 't', 'o' and 's', which represent 'tip', 'object', and 'substrate' respectively. For example, F^a_{to} represents the adhesive force applied to tip from the object.

Each type of these forces comes from many sources. The adhesive force may come from van der Waals force, capillary force, or molecular bonding. The repulsive force mainly comes from repulsive contact. The frictional force may come from the friction force caused by repulsive contact and the shear force caused by surface tension. All the forces dominant in the nanoscale can be theoretically calculated [61, 62, 63]. However, it is not feasible to compute them because some parameters

in the model are not obtainable. For example, object-surface distance, radii of curvature of the meniscus, and the thickness of the liquid layer, which are used to calculate the capillary force, are almost impossible to obtain. Although, each force coming from single source may not be obtainable, their overall effects are sometimes measurable. For example, the adhesive force between tip and substrate surface is measurable by AFM force calibration mode. Figure 4.2 shows the result from the AFM force calibration mode. When the tip is approaching the substrate surface and close to the surface, it suddenly drops down to the surface due to the long range of adhesive force such as electrostatic force. If the tip is pushed further down onto the surface, the repulsive force causes deflection of the cantilever. When the tip is driven away from the substrate surface, adhesive force causes the cantilever deflection to the opposite direction. The tip detachs from the surface when the pulling force reaches the critical point to break the equilibrium. The point A is the critical point as shown in Figure 4.2. According to JKR (Johnson, Kendal and Roberts) theory, the pull-off force at critical point is 75% of the adhesive force [62].

Since the adhesive forces are proportional to the contact areas and the adhesive force F_{ts}^a between the tip and substrate surface can be measured from Figure 4.2, then other adhesive forces can be estimated by the objects size such that

$$\frac{F_{ot}^a}{F_{ts}^a} = \frac{A_{ot}}{A_{ts}}, \quad \frac{F_{os}^a}{F_{ts}^a} = \frac{A_{os}}{A_{ts}}$$

where A_{ot}, A_{ts}, A_{os} represent the nominal contact area among tip, object, and substrate surface respectively.

As illustrated in Figure 4.1, the directions of the three main basic types of forces are known although the accurate force value is not available. Since the mass of a nano object is relatively small, the inertia force is usually ignorable. By assuming that the pushing direction is perpendicular to the body axis of the nano-object, the equilibrium condition of the nano-object both in horizontal and vertical direction can

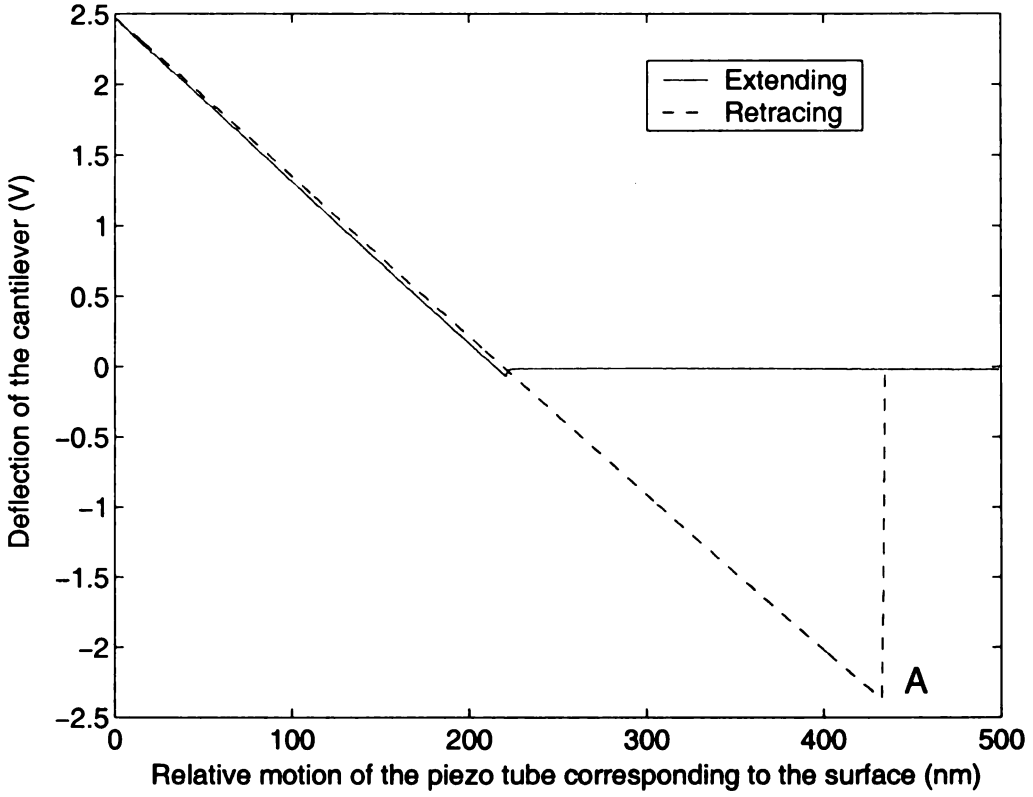

Figure 4.2. AFM force calibration result on graphite surface

be obtained as

$$F_{ot}^{r}\cos\theta = F_{os}^{f} + F_{ot}^{f}\sin\theta + F_{ot}^{a}\cos\theta \tag{4.1}$$

$$F_{os}^{r} + F_{ot}^{a}\sin\theta = F_{ot}^{f}\cos\theta + F_{ot}^{r}\sin\theta + F_{os}^{a} \tag{4.2}$$

where $\theta = \theta_x + \gamma$; θ_x is the twisting angle of the cantilever; and γ is the open half angle of the tip apex. The forces applied to the tip, as shown in Figure 4.1, should be balanced by the normal force F_z and the lateral force F_l from the cantilever. The equilibrium conditions of the tip in normal and lateral direction are

$$F_z + F_{to}^{a}\sin\theta + F_{ts}^{a} = F_{to}^{r}\sin\theta + F_{to}^{f}\cos\theta + F_{ts}^{r} \tag{4.3}$$

$$F_l + F_{to}^{f}\sin\theta = F_{to}^{r}\cos\theta - F_{to}^{a}\cos\theta + F_{ts}^{f} \tag{4.4}$$

Assume that $\bar{F}_z$ is the minimum value of F_z to maintain the equilibrium under the condition that $F_{ts}^{r} = 0$ when the tip apex is still contacting the substrate surface.

Noting that $F_{ot}^r = F_{to}^r$, $F_{ot}^f = F_{to}^f$, and $F_{to}^a = F_{ot}^a$, $\bar{F}_z$ can be solved by (4.1), (4.2) and (4.3) under the condition whether the nano-object is sliding or rolling. In the macro-world, round particles or tubes tend to roll instead of slide. The rolling behavior of carbon nanotube on graphite substrate surface has been observed in [64]. However, this may not always be true in a nano environment. In most cases, the objects under manipulation will slide on the surface due to their irregular shape and strong adhesive force. Therefore, only object sliding on the surface will be discussed here. The analysis of object rolling on the surface is similar to the analysis of object sliding on the surface.

During sliding, the rolling potential due to the friction, F_{os}^f, has been balanced by the irregular distribution of the adhesive force, F_{os}^a. The object has no relative movement with respect to the tip but slides on the substrate surface. Therefore, the friction F_{ot}^f can be assumed as zero. The friction, F_{os}^f, between object and substrate surface should be proportional to the repulsive force, F_{os}^r, and the adhesive force, F_{os}^a, such that

$$F_{os}^f = \mu_{os} F_{os}^r + \upsilon F_{os}^a \tag{4.5}$$

where μ_{os} is the sliding frictional coefficient between object and substrate surface and ν is the shear coefficient. Using (4.5) to solve (4.1) and (4.2), the repulsive force between the tip and the object, F_{ot}^r, can be obtained as

$$F_{ot}^r = F_{ot}^a + \frac{\mu_{os} + \upsilon}{\cos\theta - \mu_{os}\sin\theta} F_{os}^a \tag{4.6}$$

In order to prevent the tip from squeezing the nano-object into the substrate surface, the angle θ should be less than a minimum value. This value can be found by letting the denominator of the second term in (4.6) equal zero i.e. F_{ot}^r goes to infinity. Therefore,

$$\theta_{max} = \operatorname{atan}\left(\frac{1}{\mu_{os}}\right)$$

Substituting (4.5) and (4.6) into (4.3), and letting $F_z = \bar{F}_z$ and $F_{os}^r = 0$, the minimum value of F_z and the lateral force from cantilever can be obtained as

$$\bar{F}_z = \frac{(\mu_{os} + v)\sin\theta}{\cos\theta - \mu_{os}\sin\theta} F_{os}^a - F_{ts}^a \tag{4.7}$$

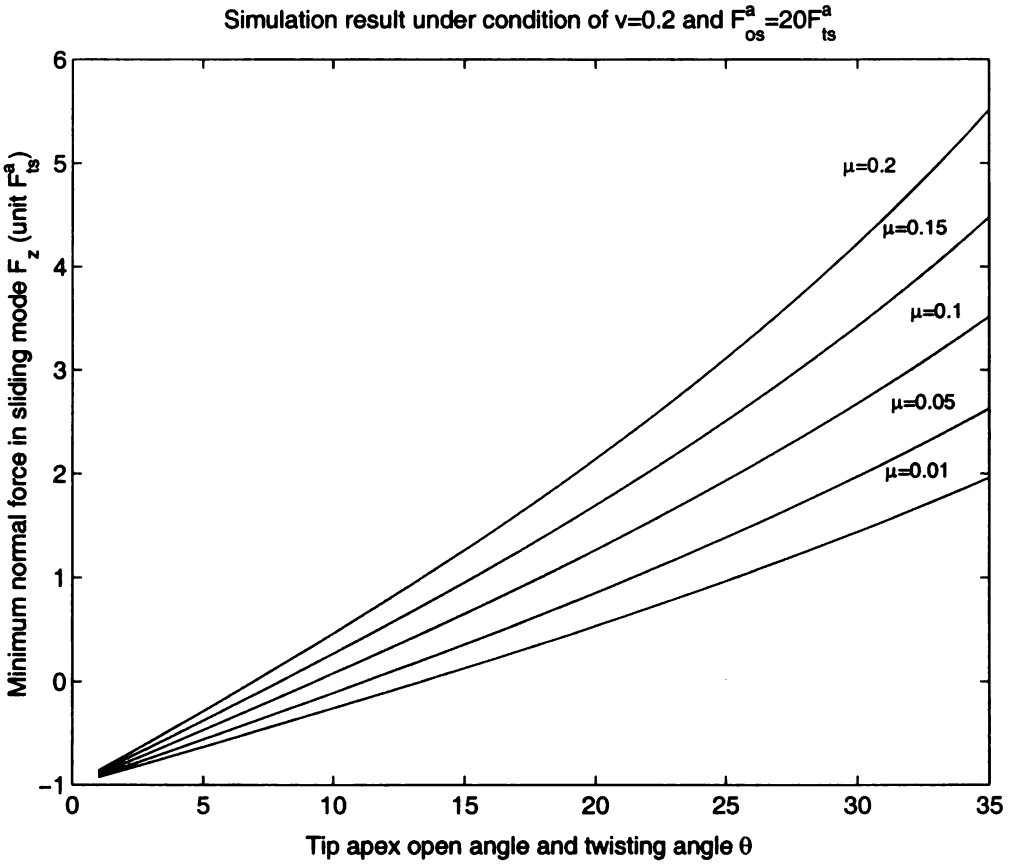

Figure 4.3. The minimum normal force, $\bar{F}_z$, to keep tip on surface corresponding to θ and μ (The unit of $\bar{F}_z$ here is F_{ts}^a).

In order to maintain the pushing condition, F_z has to be larger than $\bar{F}_z$. The additional force is balanced by $F_{ts}^r = F_z - \bar{F}_z$. If $\bar{F}_z < 0$, it means that the adhesive force itself can keep the tip in contact with the substrate surface. During manipulation, a small F_z is preferred since a large F_z induces a large friction force F_{ts}^f, which wears out the tip apex quickly. From the simulation result in Figure 4.3, it can be seen that $\bar{F}_z$ is proportional to θ. Considering $\theta = \theta_r + \gamma$, a stiff cantilever and a

tip with small apex open angle are preferred for nanomanipulation. This conclusion that a stiff cantilever is preferred for nanomanipulation agrees with the experimental results as discussed in Section 3.7.

4.2.2 Experiments on Manipulation of Nano-Particles

Using the augmented reality enhanced nano-robotic system, manipulation of latex particles has been performed to verify the effectiveness of the real-time visual display. Latex particles with diameters of 100nm are distributed on a glass surface as shown in Figure 4.4(a). The real-time AFM image is displayed in the augmented reality interface as shown in Figure 4.4(b). A new scanning image as shown in Figure 4.4(c) shows that the final result matches the image displayed in the augmented reality interface.

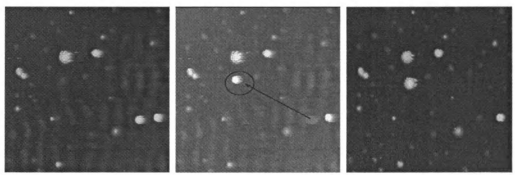

(a) (b) (c)

Figure 4.4. Pushing latex particles on a glass surface with operation range of 10μm. (a) Image of latex particles before manipulation; (b) The real time display on the augmented reality interface during pushing operation. The arrow indicates the pushing direction and pushing path; (c) A new scanning image after manipulation

Under the assistance of visual feedback through the augmented reality interface, manipulation of nano-particles becomes very straightforward. Its efficiency can be verified in Figure 4.5. It can be seen that a lot of particles can be manipulated

without the need of new image scan. Latex particles with diameters of 50nm are distributed on a polycarbonate surface. The real-time AFM image is displayed in the augmented reality interface as shown in Figure 4.5(b). A new scanning image as shown in Figure 4.5(c) shows that the final result matches the image displayed in the augmented reality interface. The little mismatch of the final positions of the latex particles between the augmented reality display and the final result from the new image scan is due to the inevitable position errors as analyzed in Section 3.6. The experimental result shown in Figure 4.6 is obtained by pushing more than one hundred nano particles to form complex patterns within half an hour.

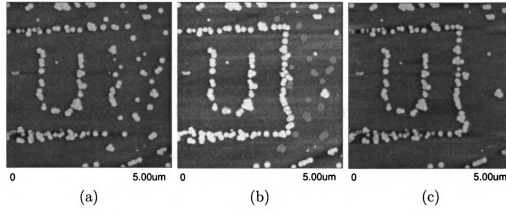

Figure 4.5. Pushing latex particles (diameter of 50nm) on a polycarbonate surface with an operation range of 5μm. (a) Image of latex particles on a glass surface before manipulation (b) the real time display on the augmented reality during pushing operation. (c) A new scanning image after manipulation

4.3 Manipulation of Nano-Rods or Nano-Wires

In order to enable assembly of nanowires using the augmented reality enhanced nano-robotic system, the tip-wire-surface interaction model and the wire behavior model during nanomanipulation have to be developed in order to update the image displayed

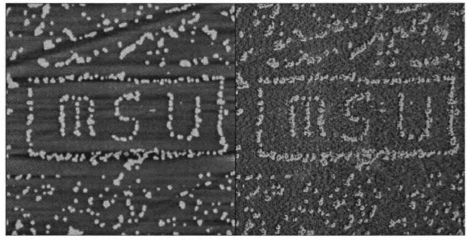

Figure 4.6. Pushing particles on a polycarbonate surface to form patterns. The nano-objects are latex particles in diameters of 50nm. The working area is $10\mu m \times 10\mu m$.

in the augmented reality interface in real time.

4.3.1 Modeling the Behavior of the Nanowire under Pushing

The nanowire under pushing may have different kinds of behavior, which depends on its own geometric properties. Define the aspect ratio of a nanowire as

$$\sigma = L/d$$

Practically, a nanowire with an aspect ratio of $\sigma > 25$ usually behaves like a soft wire, which will deform or bend under pressure. Figure (4.7) shows a nanowire with an aspect ratio of 30 which was bent by pushing it from one end.

The rotation behavior is observed for nanowires with aspect ratios of $\sigma < 15$. The deformation of the nanowires with large aspect ratio needs further investigation in order to model the behavior of the nanowire. In this chapter, only the nanowires with aspect ratio less than 15 will be discussed. The nanowires with such aspect ratio are often called nanorods. The detailed external forces applied on the nanorod in this case have been shown in Figure 4.8(a). The nanorod with dimension of $L \times d$ is

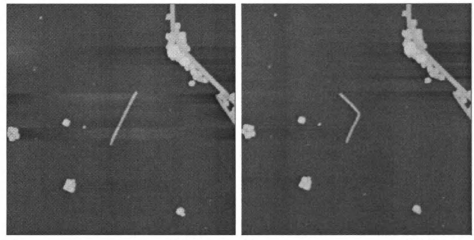

(a) (b)

Figure 4.7. A silver nanowire with aspect ratio of $\sigma = 30$ is bent due to the external pushing force. (a): The nanowire before pushing (b): The nanowire after pushing, which was bent in the middle

pushed at point T and it rotates around point S. The pushing force F from the tip causes the friction or shear force F' which can be calculated as

$$F' = \mu_{ot} F + \nu F_{ot}^{a}$$

where μ_{ot} and ν are the friction and shear coefficients between the tip and the nano-object. The values of these parameters depend on material properties and the environment; F_{ot}^{a} is the adhesion force between the tip and the nanorod. The shear force F' is along the rod axis direction when the pushing direction is not perpendicular to the rod axis. Fortunately, it is easy to prove that the force F' does not cause any significant rod movement along the rod axis direction. Assuming that the shear forces between the rod and the substrate surface are equal along any direction during moving, then

$$fL = f'_{\max} d$$

The shear force is usually proportional to the contact area and the contact area between the rod and surface is much greater than that between the tip and the rod.

Therefore

$$\nu F_{ot}^{a} << f^{'} d$$

And also note that

$$F <= fL = f_{\max}^{'} d$$

Because μ is usually is very small, finally it is reasonable to assume that

$$f^{'} d = F^{'} = \mu F + \nu F_{ot}^{a} < f_{\max}^{'} d$$

This means that the rod will have no motion along the rod axis direction. Therefore, the pivot S must be on the axis of the rod.

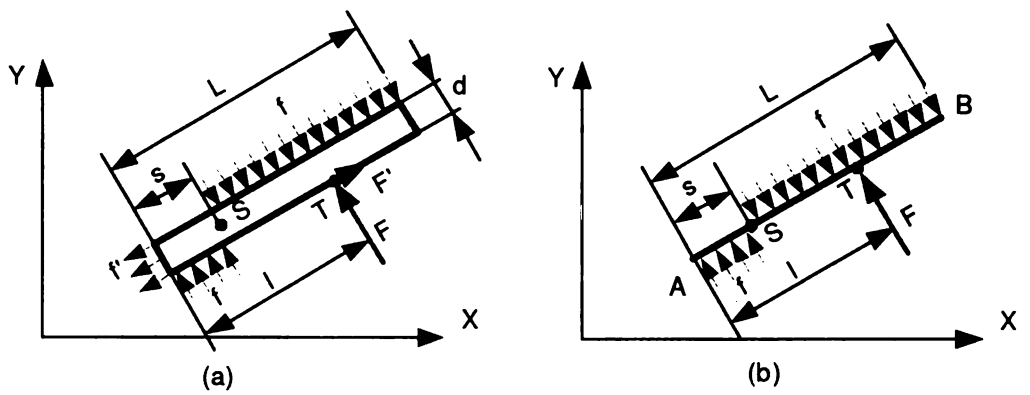

Figure 4.8. The external forces applied on a nanorod in surface plane. (a): The detailed force model. Here S is the pivot; T is the pushing point and also the tip position; L is the length of the rod; d is the width of the rod; l is the length between the pushing point and the reference end; s is the distance between the pivot S and the reference end; F is the pushing force from the tip; $F^{'}$ is the friction and shear force from tip; f is the evenly distributed friction and shear force density on the rod; $f^{'}$ is the evenly distributed friction and shear force density along the axis of the wire. (b): The simplified force model. Here, A is the reference point; B is the other end of the rod; the other parameters are the same as in (a).

Considering the above analysis, the nanorod can be simplified as a line segment. The external forces applied on the nanorod in the surface plane can be modeled as in

Figure 4.8(b). The pivot S can be either inside or outside of the rod. First assume that S is inside the rod. In this case, all the torques around S are self balanced during smooth moving.

$$F(l-s) = \frac{1}{2}f(L-s)^2 + \frac{1}{2}fs^2$$

namely,

$$F = \frac{f(L-s)^2 + fs^2}{2(l-s)} \tag{4.8}$$

There must be an s which can minimize F, in which the rod begins to rotate once the pushing force F reaches this minimum force F_{min}. Therefore, the pivot S can be determined by the following equation

$$\frac{dF}{ds} = 0 \quad : \quad s^2 - 2ls + lL + L^2/2 = 0 \tag{4.9}$$

Since we have assumed that $0 < s < L$, a unique solution of Equation (4.9) for any $0 < l < L$ except $l = L/2$ is

$$s = \begin{cases} l + \sqrt{l^2 - lL + L^2/2} & l < L/2 \\ l - \sqrt{l^2 - lL + L^2/2} & l > L/2 \end{cases} \tag{4.10}$$

The results are shown in Figure 4.9. It can be seen that the pivot will never fall between $(1 - \sqrt{2}/2)L$ and $\sqrt{2}L/2$.

When $l = L/2$, there is no unique solution. A detailed analysis will show that S can be anywhere outside the wire when the force F is applied in the exact middle of the wire, in which T becomes a bifurcation point. Now, assume the pivot S is outside of the rod but in the left side. Noting that $s < 0$ now, the self-balanced torque equation becomes

$$F(l-s) = fL(L/2 - s)$$

Namely,

$$F = \frac{fL(L/2-s)}{2(l-s)} \tag{4.11}$$

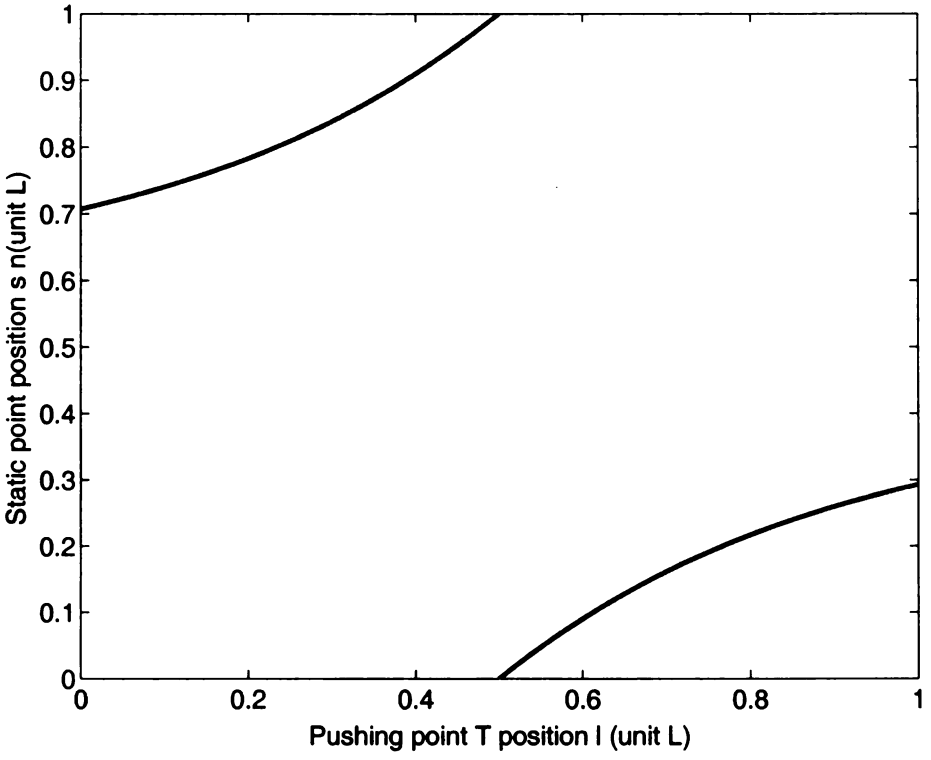

Figure 4.9. Possible position of the pivot S. When $l < L/2$, S falls between $\sqrt{2}L/2$ to L; When $l > L/2$, S falls between 0 to $(1 - \sqrt{2}/2)L$ to L; When $l = L/2$, the solution is not unique.

By minimizing F, it can be seen that only when $l = L/2$ can enable

$$\frac{dF}{ds} = 0$$

Similarly, if S is in the right side, the results should be the same. Practically, it is hard to keep T at this bifurcation point ($l = L/2$). Any disturbance will move the pivot to one end of the wire. Therefore, during manipulation, it is better to avoid pushing the exact middle of the nanorod because it is hard to predict the behavior of the nanorod in this situation. The manipulation scheme of a nanorod has to go through a zigzag strategy in order to position the nanorod to a specified orientation. This prediction will be proven in next section by experiments.

4.3.2 Verification of the Nano-Rod Behavior Model

In order to validate the rod behavior model, a silver nanorod (From Xia's group in the University of Washington) was pushed on a smooth polycarbonate surface as shown in Figure 4.10. The AFM image of the nano-rod before pushing is shown in Figure 4.10(a). The arrow indicates the pushing direction, and Point T is the pushing position which is close to the center of the nano-rod. After pushing, the result was checked by a new scanning on the surface. The new AFM image shows that the nanorod rotated around a pivot at S, which is close to the end of the rod as shown in Figure 4.10(b).

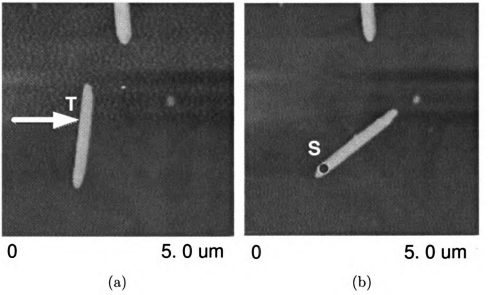

Figure 4.10. Pushing a silver nanorod with diameter of 130nm and length of 2μm on a smooth polycarbonate surface in scanning range of $5\mu m \times 5\mu m$. (a) AFM image before pushing. The arrow indicates the pushing direction, and T is the pushing position. (b) AFM image after pushing point. S is the turning pivot.

After the first pushing, a second pushing was performed but the nano-rod was pushed at the other end as shown in Figure (a). After second pushing, the new image scan in Figure 4.11(b) shows that the turning pivot S moves inside the nano-rod.

The two experimental results exactly agree with what is predicted by the theoretical result from Equation (4.10). Therefore, the correctness of the behavior model of nanorod is proven.

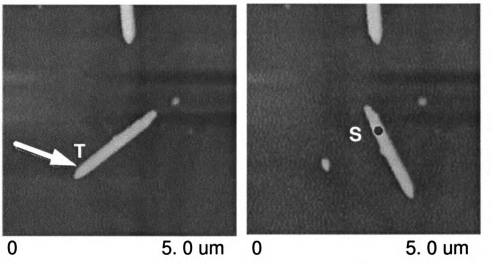

Figure 4.11. Pushing a silver nano-rod with diameter of 130nm and length of 2μm on a smooth polycarbonate surface in scanning range of $10\mu m \times 10\mu m$. (a) AFM image before pushing. The arrow indicates the pushing direction, and T is the pushing position . (b) AFM image after pushing point. S is the turning pivot.

4.3.3 Modelling the Tip-Substrate-Rod Interaction

After the motion behavior of the nanorod has been modelled, the motion of the nanorod should be predictable once the pushing force reaches the minimum force required to move the nanorod. The minimum force required for pushing the nanorod at different locations can be solved by the self-balanced force equations as follows

$$F = \begin{cases} fs - f(L-s) = f(2s-L) & l < L/2 \\ f(L-s) - fs = f(L-2s) & l > L/2 \end{cases} \tag{4.12}$$

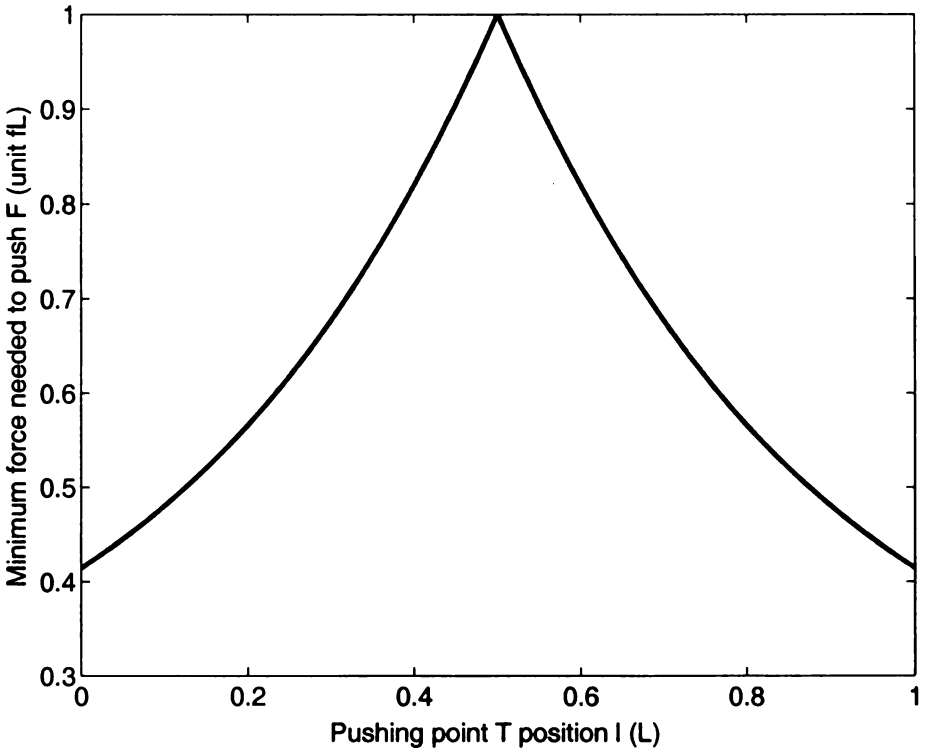

Figure 4.12. Minimum force required for pushing a nanorod at different locations. The pushing force is only $(2-\sqrt{2})fL$ when pushing the nanorod from the end; the pushing force reaches the maximum value fL when pushing the nanorod exactly at the mid position.

The relation between F and l is shown in Figure 4.12. It can be shown that a maximum force $F_{max} = fL$ is needed in order to push the nanorod in the middle and a minimum force $F_{min} = (2-\sqrt{2})fL$ to push the wire at the end. This is another reason that we prefer pushing the nanorod from the end. Obviously, if the tip can generate a pushing force $F > fL$, then the nanorod is movable on the surface and follows the motion pattern predicted. Otherwise, the nanorod remains static on the surface and the tip may slip over the nanorod.

From Figure 4.8, it is obvious that

$$fL = \mu_{os} F_{os}^{r} + \nu F_{os}^{a}$$

where F_{os}^{r} is the repulsive force between the object and the substrate surface; μ_{os} is the sliding friction coefficient between the nanorod and the substrate surface; F_{os}^{a} is the adhesion force between the object and the substrate surface; ν is the shear coefficient. Now Equation (4.12) becomes

$$F = \begin{cases} (2s/L - 1)(\mu_{os}F_{os}^{r} + \nu F_{os}^{a}) & l < L/2 \\ (1 - 2s/L)(\mu_{os}F_{os}^{r} + \nu F_{os}^{a}) & l > L/2 \end{cases} \tag{4.13}$$

Let

$$\rho = \begin{cases} (2s/L - 1) & l < L/2 \\ (1 - 2s/L) & l > L/2 \end{cases}$$

Then

$$\rho = \begin{cases} 2(l + \sqrt{l^2 - lL + L^2/2})/L - 1 & l < L/2 \\ 1 - 2(l + \sqrt{l^2 - lL + L^2/2})/L & l > L/2 \end{cases}$$

Then Equation (4.13) becomes

$$F = \rho(\mu_{os}F_{os}^{r} + \nu F_{os}^{a}) \tag{4.14}$$

The interaction among tip, substrate, and nanorod can be modelled as shown in Figure 4.13. Three main types of forces are shown in Figure 4.13: adhesive, repulsive, and frictional force. The labelling of these forces is chosen in such a way that they are self-explained and distinguished easily. The superscript of force F could be one of 'a', 'f' or 'r', representing 'adhesive', 'frictional', and 'repulsive' respectively. The subscripts could be a combination of 't', 'o' and 's', representing 'tip', 'object', and 'substrate' respectively. For example, F_{to}^{a} represents the adhesive force applied to tip by the object.

As illustrated in Figure 4.13, the directions of the three main basic types of forces are known although the accurate force value is not available. By assuming that the pushing direction is perpendicular to the body axis of the nanorod, the equilibrium condition of the nanorod in both horizontal and vertical directions can be obtained as

$$F_{ot}^{r}\cos\theta = F_{os}^{f} + F_{ot}^{f}\sin\theta + F_{ot}^{a}\cos\theta \tag{4.15}$$

$$F_{os}^{r} + F_{ot}^{a}\sin\theta = F_{ot}^{f}\cos\theta + F_{ot}^{r}\sin\theta + F_{os}^{a} \tag{4.16}$$

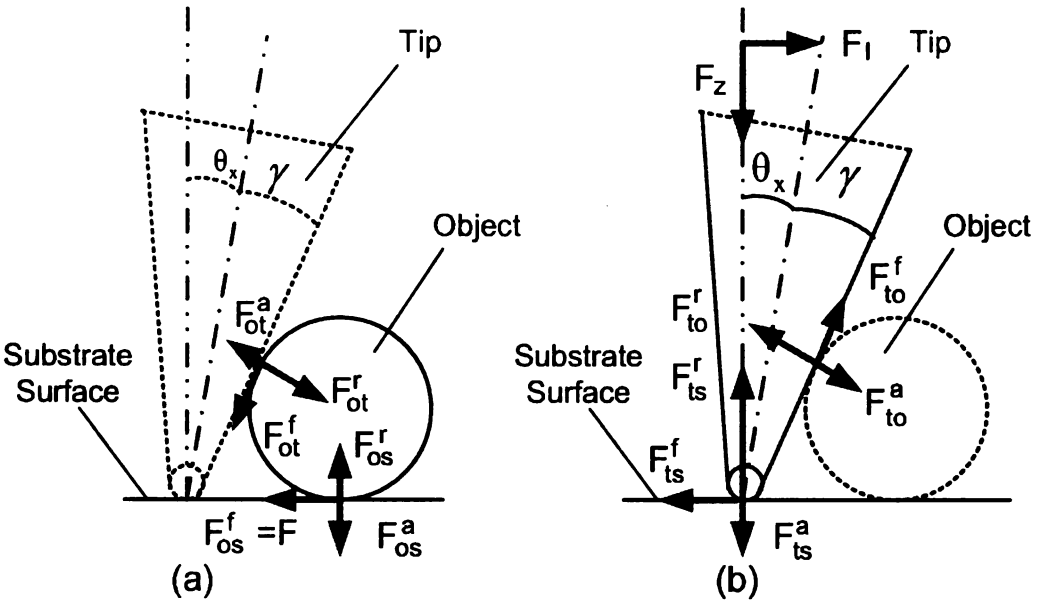

Figure 4.13. The model of tip-rod interaction, where θ_x is the twisting of the cantilever and γ is the open half angle of the tip apex: (a) The forces applied to the wire; (b) The forces applied to the tip.

The equilibrium conditions of the tip in the normal and lateral directions are

$$F_z + F^a_{to}\sin\theta + F^a_{ts} = F^r_{to}\sin\theta + F^f_{to}\cos\theta + F^r_{ts} \tag{4.17}$$

$$F_l + F^f_{to}\sin\theta = F^r_{to}\cos\theta - F^a_{to}\cos\theta + F^f_{ts} \tag{4.18}$$

Define $\bar{F}_z$ as the minimum value of F_z to maintain the equilibrium under the condition that $F^r_{ts} = 0$ when the tip apex is still contacting the substrate surface. Noting that $F^r_{ot} = F^r_{to}$, $F^f_{ot} = F^f_{to}$, and $F^a_{to} = F^a_{ot}$, $\bar{F}_z$ can be solved by Equation (4.15), (4.16) and (4.17) if it is know that the nanorod is sliding or rolling. Whether the nanorod is sliding or rolling is determined by the energy cost during pushing. It has been observed that the energy cost for rolling is larger than that for sliding when pushing a carbon nanotube sideways. Therefore, the nanotubes should prefer sliding instead of rolling. Although the rolling behavior of a carbon nanotube on a graphite substrate surface has been observed in [64], in most cases, the nanorods under manipulation should slide on the surface due to their irregular shape,

deformation, and strong adhesive force. During sliding, the rolling potential caused by the friction, F_{os}^{f}, is balanced by the irregular distribution of the adhesive force, F_{os}^{a}. The nanorod has no relative movement with respect to the tip but slides on the substrate surface. Therefore, the friction F_{ot}^{f} can be assumed to be zero. The friction, F_{os}^{f}, between the object and the substrate surface is the force that needs to be overcome in order to move the nanorod on the surface. Therefore $F_{os}^{f} = F$, which can be calculated from Equation (4.14). Using (4.14) to solve (4.15) and (4.16), the repulsive force between the tip and wire, F_{ot}^{r}, can be obtained as

$$F_{ot}^{r} = F_{ot}^{a} + \frac{\rho(\mu_{os} + v)}{\cos\theta - \rho\mu_{os}\sin\theta} F_{os}^{a} \tag{4.19}$$

In order to prevent the tip from squeezing the nanorod into the substrate surface, the angle θ should be less than a certain value. The value can be found by letting the denominator of the second term in (4.19) equal zero i.e. F_{ot}^{r} goes to infinity. Therefore,

$$\theta_{max} = \text{atan}\left(\frac{1}{\rho\mu_{os}}\right)$$

Substituting (4.19) into (4.17), and letting $F_z = \bar{F}_z$, $F_{ts}^{r} = 0$ and $F_{ot}^{f} = 0$, the minimum value of F_z to maintain the equilibrium condition is

$$\bar{F}_z = \frac{\rho\sin\theta(\mu_{ot} + v)}{\cos\theta - \rho\mu_{os}\sin\theta} F_{os}^{a} - F_{ts}^{a} \tag{4.20}$$

In order to maintain the pushing condition, F_z has to be larger than $\bar{F}_z$. The additional force is balanced by $F_{ts}^{r} = F_z - \bar{F}_z$. If $\bar{F}_z < 0$, it means that the adhesive force itself can keep the tip in contact with the substrate surface. During manipulation, a small F_z is preferred since a large F_z will induce a large friction force F_{ts}^{f}, which wears out the tip apex quickly. The simulation results of the minimum force $\bar{F}_z$ corresponding to θ, μ and l have been shown in Figure 4.14 and Figure 4.15. From the simulation results, it can be seen that $\bar{F}_z$ is proportional to θ. Therefore, a stiff cantilever and a tip with a small apex and very small open angle are also preferred for manipulation of nanorods.

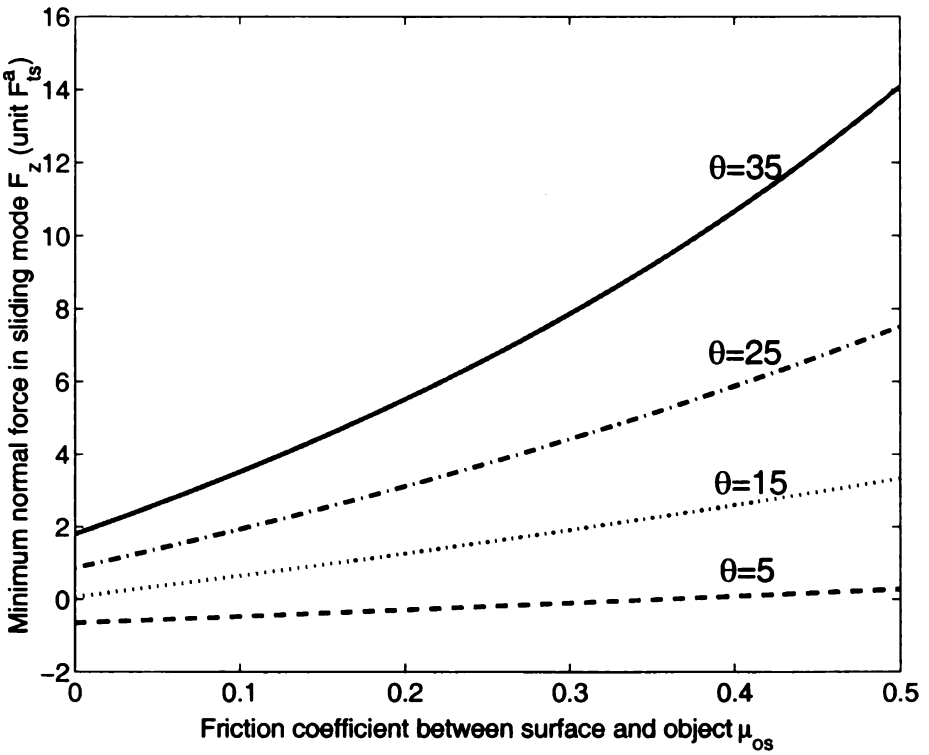

Figure 4.14. The minimum normal force, $\bar{F}_z$, to keep the tip on the surface in sliding mode as a function of θ and μ (The unit of $\bar{F}_z$ here is F_{ts}^a. Assume $F_{os}^a = 20F_{ts}^a$, and $\nu = 0.2$).

4.3.4 Experiments on Assembly of Nanowires

In order to fabricate nano-devices, some of the nano-structures have to be positioned in desired locations. For example, a carbon nanotube has to be fixed between two electrodes in order to make it a nano-sensor. Fortunately, under the assistance of the augmented reality enhanced system, it is possible to first create a fixture and then push the nanowire into the fixture which can hold the nanwire in place.

Figure 4.16(a) shows a silver nanorod with length of 1.3μm and diameter of 100nm (aspect ratio of $\sigma = 13$). First, a trench, as a holder for the nanorod, can be created using the AFM tip by inscribing it into the surface. Figure 4.16(b) shows the real-time result displayed in the augmented reality interface. After a new scan, the

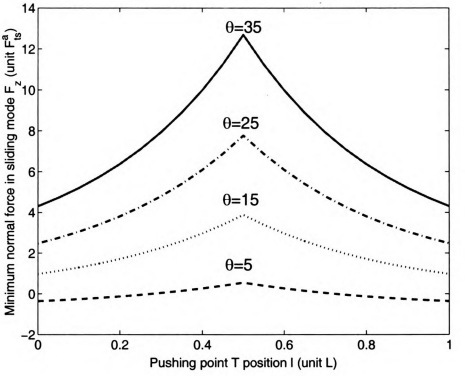

Figure 4.15. The minimum normal force, $\bar{F}_z$, to keep the tip on the surface in sliding mode as a function of θ and l (The unit of $\bar{F}_z$ here is F^a_{ts}. Assume $F^a_{os} = 50F^a_{ts}$, and $\nu = 0.2$).

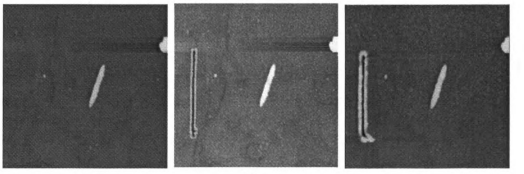

(a) (b) (c)

Figure 4.16. (a) A silver nanorod with diameter of 100nm and length of 1.3μm on a smooth polycarbonate surface in scanning range of $5\mu m \times 5\mu m$. (b) Image displayed in the augmented reality interface. A trench as a fixture is created on the surface by inscribing the tip into the surface. (c) AFM image by a new scan after the trench has been created.

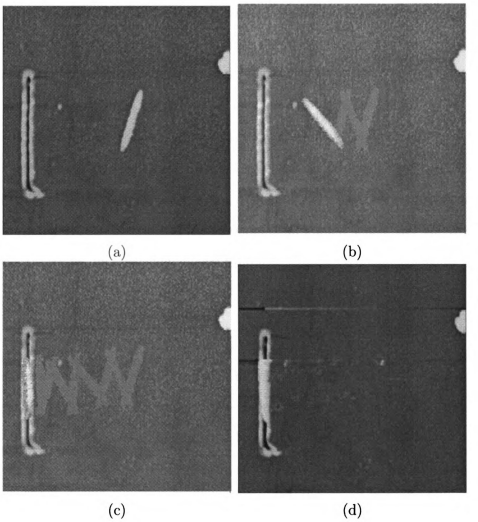

Figure 4.17. (a) AFM image by a new scan after the trench has been created. The scanning range is $5\mu m \times 5\mu m$. (b)-(c) Image displayed in the augmented reality interface: The pushing operation drives the wire into the fixture. (d) AFM image by a new scan after the final pushing operation.

image is shown in Figure 4.16(c). A trench with length of 2.8μm has been created as a fixture. It can be shown that the new AFM image is almost the same as the image captured from the augmented reality interface.

Then, the nanorod can be pushed into the trench. In order to push the nanorod, a zigzag strategy has to be used according to the theoretical analysis in Section

4.3.1. As shown in Figure 4.17(b), the shadows left by the nanorod indicate that the nanorod moves in a zigzag fashion. The real result from a new AFM image as shown in Figure 4.17(c) matches the results displayed in the augmented reality interface as shown in Figure 4.17(d).

From this experimental study, it can be seen that assembly of nano-structures using the AFM based nano-robotic system becomes very easy with the assistance of the augmented reality interface. The experimental results prove the efficiency and the effectiveness of the newly developed system.

4.4 Discussions

It is well known that the main difficulty of nanomanipulation using AFM is the lack of real-time visual feedback. Fortunately, the newly developed nano-robotic system has solved this problem through an augmented reality enhanced interface which provides both real-time visual and force feedback for the operator during manipulation. The real-time visual feedback is achieved by locally updating the AFM image in real time based on physical models and measured force information during nanomanipulation. It has been shown that nano-particles and nanowires can be easily manipulated using the AFM based nano-robotic system assisted by the augmented reality interface. However, there are several issues associated with the system that are worth of further investigation.

4.4.1 Model Dependence of the System

Unlike manipulation in the macro-world, a lot of information during nanomanipulation is unavailable. The system has to count on many experiments to develop a database, which can guarantee the effectiveness of the system. Once the database

has been built up, it becomes very convenient to use it. In the current stage, several models have been developed such as the nanolithography model on polycarbonate surface, interaction model of latex particles on glass surface and polycarbonate surface, and the interaction model of silver nano-cubes and nanorods on polycarbonate surface. Other nano-objects which are similar to these entities can take the same models but use different values of the parameters that only need a calibration.

4.4.2 Automated Manipulation

In order to further increase the efficiency and accuracy of AFM-based nano-assembly, automated CAD guided nano-assembly is desirable. In the macro-world, CAD guided automated manufacturing has been widely studied [65]. However, it is not a trivial extension from the macro-world to the nano-world. In nano-environments, the nano-objects, which include nano-particles, nano-rods, nano-wires, nanotubes and so on are usually distributed randomly on a substrate. Therefore, the nano-environment and the available nano-objects have to be modelled in order to design a feasible nano-structure. Manipulation of nanoparticles only requires translation while manipulation of other nano-objects such as nano-rods involves both translation and rotation. Therefore, manipulation of nanorods is more challenging than that of nano-particles. To generate a feasible path to manipulate nano-objects, obstacle avoidance has to be considered too. Turns around obstacles should also be avoided since turns may cause the failure of the manipulation. Because of the positioning errors resulted from the random drift, the actual position of each nanoobject has to be identified before each operation. Unfortunately, automated nano-assembly only receives little attention.

A path planning algorithm for the assembly of nano-particles is developed in [66], in which object assignment, obstacle detection and avoidance, path finding and

sequencing are discussed. However, the obstacles discussed in the paper are only polygons, which do not occur often in nano-environments. A drift compensation algorithm based on Kalman filtering has been developed in [50], but it can only estimate the drift in a short period of time. The problem of integrating the estimated drift into automated path planning is not discussed either. According to our knowledge, there is no research work on the automated nano-assembly of other nano-objects such as nano-rods.

In order for automated manipulation, a general framework for CAD guided automated nano-assembly using AFM is proposed in [67]. The collision-free paths are generated based on the CAD model, the environment model and the model of the nano-objects. The actual position of each nano-object can be obtained from the local scanning method to compensate for the random drift (refer to Chapter 5). The local scanning results are then integrated into the automated path planning system to adjust the planned collision-free paths. Since the building materials of nano-structures and nanodevices may include nano-particles, nano-rods, nano-wires, nanotubes and so on, automated path planning algorithms are developed for both nano-particles and nano-rods in the paper. The experimental results show that the developed general framework can be used to manufacture nano-structures more efficiently.

4.4.3 Fabrication of Nano-Devices

It is the first time to demonstrate that nanodevices are possibly fabricated by the AFM based nano-robotic system enhanced by augmented reality. The system enables us to simultaneously image, sense, and manipulate nano-objects *in situ*. All the experimental results show the effectiveness and efficiency of the developed system. The ability of the nano-robotic system to manipulate nano-particles, nano-wires, and nanotubes makes it an effective machine to fabricate nano-devices and nanosensors.

The potential application of this system is comprehensive and far-reaching to nanotechnology research. For example, single carbon nanotube (CNT) infrared detectors and single carbon nanotube transistors have been successfully fabricated in our lab using the nano-robotic system.

One of the key challenges for achieving CNT based infrared detectors is to enable connections between electrodes whose width of the gap is on nanometer scales. Thus, it is highly desired to have a reliable and repeatable way to form CNT electrical connection across electrodes. Current available methods in making CNT connections include direct CNT growth across electrodes [68, 69], deposition of as-grown CNTs on electrodes by dielectrophoresis [70, 71], fabrication of electrodes on top of as-deposited CNTs either by electron-beam (E-beam) lithography [72] or by shadow masks [73], and self-assembly of functionalizing CNTs onto electrodes with different chemicals or even DNA molecules [74, 75]. To a certain extent, these methods have their shortcomings in terms of repeatability, mass production, and ability in eliminating uncertainties.

For direct growth process, directional aligned CNTs can be formed. However, it would be hard to ensure and form a single CNT connection at specified locations if a single seed cannot be placed at that position. There is no way to repeat the growth process by resulting in exact the same CNT connections since CNT growing process is fundamentally a random process. By using dielectrophoresis or self assembly methods, bundles of CNTs could be formed across electrodes. The size of the bundles depends highly on the concentration of CNTs dispersed in solvents. This could be the major uncertain factor in this deposition process. E-beam lithography and shadow masks could give us the single CNT connection. However, due to the random deposition process of CNTs on top of a substrate, CNTs positions cannot be specified

once they are stuck onto substrates. Thus, it is highly desired to have an efficient way to fabricate CNT connections in a controllable and repeatable manner. The AFM based nano-robotic system can serve this purpose because it can directly link up the macro to the nano world. It enable us to directly manipulate nano objects to the desired position. It is obvious that the assembly of the CNT-based single-pixel infrared detector is the key step in fabrication of the infrared detector array. Figure 4.18 shows that one of the randomly distributed CNTs is aligned between the electrodes and the undesired one has been pushed away by the nano-robotic system.

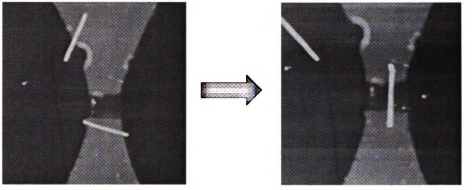

Figure 4.18. One of the randomly distributed CNTs is aligned between the electrodes and the other unwanted CNT is pushed away from the electrode

After a single pixel detector has been fabricated by aligning a multi-wall carbon nanotube between two electrodes, its I-V behavior has been characterized through a low current meter (Keithley Picometer 247). The measurement results are shown in Figure 4.19. It clearly shows that the CNT aligned between the electrodes is semiconducting CNT. The photoconductivity of CNT can be further studied by measuring the current changes at constant voltage mode. As shown in Figure 4.20, the current passing through the CNT (biased at 0.5V), has been significantly increased when pointing the infrared laser beam to the detector.

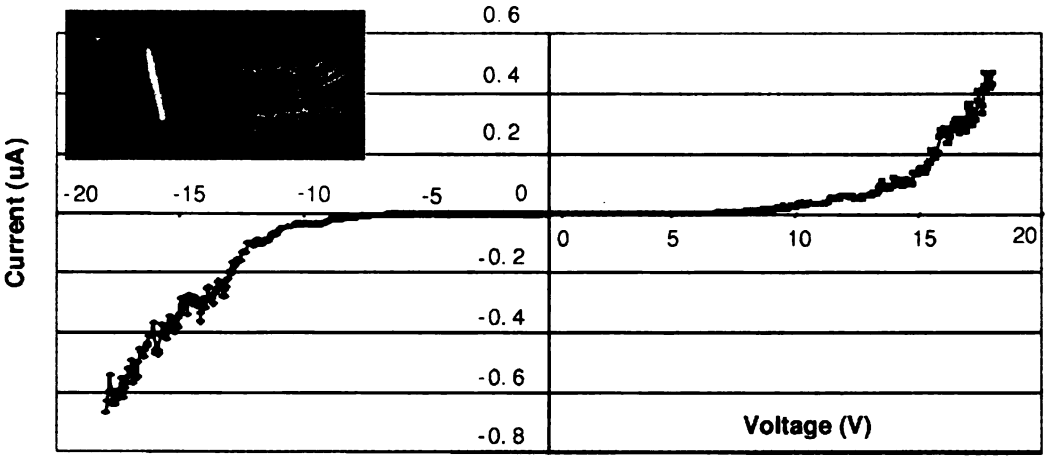

Figure 4.19. The I-V behavior of a multi-wall carbon nanotube between electrodes

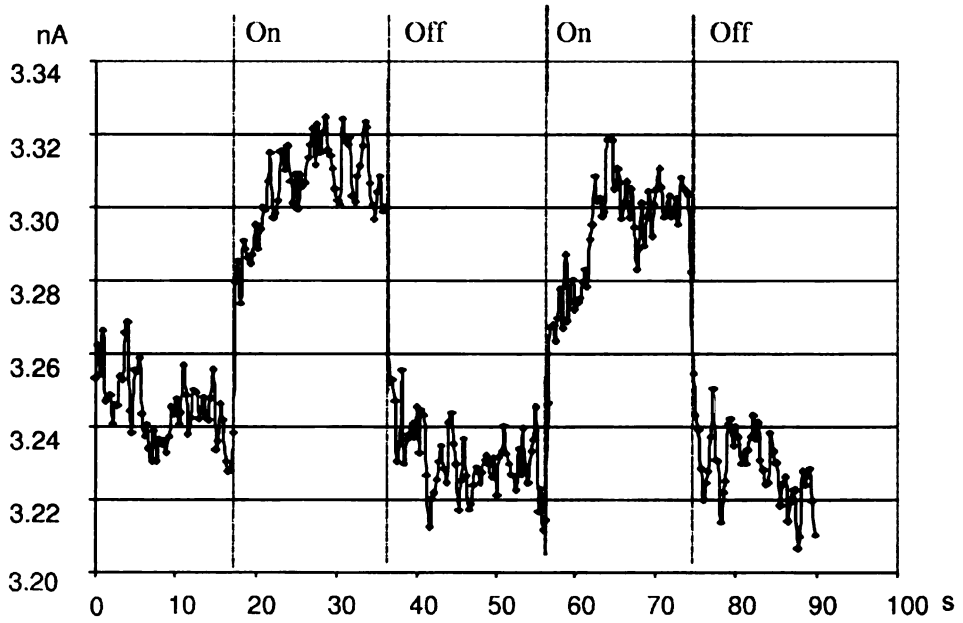

Figure 4.20. The response of detector when exposed to infrared laser source, the constant bias voltage is 0.5V

4.4.4 Applications in Biological and Biomedical Research

The dexterity of the AFM based nano-robotic system in nano-fabrication has been clearly demonstrated in the previous discussion. Its flexibility in biological and biomedical research will be further discussed in next several chapters. For exam-

ple, the AFM probe that functions as the robotic arm is deft enough to manipulate the tiny bio-molecules such as DNA. A real-time visual feedback is also possible by carefully modelling the motion behaviors of DNA molecules (refer to Chapter 6). Because AFM probes are very sharp and some of them have very high aspect ratio, nano-robotic arm is also possible to function as a scalpel to operate on individual cell when the cells are still alive (refer to Chapter 7). Although an identical real-time visual feedback is not applicable at current stage, the rough estimation and the precise display of the tip location usually provide enough assistance to accomplish the operation. In the future, it is possible to achieve an authentic real-time visual feedback if the cell deformation can be accurately modelled.

4.5 Summary

In this chapter, the physical models for different nano-objects have been developed. For nano-particles, only translation model are necessary, while for nano-wires or nano-rods, both translation and rotation have to be considered. As long as the behavior model of the nano-objects has been obtained, how they move can be predicted. However, in order to know when to move or how much force is needed to drive them to move, further analysis of the force interaction among tip, object, and sample surface is necessary. After the force model is clear, the movement of the nano-objects under manipulation can be easily predicted. The experimental results not only verify the validity of the developed models, they also prove the efficiency of the system. Improving the efficiency of the system by automated manipulation is discussed in the previous sections. Further development of the system by local scan will be discussed in next chapter.

CHAPTER 5

Improving Reliability by Local Scan

5.1 Introduction

In the previous chapter, the physical models of different nano-objects have been developed. All these models are crucial for the real-time image updating because different nano-objects have different behaviors during manipulation. The real-time visual feedback finally becomes possible. However, some inevitable position errors still cause problems for the visual feedback during manipulation. For example, the random drift is very difficult to predict. Operation often fails due to the thermal drift. Some other uncertainties such as losing objects during manipulation also cause troubles for image updating.

The random drift due to the thermal extension or contraction of the AFM system causes a major problem in nanomanipulation because the object may be easily lost during manipulation. Before the manipulation, the objects on the surface are identified and their positions are labelled based on a previously

captured AFM image. However, due to the random drift, the labelled positions of the nano-objects have errors after the AFM system switching from the imaging mode to the manipulation mode. To eliminate the effect of the random drift, the actual position of each nano-object has to be recovered before each operation. A drift compensation algorithm based on Kalman filtering has been developed in [50], but it can only estimate the drift in a short period of time. In order to overcome this problem completely, a local scan mechanism is proposed in this chapter.

A quick local scan action (as described in the following discussion) is performed first to obtain the actual initial position of each nano-object in a short time, and then an operation is performed immediately after the local scan. Another quick local scan after each operation is performed again to correct the ending position of the nano-object. The local scan will make the movie-like image display reliable and accurate, especially for the starting and ending positions. Nano-particles, nano-rods, nanotubes, and nanowires are the most often used materials for AFM based nano-manufacturing. Most nano-objects used for nano-manufacturing usually have nice and regular shape such as nano-crystals, nanowires, carbon nanotubes, and DNA molecules. The local scan mechanism for rigid nano-objects such as nano-particles and nano-rods is explained in detail in the following discussions. The local scan mechanism for flexible nano-objects such as nanotubes, nanowires, DNA molecules are still under investigation.

5.2 Local Scan of Nano-Particles

The location of a nano-particle can be approximately represented by its center and radius. The radius of each particle, R, is identified from a previously captured AFM image before the manipulation starts. Due to the thermal drift and model errors,

the displayed position may not exactly match the actual position. The actual center of a nano-particle can be recovered by two local scan actions before and after each manipulating operation. The local-scan-before-operation can eliminate the thermal drift, while the local-scan-after-operation mainly minimizes the effects of model errors–correcting the final position of the nano-particle.

The local-scan-before-operation needs at least two scanning lines, one or more horizontal lines and one vertical line as shown in the left part of Figure 5.1. First, the nano-particle is scanned using Line L_0, which passes through point O, the displayed center of the particle in the image. If the particle is not found, then the scanning line moves up and down alternatively by a distance of $3/2R$ until the particle is found. Once the particle is found, the scanning line forms two intersection points with the boundary of the particle, P_1 and P_2. Additional vertical line, V, which goes through the midpoint between P_1 and P_2 and perpendicular to the previous scanning line, is scanned to find the actual center of the particle. The vertical scanning line has two intersection points with the boundary of the particle, Q_1 and Q_2. The actual center of the nano-particle, O_a, is located at the midpoint between Q_1 and Q_2. The local scanning range (the length of the scanning line, l) is determine by the maximum random drift such that $l > R + r_{max}$, where r_{max} is the maximum random drift distance.

The local-scan-after-operation has to be performed immediately after each manipulating operation in order to correct the position errors in the real-time display. At least two scanning lines are needed for the local-scan-after-operation as shown in Figure 5.1. First, the nano-particle is scanned using Line L_0', which passes through the actual initial center and along the tip motion direction. If the particle is not found, then the scanning line moves up and down alternatively by a distance of $3/2R$

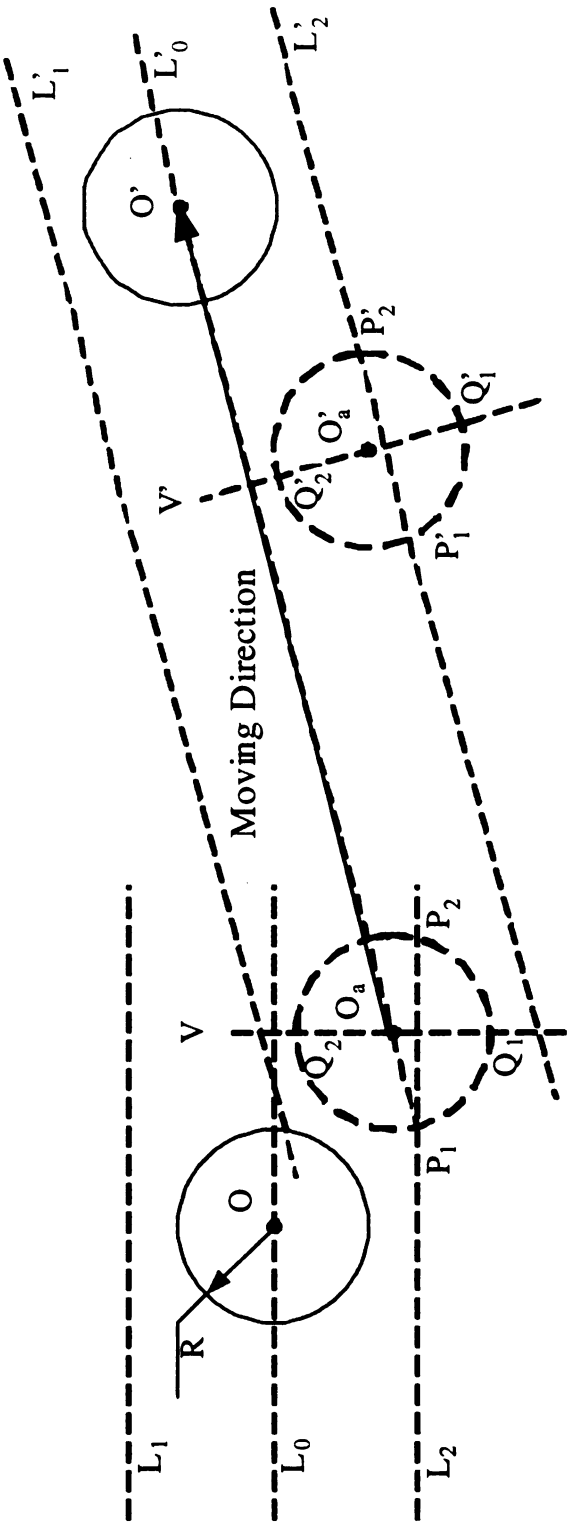

Figure 5.1. Local scan pattern to recover the actual center of a nanoparticle. R is the radius of the particle; O is the displayed initial center of the particle; O_a is the actual initial center of the particle; L_0, L_1, and L_2 are the horizontal scan lines; V is the vertical scan line. P_1 and P_2 are the interactions between the particle edge and a horizontal scan line; Q_1 and Q_2 are the intersections between the particle edge and the vertical scan line; O' is the displayed final center of the particle; O'_a is the actual final center of the particle; L'_0, L'_1, and L'_2 are the lateral scanning lines along pushing direction; V is the scanning line perpendicular to the pushing direction. P'_1 and P'_2 are the interactions between the particle edge and a lateral scanning line; Q_1 and Q_2 are the intersections between the particle edge and scanning line V. The arrow indicates the pushing direction.

until the particle is found. Once the particle is found, the scanning line forms two intersection points with the boundary of the particle, P_1' and P_2'. Another line, V', which goes through the midpoint between P_1' and P_2' and perpendicular to the previous scanning line, is scanned to find the actual center of the particle. The last scan line has two intersection points with the boundary of the particle, Q_1' and Q_2'. The final actual center of the nano-particle, O_a', is located at the midpoint between Q_1' and Q_2'. The local scanning range (the length of the scanning line, l') is determine by the maximum random drift and the pushing distance such that $l' > \Delta + 2(R + r_{max})$, where Δ is the pushing distance. The visual display is updated immediately after the actual position is obtained. The updated position will work as the new reference for the next operation on the same particle. The system is ready for next manipulating operation after updating the image with the final actual position of the manipulated nano-particle.

5.3 Local Scan of Nano-Rods

Although the position of a nano-rod is represented by its center, length and orientation in the behavior models, the location of a nano-rod is represented by its width and two ends in local scan for convenience. The center, length and orientation can be easily calculated from its width and two ends. The initial displayed rod width and ends are identified from a previously captured AFM image before the manipulation starts. Due to the thermal drift and model inaccuracy, the displayed position may not represent the actual position. The thermal drift usually causes translational errors, while the model inaccuracy causes both translational and orientational errors significantly. The actual two ends of a nano-rod can be recovered by two local scan actions before and after each manipulating operation. The local-scan-before-operation eliminates the thermal drift, while the local-scan-after-operation mainly

minimizes the effects of model errors–correcting the final position of the rod.

The local-scan-before-operation needs at least two scanning lines, one or more lines perpendicular to the rod orientation and one line parallel to the rod orientation, as shown in the left part of Figure 5.2. First, the nano-rod is scanned using Line L_0, which passes through the displayed center of the rod and perpendicular to the rod orientation. If the rod is not found, then the scanning line move up and down alternatively by a distance of $1/4L$ until the rod is found, where L is the rod length. Once the rod is found, the scanning line forms two intersection points with the boundary of the rod, P_1 and P_2. Another line, V, which goes through the midpoint between P_1 and P_2 and parallel to the rod orientation, is scanned to find the actual two ends of the rod. The scanning line, V, has two intersection points with the boundary of the rod, Q_1 and Q_2. These two points are the actual two ends of the rod. The actual rod center, orientation can be calculated correspondingly. The pushing operation will be performed immediately based on the actual position of the rod. The local scanning range (the length of the scanning line, l) is determine by the maximum random drift such that $l > d + r_{max}$, where d is the rod width.

For the local-scan-after-operation, at least three scanning lines are needed as shown in the right part of Figure 5.2. First, the nano-rod is scanned using Line L_0', which passes through the initial pushing point, T, and along the pushing direction, $\overline{O_a O'}$, as shown in Figure 5.2. If the rod is not found, then the scanning line goes along the line $\overline{O_a O'}$. If the rod is still not found, the scanning action continues by moving the scan line up and down by a distance of $1/4L \sin\alpha$ until two scan lines can locate the rod, where α is the angle between the pushing direction and the initial rod orientation. Each of the two scan lines has two intersection points with the boundary of the rod. For example P_1' and P_2' for L_0', P_3' and P_4' for L_1'. Another line,

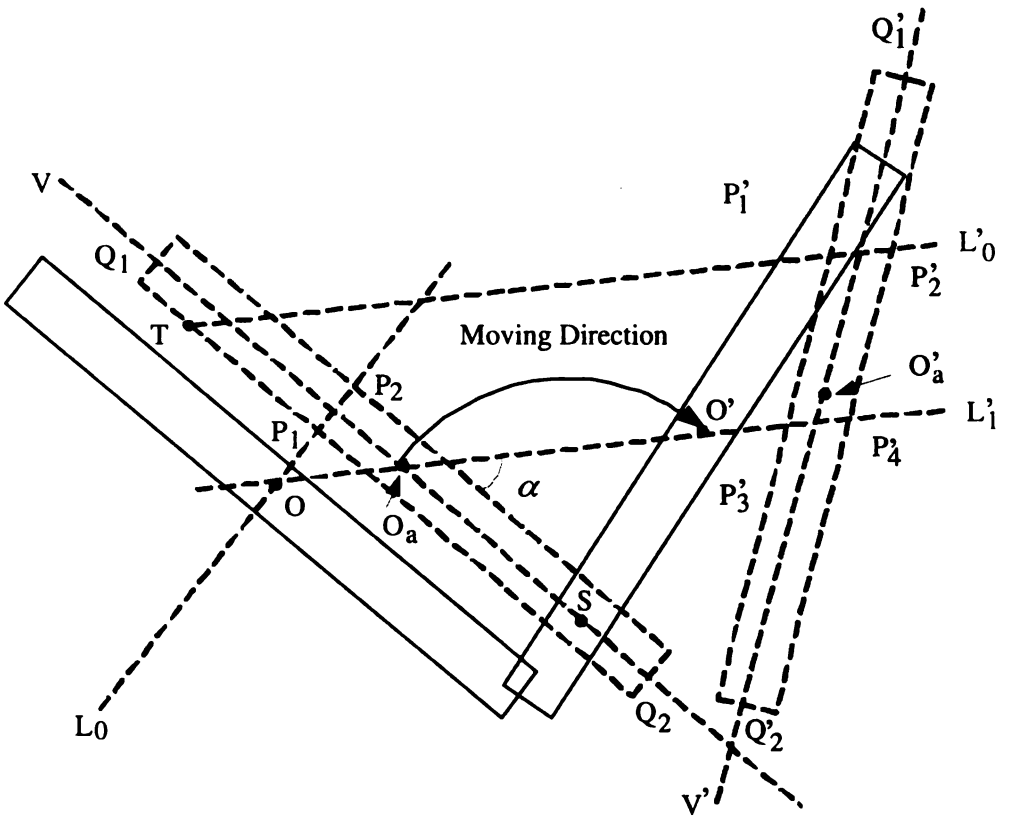

Figure 5.2. Local scan pattern to recover the actual position of a nano-rod. O is the displayed initial center of the nano-rod; O_a is the actual initial center of the nano-rod; P_1 and P_2 are the interactions between the rod edge and the scan line L_0; Q_1 and Q_2 are the actual initial ends position of the nano-rod; O' is the displayed final center of the nano-rod; O'_a is the actual final center of the nano-rod; P'_1 and P'_2 are the interactions between the rod edge and the scan line L'_0; P'_3 and P'_4 are the interactions between the rod edge and the scan line L'_1; Q_1 and Q_2 are the actual final ends position of the nano-rod; The arrow indicates the rod motion direction according to the behavior model; T is the pushing position; S is the pivot during pushing; α is angle between the initial orientation and the pushing direction.

V', which goes from the midpoint between P'_1 and P'_2 to the midpoint between P'_3 and P'_4, is scanned to locate the two actual ends of the rod. The scanning line, V', has two intersection points with the boundary of the rod, Q'_1 and Q'_2. These two points are the actual ends of the rod. The local scanning range (the length of the scanning line, l') is determine by the maximum random drift and the pushing distance such

that $l' > \Delta + 2(d + r_{max})$, where Δ is the pushing distance (the tip moving distance during pushing). The visual display is updated immediately after the actual position obtained. The updated position will work as the new reference for the next operation on the same rod. The system is ready for next manipulating operation after updating the image with the final actual position of the manipulated nano-rod.

5.4 Implementation of Local Scan

In order to realize the proposed local scan algorithm, the original system structure has to be modified. Some signals belonging to the scanning mode need to be accessed. The architecture of the modified system is shown in Figure 5.3. The modules of the manipulation and the local scan are implemented in the windows PC system, which communicates with the Linux system through Ethernet. The Linux system samples analog signals and outputs control signals through an A/D (D/A) card.

When the system runs in manipulation mode, a digital signal is sent to the Linux system first, and then the Linux system turn off the tapping signal via a switch through the DO port. The position control signals X1, Y1 and Z1 are sent to the amplifiers through the D/A card. During manipulation, the position control signals X, Y and Z from AFM PC are set to zero. The AFM scanner is controlled by the manipulation module at current stage.

When the system runs in local scan mode, the tapping signal is turned back on by the switch and the cantilever backs to tapping mode. At the same time, the internal scanner feedback in Z direction is turned on by the Nanoscript (comes with the AFM software package from Veeco Instruments, Inc). The actual position X0, Y0, Z0, and the amplitude signal RMS (root mean square) are read through the A/D card and

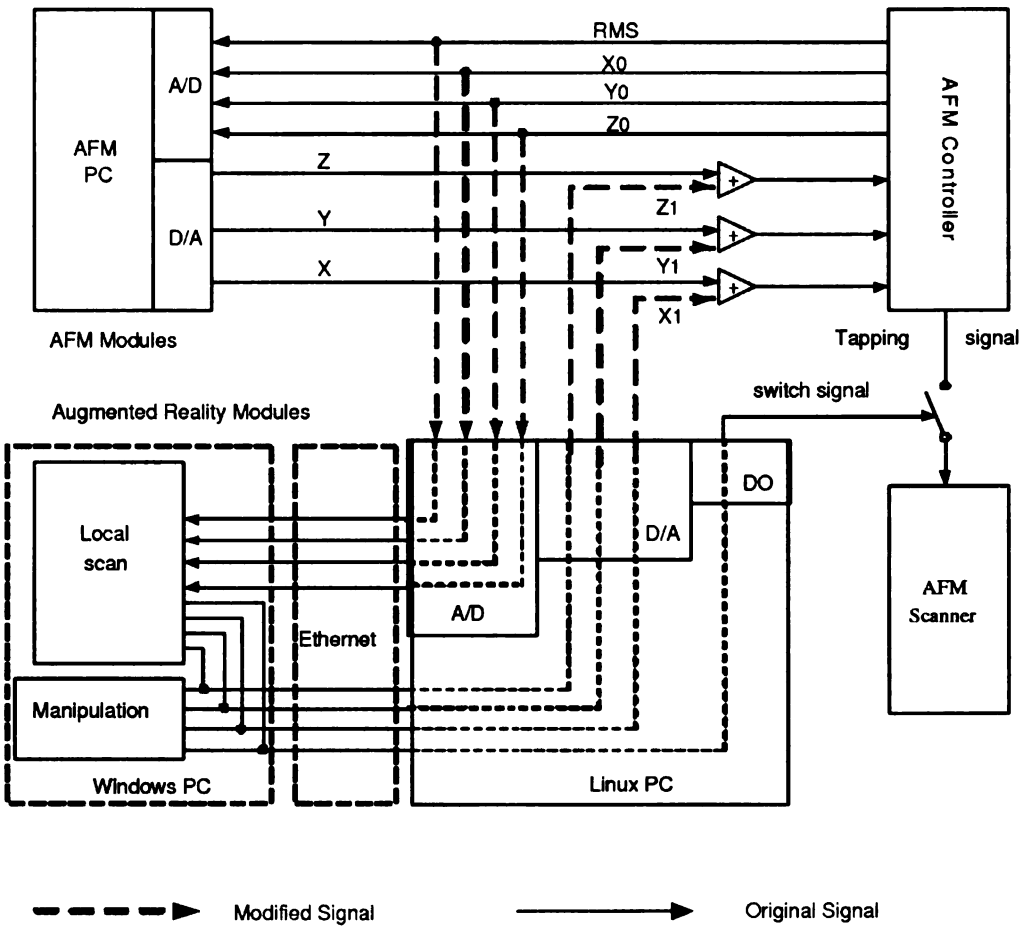

Figure 5.3. Architecture of the modified system

then passed to the local scan module. The local scan module sends out the position control signal based on the local scan pattern. The actual position X0, Y0, Z0 of the scanner are recorded during local scan. These information can be used to recover the actual position of the nano-objects.

5.5 Experimental Verification

In order to verify the proposed scanning strategies and the modified system, both manipulation of nano-particles and nanorods with local scan are performed.

The first experiment is the manipulation of nanoparticles with local-scan-after-operation. As shown in Figure 5.4(a), a particle is pushed from one location to another location. A scanning pattern is generated as shown in Figure 5.4(b). The local scan results are shown in Figure 5.5. From the local scan information, the actual position of the nano-particle can be easily recovered by the particle center defined by the second scan line.

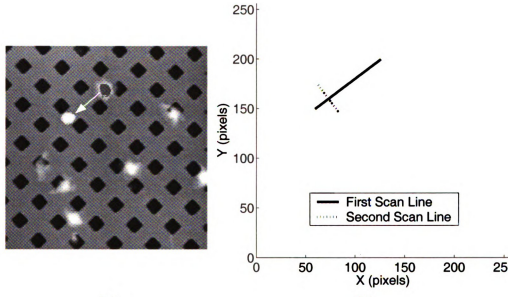

Figure 5.4. (a) A nano-particle with diameter of 150nm is pushed form one location to another location. The scanning range is $10\mu m \times 10\mu m$. (b) The local-scan-after-operation pattern for particle generated according to the strategies.

The second experiment is the manipulation of nanorods with local-scan-after-operation. As shown in Figure 5.6(a), a nanorod is pushed from one end and the nanorod rotates around the other end as predicted by the model in the previous chapter. A scanning pattern is generated as shown in Figure 5.6(b). The local scan results are shown in Figure 5.7. From the local scan information, the actual position of the nanorod can be easily recovered by the two rod end positions obtained from

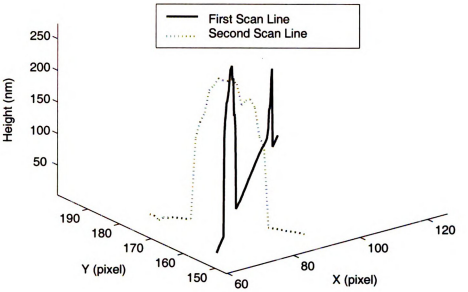

Figure 5.5. The local-scan-after-operation results of a nano-particle

the third scan line.

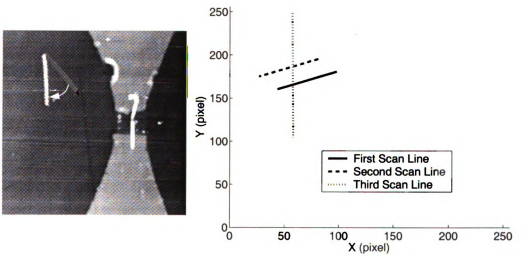

(a) (b)

Figure 5.6. (a) A nanorod with diameter of 100nm is pushed from one end and the nanorod rotate around the other end. The scanning range is $10\mu m \times 10\mu m$. (b) The local-scan-after-operation pattern for nanorod generated according to the strategies.

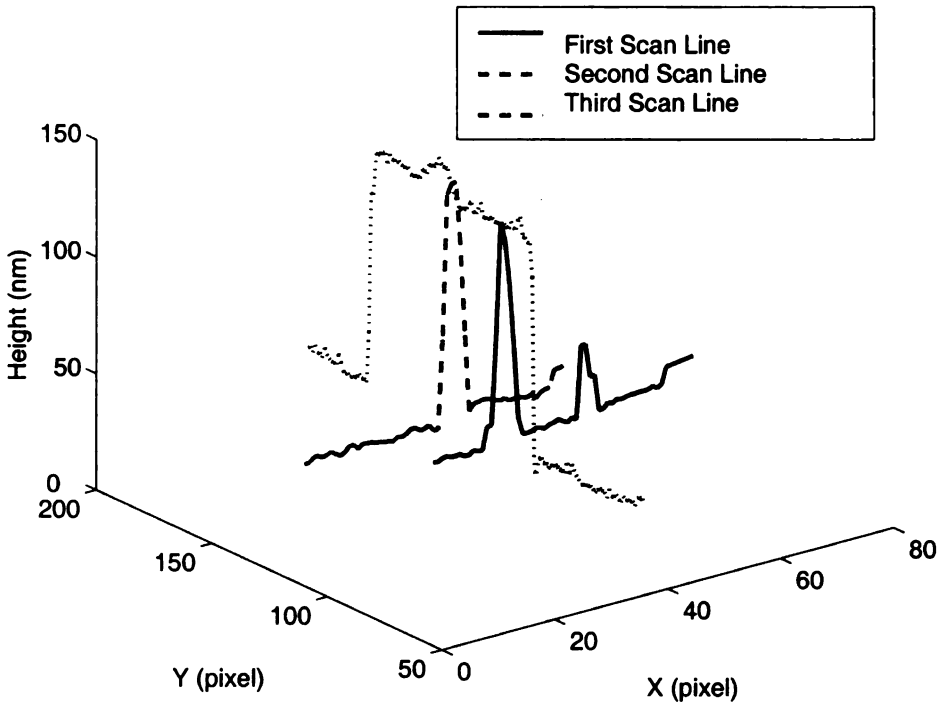

Figure 5.7. The local-scan-after-operation results of a nanorod

5.6 Summary

In this chapter, a local scan mechanism is proposed to deal with the position errors due to thermal drift and the uncertainties during manipulation. The local scan patterns for both nano-particles and nanorods have been developed. The local scan module has been integrated into the AFM based nano-robotic system. Its effectiveness has been proven by the experiments.

CHAPTER 6

Study of DNA Properties Using the Nano-Robotic System

6.1 Introduction

DNA plays a key role in biology as a carrier of genetic information in all living species. The Watson-Crick double-helix structure of DNA has been known for almost 50 years. During the last half century, the majority of research in DNA has been devoted to its biological properties, especially its role in genetic inheritance, disease, aging, RNA synthesis, and mutation. Recently, the DNA molecule has drawn much attention in engineering applications because of its appealing features for use in nanotechnology: it's minuscule size, with diameter of about 2.4 nm, and its short structural repeat of about 3.4-3.6 nm [76]. The desire to use DNA as the ultimate building blocks of electronic circuits has motivated the studies on DNA electrical properties and DNA manipulation.

In 1962, D. D. Eley and D. I. Spivey first suggested that DNA could serve as an electronic conductor [77]. The initial model for electron transfer through

DNA is based on overlapped π-stack orbital in adjacent base pairs. After much initial controversy over the past 15 years, the mechanism of charge-transfer is now moving towards a consensus view in the chemistry community [78]. The dominant charge-transfer mechanism in DNA appears to be distance-dependent coherent tunnelling through unit-step and weak-distance-dependent thermal hopping through multi-step [79]. Both charge-tunnelling and thermal-hopping have been verified in [80]. Contrary to the consensus in the chemistry society, the problem of whether DNA is conducting or insulating remains to be hotly debated among physics groups due to the disparate experimental results. A lot of experiments have been performed to measure the conductivity of DNA from indirect methods to direct methods (physical contact). Most indirect results suggest that DNA is a good conductor by microwave cells method [81], fluorescence quenching [82] and resonant cavity measurments[83], but only few results prove that it is insulating by measuring its dielectric property [84]. For direct measurement (with physical contact), the results are even more controversial. Some results suggest that DNA is a good conductive molecule wire [85] or even a super conductor at low temperature [86], some report that DNA is a semi-conductor [87, 88, 89, 90], while others find that DNA behaves as an insulator [91, 92, 93].

Due in part to the difficulty of individually connecting a single DNA molecule to an electrode, the results of almost all experiments are not repeatable. The only way to obtain a reliable measurement result is to make the experimental process repeatable and in a controlled environment. Therefore, having an efficient way to individually manipulate DNA molecules is a key to DNA electronics circuits. DNA is a random coil in solution and it needs to be elongated, cut and fixed on a solid surface. Many methods have been used in the alignment of DNA, for example, surface tension [94], dielectrophoretic force [95, 96, 97], viscous drag [98], laser

trapping [99]. However, all these methods are still far from the requirement of accurately positioning DNA and building it into circuits.

In this chapter, the DNA molecules are manipulated by the recently developed nano-robotic system with enhanced augmented reality. Using the system, the DNA can be cut, deformed, elongated, or manipulated to a desired location. In order to performed the manipulation, the behavior model of DNA molecules is provided to update the real-time visual display in the augmented reality interface.

6.2 DNA Sample Preparation

Further investigation shows that the heavy water adsorption of DNA molecules, due to the negatively charged backbone of the DNA helix structure, causes a strong adhesive force between DNA molecules and a hydrophilic surface. The strong adhesive force may destroy the double helix structure of the DNA molecules. By measuring the height of a single DNA molecule, it has been found that there is very large compression deformation of the deposited DNA on the most commonly used substrates such as the mica and silicon oxide surface [100]. According to [101], the thickness of DNA molecules on a silicon substrates treated by pentylamine is about 2.4 nm while the thickness is about 1.1 nm on a clean substrate. Therefore, DNA molecules are deposited on a hydrophobic surface or a silanized quartz surface in order to avoid the compression deformation due to the adhesive force. A detailed protocol to treat SiO_2 surface is provided in Appendix A.

In the study of DNA electrical conductivity, most researchers use commercial DNA samples with identical length and identical base-pair sequence such as λ-Phage DNA. However, this may cause problems since DNA has almost unlimited base-pair

sequences in nature and the nature of the sequence and length may affect its electrical conductivity. Another problem for the commercial DNAs is that they are stored in Tris-HCl and EDTA (ethylenediaminetetraacetic acid) solvent. These chemicals inevitably affect the electrical properties. Therefore, instead of using commercial DNA samples, raw DNA samples with random length and random base-pair sequences are used in this research. The DNA sample was collected from mature seeds of peony species without restriction (cutting), therefore, some DNA molecules still keep their original length (Department of Plant Biology at Michigan State University). The AFM images of the DNA samples on a hydrophobic polycarbonate surface are shown in Figure 6.1.

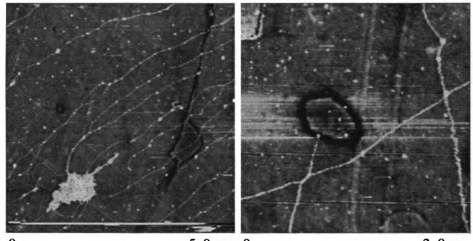

Figure 6.1. AFM image of DNA samples: (a) Image of DNA sample in scanning range of 5um. Most DNA molecules are longer than 5um. (b) Image of DNA sample in scanning range of 2um.

6.3 Manipulation of Single DNA Molecules

In order to compare the electrical conductivity of DNA molecule in its different shape, kinks and deformation of DNA molecules can be created artificially using the AFM based nano-robotic system. By controlling the pushing force between the tip and sample surface, the DNA molecules or DNA bundles can be either broken or deformed as shown in Figure 6.2. A large pushing force in normal direction usually breaks the DNA molecule, and a small pushing force may only deform the DNA molecule without breaking it. In Figure 6.2(b), the big scratches on the surface indicate large pushing force applied on the AFM tip, and small scratches imply small pushing force used. We can see that the DNA bundle was broken when a big pushing force was applied but only deformed when a small pushing force was applied.

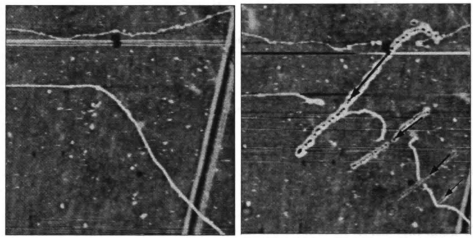

(a) (b)

Figure 6.2. (a). The AFM image of DNA ropes in its original shape. (b) The DNA ropes are cut by the AFM tip. The pushing force can be controlled in order to cut the DNA rope or only deform the DNA rope. The big scratches on the surface indicate strong pushing force applied, and small scratches imply small pushing force used. The arrows indicate the pushing directions.

In order to real-time display the deformation of DNA molecules or bundles

in the augmented reality interface, the deformation model of DNA molecules and bundles has to be found. However, it is not a trivial problem to model DNA. The well-accepted worm like chain model is to model DNA in liquid condition [102]. There are still no effective model for DNA on a substrate surface in the air. The molecular dynamics may provide a possible solution, but the calculation may be too slow for real-time response. Therefore, instead of using mathematic model for the force-deformation of DNA molecules, an empirical method, as shown in Figure 6.3, is employed in this research to predict the deform of DNA molecules during manipulation.

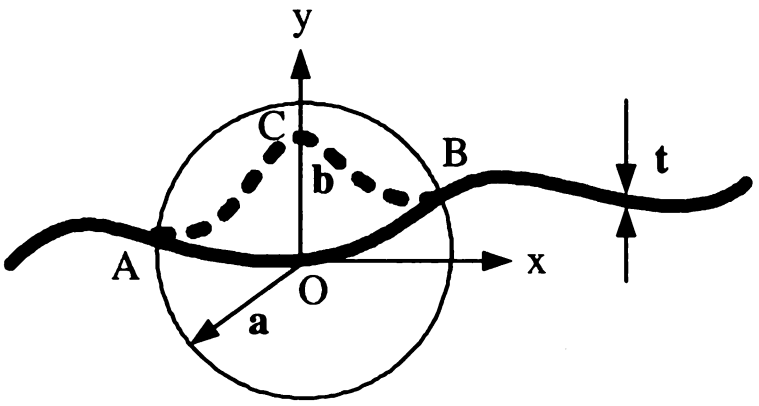

Figure 6.3. Modelling the deformation of DNA molecules and bundles when pushing by AFM tip. The solid curve is a DNA molecule (or DNA bundle) in its original status. The dash curve is the new status of the DNA molecules. The DNA molecule (bundle) is pushed by the AFM tip from the start point O to the end point C. The DNA molecule (bundle) is only deformed within an affecting region from point A to B, which is bounded by a circle with radius of a. t is the thickness of the DNA molecule (bundle).

As shown in Figure 6.3, the DNA molecule (or bundle) is pushed by the AFM tip from the start point O to the end point C. The DNA molecule (or bundle) is only deformed within an affecting region from point A to B, which is bounded by a circle

with radius of a. a is determined by following empirical function f:

$$a = f(b, t)$$

where, b is the pushing distance before DNA broken, and t is the thickness of DNA itself. In order to display the DNA deformation in real time, a local coordinate system is defined such that y axis is along the pushing direction. The original shape of DNA inside the affecting circle can be removed first and then the new shape of DNA can be redisplayed through a 4th order polynomial function with respect to the local coordinate system. Define (x_A, y_A), (x_B, y_B) and (x_C, y_C) as the positions of points A, B and C; and also define v_A and v_B as the slopes of the tangent at points A and B. Then the 4th order polynomial function can be found as

$$y = a_4 t^4 + a_3 t^3 + a_2 t^2 + a_1 t + a_0$$

where

$$t = \frac{x - x_A}{x_B - x_A}$$

and the coefficients can be found through following equations

$$\begin{bmatrix} 0 & 0 & 0 & 0 & 1 \\ 0 & 0 & 0 & 1 & 0 \\ 1 & 1 & 1 & 1 & 1 \\ 4 & 3 & 2 & 2 & 1 \\ t_m^4 & t_m^3 & t_m^2 & t_m & 1 \end{bmatrix} \begin{bmatrix} a_4 \\ a_3 \\ a_2 \\ a_1 \\ a_0 \end{bmatrix} = \begin{bmatrix} y_A \\ v_A \\ y_B \\ v_B \\ y_C \end{bmatrix}$$

here

$$t_m = \frac{x_C - x_A}{x_B - x_A} = -\frac{x_A}{x_B - x_A}$$

It has been found that the AFM tip may slip across the nano-objects if the pushing force is not strong enough to keep the tip in contact with the surface [103]. Therefore, there exists a maximum value of b such that either the AFM tip slips across the DNA or the DNA is broken at that point. Namely,

$$b_{\max} = \text{Min}\{b_{\max}^1, b_{\max}^2\}$$

where $b^1_{\max}$ is determined by pushing force in normal direction F_n, DNA thickness t and surface properties. $b^2_{\max}$ is determined by DNA thickness t and surface properties. Unfortunately, these values have to be determined experimentally because it is almost impossible to obtain their mathematic models.

Using the model developed in this section, manipulation of DNA molecules can be real-time displayed in the augmented reality interface. An example of DNA manipulation is shown in Figure 6.4 in which Figure 6.4(a) shows the DNA molecules in their original shapes; Figure 6.4(b) shows the manipulation of DNA molecules displayed in the augmented reality interface; Figure 6.4(c) shows an AFM image after manipulation. It can be seen that several kinks have been created by slightly pushing the DNA molecules. The kinks created in the augmented reality environment are relatively identical to the real results.

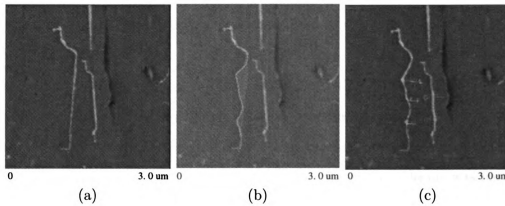

Figure 6.4. Pushing DNA on a polycarbonate surface (scanning range of 5um). (a) Image of DNA before pushing. (b) the real time display on the augmented reality during pushing; The kinks inside the circles are created by elaborately pushing. (c) A new scanning image after several pushing operations.

6.4 DNA Electrical Conductivity Measurement

In order to characterize the DNA conductivity, DNA ropes were suspended across holes in a gold-coated carbon grid and a tungsten tip was then used to make contact with the ropes in [85]. Using this method, Fink and Schönenberger measured a single rope of λ-DNA 600nm long, which indicated efficient conduction through the rope. Double-stranded DNA molecules were deposited by a combing process across a submicron slit between rhenium/carbon metallic contacts in [86]. In this paper, the measured resistance per molecule is less than 100 kΩ at room temperature. The results also indicates that DNA has good ohmic conduction behavior. Porath *et al* observed wide band gap semiconductor-like behavior for a single, double stranded DNA with only G-C base pairs sequence between two Pt electrodes with gap of 8nm in [88]. The semiconductor behavior of DNA is also observed by K.-H. Yoo and *et al* in [90] in which they measured the electrical transport through polyadenine-polythymine and polyguanine-polycytosine molecules containing identical base pairs between two electrodes with gap of 20nm. The gate-voltage dependence transport measurement by introducing a third electrode shows that polyadenine-polythymine behaves as an n-type semiconductor, whereas polyguanine-polycytosine behaves as a p-type semiconductor. The absence of dc-conductivity in λ DNA is observed by P.J. de Pablo and *et al* in [91]. In that experiment, the DNA molecule was partially covered by a gold electrode while the second electrode was a metallic atomic force microscopy tip. Since the thermal drift is quite significant, a reliable electrical contact between the tip and DNA is highly suspicious in this work. A series of experiments done by A.J. Storm in [92] prove that DNA is definitely an insulator at the length scale larger than 40nm. This result is clearly in disagreement with the work of [85] and [86]. Until now, the conductivity of DNA remains controversial in the direct measurement experiments.

Indeed, the DNA molecule adopts many different structures which may affect the measurement results. These include kinks, bends, bulges and distortions along the molecule, as well as the flow of positively charged counterions along the negatively charged phosphate backbone. By measuring the height of a single DNA molecule, it has been found that there is very large compression deformation of the deposited DNA on the most common used substrates such as mica and silicon oxide surface [100]. In [101], the thickness of DNA molecules on the substrates treated by pentylamine is nearly 2.4 nm comparing to the thickness of 1.1 nm for DNA molecules on a clean substrate. Using atomic force microscopy (AFM) in spreading resistance mode, it has been found that the DNA is insulating on clean substrate but conductive on treated substrate. Another significant factor, which may affect the measurement result, is perhaps the electrical contacts. Ideally, these contacts should be ohmic so that any no-linearity in the conductivity of the molecular wire can be correctly attributed and studied. It has long been recognized that to make good electrical contact between a molecule and a conducting electrode, a chemical bond is required [104]. Therefore, a chemical bond approach for electrical contact and manipulation instrument for elongating, deforming or cutting DNA play key roles in verifying the hypothesis that the shape and structures of DNA molecules affect their conductivity.

In order to verify the distance dependence of DNA conductivity, a series of electrodes with gaps from 50nm to 3um were fabricated on transparent substrates like quartz. The advantages of quartz substrate are its transparency for easily locating the electrodes through an inverted optical microscope. However, quartz surface is hydrophobic, which is not suitable for deposition of DNA on it. Therefore, special treatment such as hydophobization is necessary after electrode fabrication. The hydrophobic surface keeps DNA molecules in their original shape without strong com-

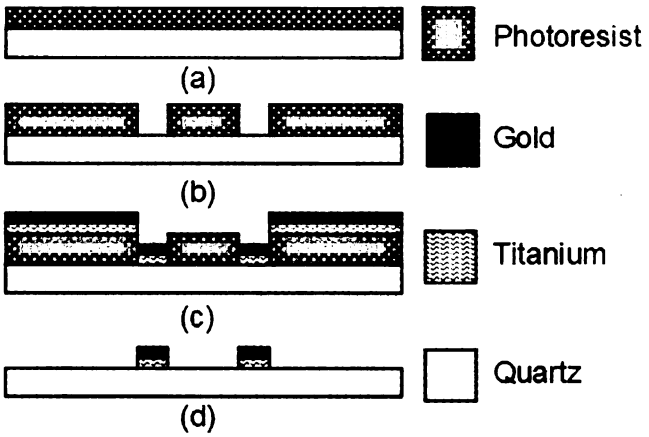

Figure 6.5. Fabrication process of microelectrodes on a quartz substrate.

pression due to adhesion force. The hydophobization process of quartz surface can be found in Appendix A.

6.4.1 Fabrication of Electrodes

Gold (Au) microelectrodes with gap distances around 2μm can be fabricated using a 5μm gap distance mask design by over-developing technique during image reversal process. The fabrication process of electrodes is shown in Figure 6.5. The process starts with a transparent quartz substrate (500μm). A 1.5μm thick photoresist (AZ5214E) was span on and patterned by an AB-M mask aligner as shown in Figure 6.5(a). The exposed areas were developed by AZ300 developer according to Figure 6.5(b). Then, a Gold (20nm)/Titanium (2nm) layer is deposited by an Edward Auto306 thermal evaporator as shown in Figure 6.5(c). The titanium layer was used to promote the adhesion between the gold and quartz substrate. This layer is patterned by lift off process. The photoresist underneath this layer is etched by acetone as shown in Figure 6.5(d). A pair of electrodes with gap of 1.5um fabricated by this method is shown in Figure 6.6(a).

Basically, it is a typical process for fabricating electrodes. But, in forming electrodes, lift off process was preferable rather than etching process because of the

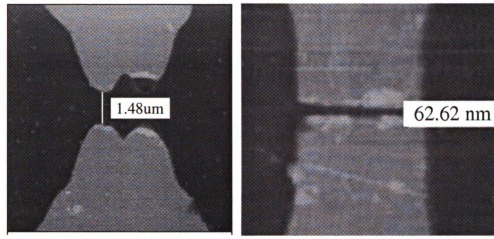

Figure 6.6. (a) AFM image of the electrodes fabricated on a quartz surface with a gap of 1.5um (10um scanning range); (b) AFM image of electrodes fabricated by AFM nanolithography on a gold coated quartz surface with a gap of 60nm (5μm scanning range).

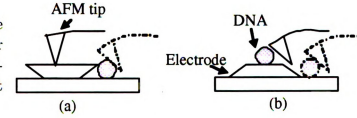

Figure 6.7. Illustrations of the overcome of pushing DNA over the electrodes which are fabricated by (a) etching and (b) lift off process

difference in the step profile between these two processes. The step profile of lift off process is better for later DNA pushing process. This idea is illustrated in Figure 6.7. DNA can easily be pushed up the electrodes for lift off case but not the etching case. The DNA may stuck in edge of the electrode and cannot be pushed up as shown in Figure 6.7(a).

The typical fabrication process is very efficient but it is very difficult to fabricate electrode with gap smaller than 1 μm. E-beam nano-lithography is a possible solution to fabricate a electrode gap smaller than 1 μm but it is a complicated and time-consuming process. Fortunately, the AFM itself can also serve as a nanolithography

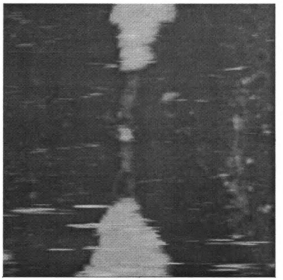

Figure 6.8. DNA bundles deposited across the electrode with gap of 1 μm. The scanning range is 2μm.

tool under the assistance of the augmented reality interface. By controlling the AFM tip through a haptic joystick to cut the electrode to make a gap, a very small electrode gap can be made on the gold coated surface. Figure 6.6(b) shows that a 60nm gap can be made by inscribing the AFM tip into the gold coated electrode. The thickness of gold coating is about 30nm, and it is prepared by the typical process discussed before. After mechanical lithography, the electrode is etched by a 10% HCl solution for 10 minutes to remove the Titanium in the gap. Before etching, there is a linear resistance of 15Ω between the electrodes. After etching, the resistance between the electrodes becomes almost infinite.

6.4.2 Electrical Conductivity of Bundle DNA

The DNA sample suspending in DI water was dropped on the electrodes and then applied an AC voltage across the electrodes for several seconds. The purpose of AC voltage applied on the electrodes is to help the deposition of DNA by dielectrophoresis, a method often used to attract small particles close the electrodes. After deposition of DNA, the electrode is blown with dry nitrogen. The success of DNA deposition is checked by AFM scan. If there is no DNA deposited near the neighborhood of

the electrodes, the process has to repeat. The DNA bundles are deposited across the electrodes with a gap of 1μm as shown in Figure 6.9(a). Further manipulation is often necessary to guarantee a proper contact with the electrodes. The resistance between electrodes becomes 180MΩ after depositing DNA sample. The I-V curves before and after deposition of DNA sample are shown in Figure 6.9(b) (The current is measured by a Picometer with resolution of 10 fA from Keithley Co.). This proves that DNA bundles are conductive in air condition.

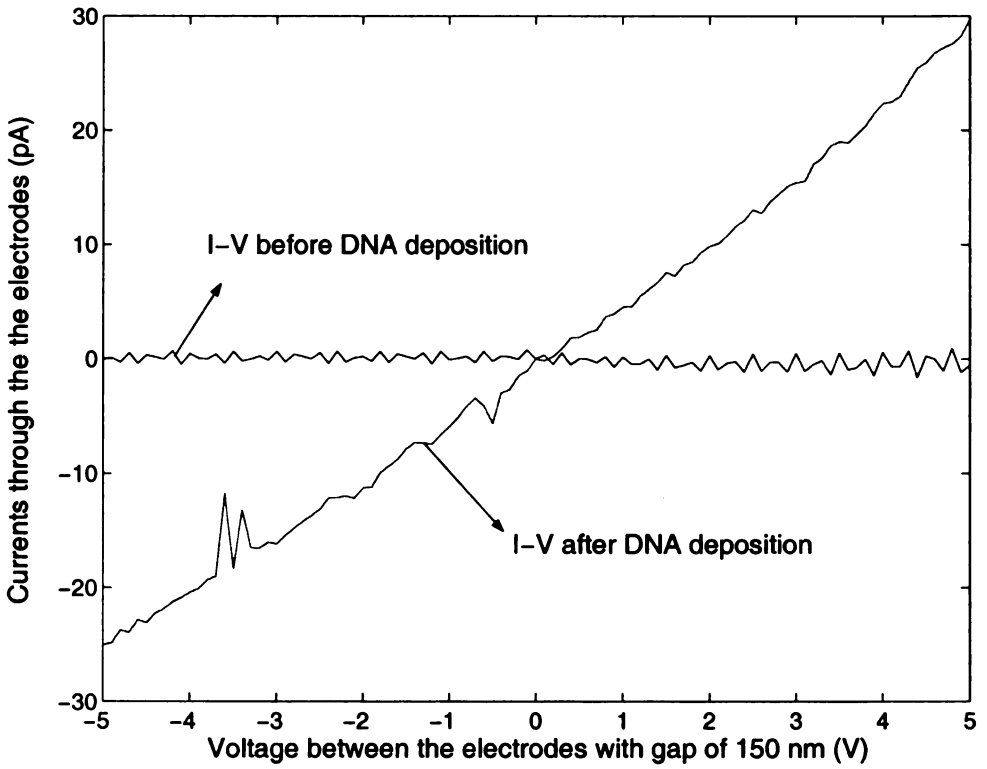

Figure 6.9. I-V curves before and after deposition of DNA sample on the surface

6.5 Discussions

The recent debate on DNA electrical conductivity requires more efficient experimental methods. Through cross verification based on a series of experiments, conclusive

evidences will be found to terminate the dispute on the electrical conductivity of DNA molecules. Considering the hydrophilic property of the DNA molecules, hydrophobization of the substrate surface is necessary in order to prevent the damage of the helix structure from the surface adhesion force. The protocol in Appendix A can treat a quartz surface (hydrophilic) and make it hydrophobic.

Because the DNA molecules are so small (less than 3nm in diameter), a fine electrode with thickness less than 10nm is necessary in order to observe the DNA molecules from the AFM image. Or else, if the electrodes are too high, the contrast may be not enough to make the DNA molecules visible.

Although the result shows that the DNA is conductive, the conductivity may be caused by the water molecules in air. Therefore, a vacuum condition is necessary to further study the electrical property of DNA molecules.

6.6 Summary

In this chapter, the DNA molecules are manipulated by the recently developed nano-robotic system with enhanced augmented reality. Using the system, the DNA can be deformed, elongated, and manipulated to a desired location. In order to performed the manipulation, the behavior model of the DNA molecules is provided to update the real-time visual display in the augmented reality interface. The electrical property of DNA molecules are also studied by measuring its resistance across the electrode.

CHAPTER 7

Cellular Imaging and Surgery

7.1 Introduction

Atomic force microscopy has been proven to be an efficient and powerful technique for surface science research. Astonishingly, it has been extended to the more complex field of biology shortly after its advent. Research efforts in the past few years have made AFM a potential powerful tool for biological and biomedical research, especially for cellular biology. Such rapid expansion of AFM application in cellular biology is ascribed to the fact that AFM offers several advantages over other conventional techniques used for biological study such as SEM (scanning electron microscopy) and TEM (transmission electron microscopy). For instances, AFM is capable of operating in several environments, including air, vacuum, and liquid. Most importantly, it can study the cells when they are still alive. Unfortunately, the image formed by AFM is based on the contact force between the tip and the sample, which is spontaneously suitable for hard surface but inept to soft surface like cells.

To study biological sample at very high spatial resolution is one of ostensible incentives to the applications of AFM in biological research, especially in the cellular

study in living condition. Until now, studies of living cells by AFM are still hindered by the cell deformation during imaging. Several approaches have been investigated to obtain high resolution images of soft biological materials such as low temperature method [18] and small contact force methd[19]. However, few of them are proven to be effective. The substantial improvement of imaging quality and stability by TMAFM (tapping mode AFM) [20] remains only a theoretical supposition. Contact mode in practice often provides better resolution for a given application such as when imaging relatively hard cells [22].

Although imaging living cells with high resolution by AFM is hampered by several obstacles such as cell deformation and tip contamination as well as cell's mobile predisposition, the potential benefits of AFM to study living cells as aforementioned still motivate us to face the challenges hoping to break through the barriers. Although the TMAFM is still under development, it remains the most promising approach considering its less destructive shear force. In this chapter, the techniques for improving the imaging quality of living cells are discussed, and the existing problems and possible solutions are provided. An example of imaging living neurons is also introduced in this chapter.

7.2 Tapping Mode in Liquid

Due to viscoelastic properties of the plasma membrane, the cell may harden when responding to externally applied high frequency vibration and hence is less susceptible to deformation. Moreover, with this imaging mode, the cantilever oscillates at its resonant frequency and is only in intermittent contact with the cell surface. As a result, the destructive shear force is minimized [15]. In practice, the tip of an AFM tends to get more contaminated and lose resolution with time while

operating in contact mode, especially when imaging adsorbable biological molecules. In contrast, the tip tends to recover after picking up contaminants in the tapping mode. Presumably, the accumulated material is vibrated off or left on the surface when the tip taps. Therefore, high-resolution imaging of subcellular structures is theoretically feasible with the TMAFM.

However, submersion in a liquid significantly changes the oscillatory behavior of the cantilevers. For example, the resonance frequencies in water are low than those in air by up to a factor of 5 for the most commonly used cantilevers; Quality factors in water are of order 1, compared with 10–100 in air [21]. The lowered and poorly defined resonance of cantilevers in aqueous solution makes high-resolution tapping mode imaging a technical challenge. While in principle tapping mode tends to minimize the tip-sample interaction force, contact mode in practice often provides better resolution for a given application such as when imaging relatively hard cells [22].

7.3 Acoustic vs. Magnetic Excitation

Currently, there are at least three drive mechanisms for tapping mode in fluid available to users on the commercial AFMs. Acoustic drive is among the first generation of tapping mode in fluid. In the scanning sample AFM design, a very small and fixed ac voltage is modulated into the large and slow varying dc voltage that controls the z piezo to move the sample up and down. Such modulation causes the sample oscillating at the ac driving frequency without affecting the imaging functionality [15]. Because such driving frequency is usually within the acoustic region and the cantilever oscillation is stimulated by the acoustic wave in the fluid, it is also called acoustic drive. Obviously, the oscillation is vulnerable to the

environment noise. This form of acoustically excited tapping mode has been shown to generate unwanted mechanical excitation of the detection system, rendering it less sensitive to the approach of the sample [105]. Furthermore, indirect forcing causes spurious resonances due to acoustic modes of the fluid cell [21]. A frequency sweep yields numerous peaks in the RMS (root mean square) cantilever amplitude in the general range of the desired cantilever resonance. This makes selection of the cantilever's natural frequency difficult [106]. The oscillating amplitude driven by the acoustic wave may vary 20% under normal condition from our observation. That means a large tapping force needs to be applied during imaging in order to suppress the oscillation large enough to maintain the stability of the system. Sometimes, this large tapping force will cause large cell deformation and obscure the image and even damage the cells.

The magnetic actuated drive is developed such that a electromagnet creates a magnetic field to drive a specialized probe coated with a magnetic film on the back side of the cantilever [107, 105]. Using the magnetic actuated drive mechanism, the resonant frequency of the cantilever is somewhat easier to be identified, as the resonant frequency oscillation of the cantilever is mainly excited. An unmagnetized cantilever has also been oscillated by applying an ac current to custom traces on the cantilever in the presence of a permanent magnet [106]. Revendo and Proksch constructed a fluid cell capable of imaging the same sample area using both acoustical excitation with a piezotube and magnetic excitation with a built in magnetic drive [108]. While the piezotube-driven tuning curve exhibited a complicated acoustic spectrum, the magnetic method produced a cleaner resonance response. The two techniques were shown to produce images with similar resolution. However, acoustic modulation resulted in sonication of molecular samples, causing sample instability and motion. The drawbacks of magnetic imaging were higher complexity and cost,

contamination of samples by magnetic metal ions, and heating of the fluid cell by the electromagnet.

7.4 Direct Drive

Recently, a direct drive liquid tip holder has been developed (Veec. Inc) such that a sealed piezo directly stimulates the probe as the traditional tapping mode tip holder does in the air. Using this driving mechanism, a large drive voltage is necessary to overcome the damping effect from the sealing layer and the liquid. As shown in Figure 7.1, a drive voltage of 50mV is enough to oscillate the cantilever at its resonance frequency of 75.7kHz with amplitude of 1V, while a drive voltage of more than 5V can only oscillate the cantilever at its resonance frequency of 10.6kHz with amplitude less than 0.5V. The quality factor dramatically changes from 105 in the air to 8 in the liquid. In our experiments, the oscillation generated by the direct drive is much stable and robust to disturbance. An amplitude of 0.4V or less is routinely used in our experiments without affecting the system stability.

7.5 Imaging Neurons by Tapping Mode

Neurons with their remarkable electrical activities attract our attention. It would the best candidate for AFM study since AFM has the potential to expand its functionality form imaging to sensing. Even with the poor practical results from the tapping mode AFM, its potential benefits aforementioned motivate us to face the challenges with hope to break through the barriers.

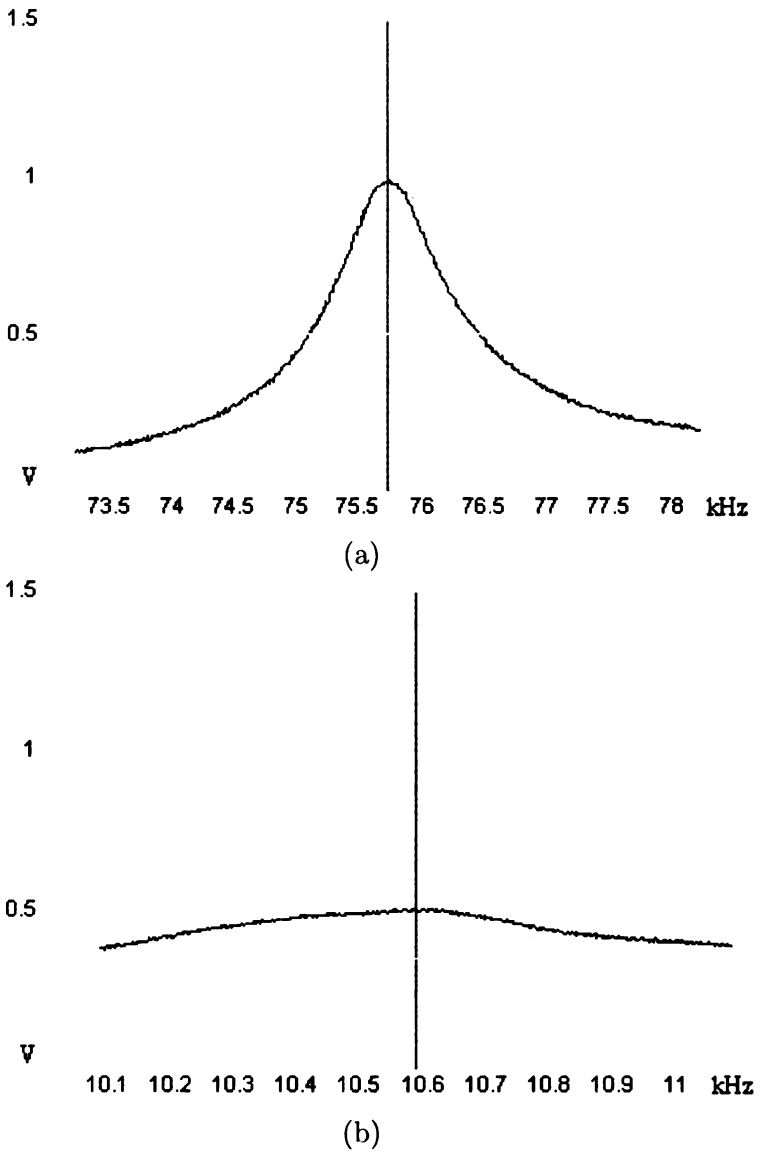

Figure 7.1. (a) The resonance frequency spectrum in both air with direct driving voltage at 50mV and quality factor close to 105. (b) The resonance frequency spectrum in both air with direct driving voltage at 5V and quality factor less than 8.

7.5.1 Cell Preparation

The living cell samples are sensory neural cells cultured on the glass coverslips in diameter of 15mm. The cells are originated in the dorsal root ganglia (DRG) tissue of male Wistar rats (body weight 125-200g). The cell culturing is a standard process

(Prepared by Dr. Wang's lab in the Department of Medicine, Michigan State University). Here is the detailed protocol. The DRGs from the cervical, thoracic, lumbar and sacral levels were removed aseptically and collected in F12 medium (Gibco/BRL). The trimmed DRGs were digested in 0.25% collagenase (Boerhinger Mannheim) in F12 medium at 37°C for 90 minutes. Following a 15-minutes incubation in PBS containing 0.25% trypsin (Gibco/BRL), the tissues were triturated with a pipette in F12 medium containing DNAse (Sigma, 80μg/ml), trypsin inhibitor (Sigma, 100μg/ml) and 10% heat-inactivated horse serum (Hyclone). Cells were then seeded in a 12-well culture plate with polyornithine coated glass coverslides inside. The purpose of polyornithine coating is to increase the adhesion between cells and the glass coveslip in order to immobilize on the glass surface. The cells were cultured in a humid incubator at 37°C with 5% CO_2 and 95% air. The cells are ready for AFM scanning after 7-10 days of culture.

7.5.2 Cell Imaging

The glass cover slip with monolayer DRG cells grown on the surface was put into a petri dish which contains F12 medium. Single cells were located using the optical microscope, and then were moved underneath the cantilever tip as shown in Figure 7.2 by adjusting the AFM stage. The image of the living cells was obtained using tapping mode AFM as shown in Figure 7.3. An image with higher magnification was obtained by zooming in the top of the cell membrane around the nucleus as shown in Figure 7.4.

7.6 Single Cell Surgery

Because AFM can operate in liquid condition, the development of the nano-robotic system engenders a powerful tool for cellar study. Single cell surgery becomes

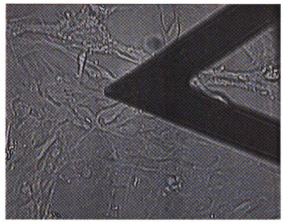

Figure 7.2. Low-magnification of the living cell using optical microscope: The AFM tip is adjusted to the top of the cell surface

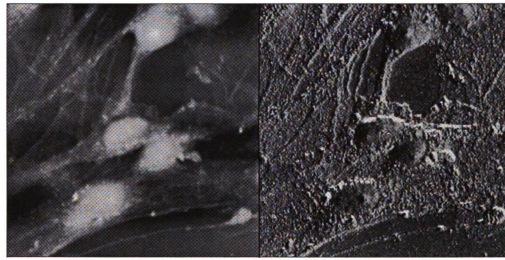

Figure 7.3. Imaging of the living cell using TMAFM with scanning range of 90μm: the left is the height image, and the right is the phase image

possible using the AFM based nano-robotic system. Because AFM probes are very sharp, some of them with high aspect ratio can be used as a scalpel to operate on individual cells when the cells are still alive. After cell imaging, manipulation can be performed under the assistance of the augmented reality. The tip can be injected into the cell or cut the cell membrane at certain locations. The two circles in Figure 7.5 indicate the cuts to a neuron's axon and another neuron's dendrite. The surgery operation is performed in the culture medium.

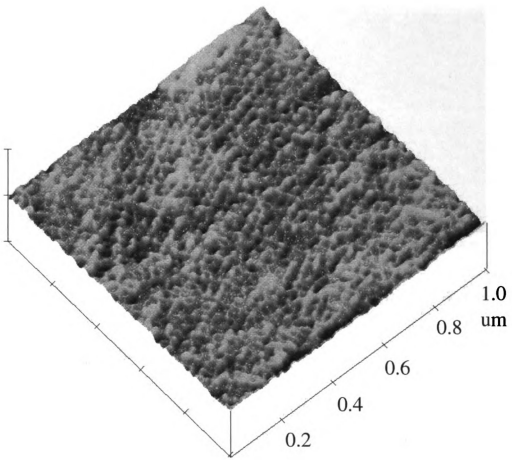

Figure 7.4. 3-D view of high-magnification imaging of the living cell using TMAFM with scanning range of $1\mu m$

Although an identical real-time visual feedback is not applicable at current stage, the rough estimation and the precise display of the tip location usually provide enough assistance to accomplish the operation. In the future, it is possible to achieve an authentic real-time visual feedback if the cell deformation can be accurately modelled.

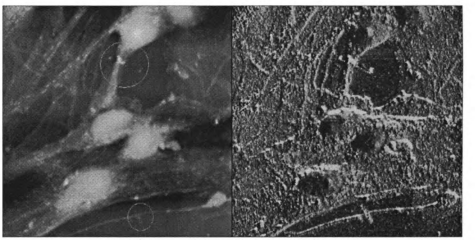

Figure 7.5. The final result of the cutting operation obtained from AFM image with scanning range of 90μm: Left, height image; Right, phase image.

7.7 Discussions

Although the TMAFM has significantly improved the resolution, it is still not possible to achieve molecular resolution when imaging the living cells. Therefore, finding an innovative way to fix the cell is very necessary. Although barriers exist, they should be overcome in the very near future given the rapid advancement of nanotechnology. Once we have reached such a breakthrough, further studies of membrane receptor functionalities including trafficking, signaling, and cross-talk would be possible. The issue will be discussed further in the next chapter.

The success of single cell surgery proved in this chapter will have a significant impact on cellular research. For example, by removing some over expressed receptors on membrane surface, some diseased cells can be cured in vitro. Given that many diseases have their roots at the molecular scale and are best understood as a malfunctioning biological nanomachines, the prospects of these unique techniques in basic biomedical research or in clinical practice are only limited by our imagination.

7.8 Summary

In this chapter, the current techniques for imaging living cells by AFM have been reviewed. The challenges and difficulties are also discussed. An example of imaging neurons in living condition is presented.

CHAPTER 8

Sensing Membrane Proteins Using Functionalized Probe

8.1 Introduction

Although membrane proteins are the main drug targets, the study of cell membrane proteins *in situ* on molecular level is difficult due to the current technical limitations. The recent development of atomic force microscopy (AFM) opens a new avenue to study the functionalities of cell membrane proteins *in situ*. AFM can operate in several environments including air, vacuum, and liquid. Most importantly, it can study the cells when they are still alive. Although recent progress has made it possible to observe the topographical image of membrane proteins in a well prepared flat surface like mica, observation of these proteins in their original location, the membrane surface, has been proven very difficult due to the softness of the membrane and the interference of the surface feature.

In this chapter, the techniques for characterizing specific single receptor using a functionalized AFM tip are discussed. The location and distribution of AT1 receptor

has been recognized by a functionalized AFM probe through a lift-up scan method. In order to increase the interaction force between tip and receptors, the AFM tip has been functionalized with antibody. A terminal thiol group is first attached to a spacer, Polyethyleneglycol (PEG), and this thiol group can then bind to a gold coated silicon nitride tip. An amine group at the other end of the PEG molecule attaches antibodies via a covalent bond. Because receptors are so small, it is hard to recognize them directly on the cell membrane surface only from the topographical information. When scanning the cell membrane surface using a tip functionalized with antibody, the tip-sample interaction force will increase when the tip approaches the receptor, thus a significant change of the phase shift will be observed. However, the topographical information is also convoluted into the phase contrast image due to the limitation of system bandwidth. By removing the topographic information of cell surface through a lift-up scanning technique, the location and distribution of a specific receptor can be easily recognized from the lift-up phase image. An example of investigation of the angiotensin II type 1 receptor by AFM with functionalized tip is introduced in this chapter.

8.2 Surface Modification

By immobilizing samples on a very flat surface such as mica, individual bio-molecules can be observed by AFM. For example, the major intrinsic proteins have been immobilized on a freshly cleaved mica surface by incubating with carboxypeptidase at room temperature overnight [23]. The mica surface was silanized in a solution of 2% 3-aminopropy-trithoxysilane in toluene for 2 hours [24] or by exposing it to the vapor of 3-aminopropy-trithoxysilane for several minutes [25]. The tip functionalization process discussed in next section is also practicable for surface modification.

8.3 Tip Functionalization

Functionalization of AFM tips by chemically and biologically coating the tip with molecules, e.g. biotin-avidin pairs [26, 27] and antigen-antibody pairs [28, 24], has opened a new research area for studying interactions of molecules on molecular level. Chemical coating of probes is mainly done by silanization or by functionalization with thiols and is often the first step before biological functionalization. Many protocols have been used for attaching proteins to an AFM tip. There are two main ways to functionalize the AFM tip with antibodies. One is to directly coat the antibody on a silanized tip, and the other is to tether the antibody on a tip via a linker (or spacer). The direct coating method is simple and results in high lateral resolution. The tethering method involves much more complicated steps, but it gives better antigen recognition given that the interaction between antibody and antigen is highly specific, which involves a high degree of spatial and orientational specificity. The drawback of the tethering method is that the lateral resolution is low. The detailed steps of these two methods are discussed below.

8.3.1 Direct Coating Methods

Several direct coating methods are available, and most of them are based on silanizing a solid surface. Here is an example that has been used by us for directly attaching antibodies to an AFM tip. The silicon nitride tips were treated with 10% nitric acid solution which was left in a silicone bath for 20 minutes at 80 °C. This causes the formation of surface hydroxyl groups on the SiN tips. The tips were then thoroughly rinsed with distilled water, placed into 2% 3-aminopropylmethyl diethoxysilane (APrMDEOS) solution in toluene, and kept in a desiccator purged with argon gas for 5 hours. This treatment provides reactive primary amine groups on the nitride surface. The tips were washed thoroughly with phosphate buffer saline (PBS)

and placed into a solution of 2 g/ml Antibody IgG for 10 minutes. The antibody-conjugated tips were then washed thoroughly with PBS and distilled water to remove loosely attached antibodies. These tips should be used immediately before being dried.

8.3.2 Tethering Methods

Functionalization of the AFM tip with antibody using the tethering method involves much more steps than the direct coating method. It usually needs a spacer to covalently bind the protein in order to orient the protein to expose specific site(s) of the protein. Polyethyleneglycol (PEG) is a common spacer to be used. A terminal thiol group can be first attached to PEG, which then will be attached to a gold-coated silicon nitride tip. An amine group at the other end of the PEG molecule attaches proteins (antibodies for example) via a covalent bond [28].

The tip functionalization used in this study is the tethering method, which needs a flexible spacer. The method was chosen because a high binding rate is expected. The tethering method needs much more complicated protocol, but it results in better chance of antigen recognition because the interaction between the antibody and the antigen is highly specific and processes a high degree of spatial and orientation specificity. It gives the antibodies more freedom to bind the antigen. The spacer covalently binding the proteins can orient the proteins to expose specific site(s) of the receptors . A terminal thiol group can be first attached to PEG and this thiol group can bind to a gold-coated silicon nitride tip. An amine group at the other end of the PEG molecule attaches proteins (antibodies for example) via a covalent bond [28]. Biological coating has been mostly used for measuring the binding force between a receptor and a ligand [109, 110] including antigen-antibody-pairs [24] as well as mapping the distribution of binding partners on samples [111, 31, 35]. The

similar process of functionalization can be found in [36].

8.4 Probing Receptor-Ligand and Antibody-Antigen Interactions

AFM is capable of measuring forces on piconewton scale by nature, a property that has been exploited to examine receptor-ligand interactions. An emerging body of literature employing AFM to measure and characterize these interactions is available. A wide range of receptor-ligand pairs have been studied by AFM with a functionalized tip. The first study focuses on very high affinity interactions, such as interactions between biotin and avidin [26, 27]. In the study, a silicon nitride AFM tip was functionalized by avidin through the following steps: The tip was first cleaned and silanized and then incubated in biotinylated bovine serum albumin for 24 hours. After fixed in 1% glutaradehyde solution for 30 seconds, the avidin was added to bind to the biotin, and the AFM tip was functionalized with avidin. By immobilizing the biotin on an agarose bead, the rupture force between the biotin from the bead and the avidin from the tip was measured using the force modulation mode. When the tip was retracted, it detached from the surface in a series of discrete jumps with each corresponding to breakage of one or more biotin-avidin bindings. The total jump-off force was expected to consist of an integral multiple of single rupture force. Therefore, by constructing a histogram of rupture forces, the single pair unbinding fore was measured. The rupture force has been calibrated from 160 pN for avidin-biotin pair to 260 pN for streptavidin-biotin pair [29]. As understanding and interpretation of these initial studies on the measurements of rupture forces by AFM have improved, more investigators reproduced and extended the avidin-biotin findings by determining the bond strength of other examples of receptor-ligand pairs. These studies of AFM binding have been given an extensive

overview by Willemensen et al [30].

Antibody-antigen interaction is of importance in the immune system, which may vary considerably in affinity. Hinterdorfer and co-workers were the first to determine the interaction between individual antibodies and antigens [28]. In their work, they used flexible linkers to couple either the antigen or the antibody to the tip, which provided the antibody and antigen enough freedom to overcome problems of mis-orientation due to the high degree of spatial and orientational specificity between antibody and antigen. By coupling the antigens and antibodies to the tip and surface, respectively, via polyethylene glycol (PEG) spacer (8nm in length), the binding probability has been significantly improved due to the large mobility provided by the long spacer molecules. When a tip is functionalized at very low antibody density such that only one single antibody at the tip apex has chance to access an antigen on the surface, single molecular antibody-antibody complex could be examined.

8.5 Single Molecules Recognition

Although high-resolution images can provide some detailed conformal information of molecules, they may not provide information related to any specific protein. Because the interaction between ligands and receptors is highly specific and possesses a high degree of spatial and orientational specificity, the technique to functionalize an AFM tip with specific molecules make investigation of single specific molecule possible. Rupture forces representing biomolecular specific interactions can also be exploited as a contrast parameter to create images in which the individual biomolecules can be recognized. It has been proven that single receptors can be recognized by an AFM tip functionalized with antibody through a force mapping technique [31, 30] on very flat surfaces such as mica. In their study, the functionalized tip was raster-scanned

over the surface while a force-distance curve was generated for every pixel. From the force distance curve, the surface parameters such as stiffness and adhesion force were extracted either by online process in real time or by off-line analysis. The individual receptors were recognized through these so called adhesion mode AFM. However, the adhesion AFM image obtained by this method has low lateral resolution and the work is extremely time-consuming.

Another way to recognize specific proteins (or receptors) is to use the tapping-mode phase imaging. It can differentiate between areas with different properties regardless of their topographical nature [32, 33]. The phase angle is defined as the phase lag of the cantilever oscillation relative to the signal sent to the piezo driving the cantilever. Theoretical simulations and experiments of the cantilever dynamics in air have shown that phase contrast arises from differences in the energy dissipation between the tip and the sample. The phase shift is related analytically to the energy dissipated in the tip sample interaction by following equation [32, 33]

$$\sin\psi = \left(\frac{\omega}{\omega_0}\frac{A}{A_0}\right) + \frac{QE_D}{\pi k A A_0}$$

where ψ is the phase angle; ω/ω_0 is the working frequency/resonance frequency; A/A_0 is the set-point amplitude/free amplitude; Q is the quality factor; E_D is the energy dissipation; and k is the cantilever spring constant. The phase shift due to the tip-sample interaction, which involves energy dissipation, is the displacement of the non-contact solution to higher phase shifts and the intermittent contact solution to lower phase shift values. The more dissipative features will appear lighter in the non-contact regime, whereas they will appear darker in the intermittent-contact regime [34].

When scanning the proteins immobilized on mica surface using a tip functional-

ized with its antibody, the tip-sample interaction force will increase as the tip closing the receptors; thus a significant change of the phase shift will be generated. Since the topographical information is also convoluted into the phase contrast image but with low frequency, a band-pass filter can be used to remove the low frequency topographical information and the high frequency noise. After filtering the phase contrast image, only the receptors' image will be left on the surface. Individual surface receptor has been identified on mica surface using these techniques [35, 36].

8.6 *In Situ* Probing Membrane Proteins

Although individual proteins can be recognized efficiently through the tapping-mode phase imaging by a functionalized tip, biomolecules have to be extracted, purified, and attached to a flat and rigid surface. Detecting membrane proteins directly in native environments is a daunting challenge given that the cell membrane surface topographical information interferes with the antigen-antibody binding. The interference may "buries" the signal and make the recognition impossible. Fortunately, this problem can be solved by an interleaved lift-up scanning, recently developed, to remove the interference from topography. The details on lift-up scan are discussed in the Section 8.6.1. As an example for *in situ* probing membrane proteins using functionalized tips by atomic force microscopy, the the Angiotensin II type 1 (AT1) receptor, which expresses on the membrane of sensory neurons, is chosen as the study object in this research. Several key techniques are required in order to probe the receptors *in situ*. They are expounded in the following discussions, which include tip functionalization, cell fixation, as well as interleave lift-up scan.

8.6.1 Interleave Lift-up Scan

Because receptors are so small, it is hard to recognize them directly on the cell membrane surface only from the topographical information. Fortunately, the new technique, tapping-mode phase imaging, provides a promising solution. When scanning the cell membrane surface using a tip functionalized with antibody, the tip-sample interaction force will increase when the tip closes the receptor, thus a significant change of the phase shift will be generated. However, the topographical information is also convoluted to the phase contrast image due to the limitation of system bandwidth. Using a interleave lift-up scan method, this problem can be easily solved. As shown in Figure 8.1, the tip first scans the surface once and obtains the topographic information of the surface, and then in the next scan, the tip lifts up a few nanometer but scans the same line as in the previous scan. As long as the lift-up distance is smaller than the length of the PEG linker and larger enough to lift the tip from the surface, the receptor-antibody interaction will not be affected but the topographical interference caused by the surface can be totally removed during the second scan. The phase image captured from the second scan only contains the information of receptor-antibody interaction. By integrating the phase image from second scan with the topographical image captured from the first scan, the location of the receptor can be easily identified and labelled.

8.6.2 The Renin-Angiotensin System

The angiotensin II type 1 receptor (AT1) expressed in sensory neuronal cells is studied using the developed techniques. Before the experiments, the background of the AT1 receptor and its associated rennin-angiotensin system are introduced.

The renin-angiotensin system plays a major role in the regulation of blood pressure, vasopressin and pituitary hormone release, sodium appetite and perception of

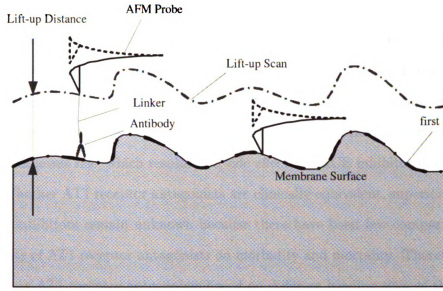

Figure 8.1. The AFM tip scans the first line and records the topographical information, and then the tip is lifted up and scans the same line but follows the topography obtained from the previous scan. In the lift-up scan, only the antigen-antibody interaction can be recorded in the phase image.

thirst [112, 113]. The cascade pathway of the renin-angiotensin system is illustrated in Figure 8.2. Renin, an enzyme, produced primarily by the juxtaglomerular cells of the kidney, converts the liver precursor angiotensinogen to an inactive substance, angiotensin I (AI). AI is in turn converted to the physiologically active peptide, angiotensin II (AII) by pulmonary angiotensin-converting-enzyme (ACE). AII is thought to involve in control of blood pressure, fluid volume, electrolyte balance, and cardiovascular functions by acting on the angiotensin type 8.2 (AT1) receptor [114]. As shown in Figure 8.2, the cascade pathway of the renin-angiotensin system can be blockaded at different steps. Different drugs have been or are in the process to be developed based on the blocking steps. For example, angiotensin converting enzyme (ACE) inhibitors or AT1 receptor antagonists have been developed as very effective anti-hypertensive drugs. Figure 8.2 also shows the major difference in the mode of action of AT1 receptor antagonists as opposed to ACE inhibitors. AT1 receptor an-

tagonists block all of the known actions of angiotensin II through acting on the AT1 receptor. In contrast, ACE inhibitors work at the up-stream of the renin-angiotensin cascade, inhibiting effects of ACE. ACE acts both on angiotensin I, converting the inactive angiotesin I to the active angiotensin II, and on bradykinin, inactivating this hormone. Since the inactivation of bradykinin is blocked by ACE inhibitors, bradykinin levels rise, which results in a side effect-the ACE inhibitor induced cough [115]. Whether AT1 receptor antagonists are clinically equivalent, superior or inferior to ACE inhibitors remain unknown because there have been few comparative trials of benefits of AT1 receptor antagonists on morbidity and mortality. Therefore, to develop more AT1 receptor antagonists based on different binding sites of the receptor and bring them to clinical trials may be beneficial in treating hypertensive patients more effectively.

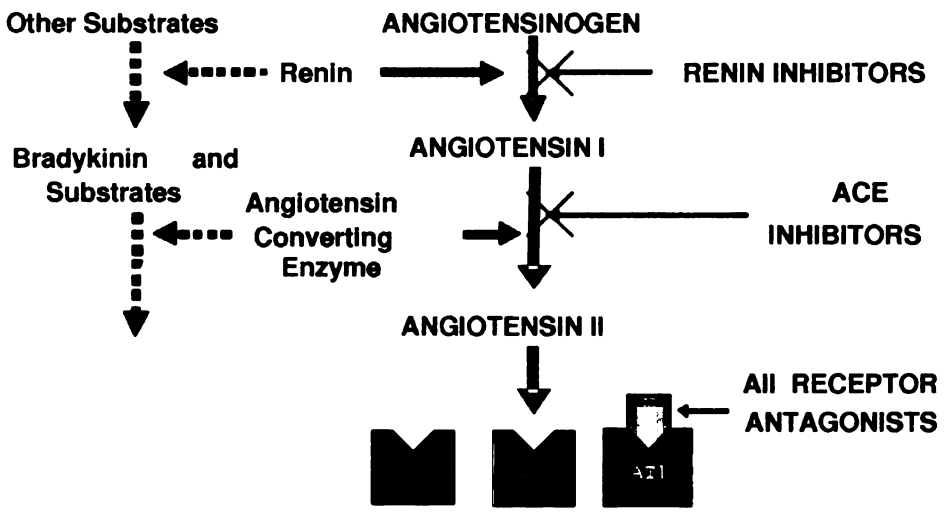

Figure 8.2. The renin-angiotesin system and theoretic biochemical and physiologic consequences of blocking the renin-angiotensin system at different steps in the pathway

8.6.3 Angiotensin II Type 1 Receptor and Its Antibody

Ang II is an important physiological effector of blood pressure and volume regulation through vasoconstriction, aldosterone release, sodium uptake and thirst stimulation. The synthesis of novel nonpeptide Ang II receptor antagonists revealed the existence of at least two Ang II receptor types, designated type 1 receptor (AT1) and type 2 receptor (AT2). Although Ang II interacts with two types of cell surface receptors, most of the major cardiovascular effects seem to be mediated through AT1 [116].

The amino acid sequences encoded by the open reading frame of AT1 cDNA and genomic DNA of all mammalian and rodent species consist of 359 amino acid residues [117]. Structural predictions suggest an extracellular NH2-terminus followed by seven helical transmembrane-spanning domains, which are connected by three extracellular and three intracellular loops, linked to the carboxyl-terminus as shown in Figure 8.3. The mechanisms of regulation, activation and signal transduction of the AT1 receptor have been studied extensively in the decade after its cloning. At present, little is known about the mechanisms regulating intracellular trafficking of the AT1 receptor. However, using confocal laser scanning microscopy, it was demonstrated that the complex of FITC-coupled Ang II and Flag epitope tagged-AT1 receptor was internalized into endosomes. After removal of Ang II, the AT1 receptor was recycled back to the plasma membrane, while Ang II was targeted to the lysosomal degradation pathway [118]. The studies using AFM with tip functionalized by AT1 antibody may provide detailed evidence of receptor intracellular trafficking.

AT1 antibody (Santa Cruz Biotechnology, Inc.) is an affinity purified rabbit polyclonal antibody raised against a peptide mapping near the amino terminus of the AT1 receptor of human origin (identical to corresponding rat sequence). It was chosen as the end effector of functionalization material because it targets against the amino

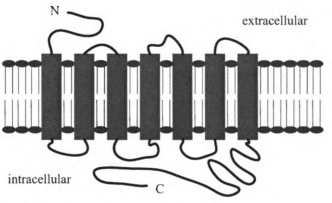

Figure 8.3. Predicted membrane topology and domain structure of the AT1 receptor. AT1 has seven complete transmembrane segments. The amino-terminal region is located outside the plasma membrane and the carboxyl-terminal region is located inside the plasma membrane

terminus of the AT1 receptor which is supposed to be outside the cell membrane.

8.6.4 Functionalization of AFM Probe with AT1 Antibody

The process is designed to functionalize the tip with AT1 antibody as shown in Figure 8.4, but the protocol can be easily extended to other functional agents. It can be divided into following steps:

1. Modify the AT1 antibody with N-Succinimidyl 3-(Acetylthio)propionate.
2. Modify AFM tips with APTES (aminopropyltriethoxysilane).
3. Tether the cross-linkers.
4. Link the SATP-Labeled antibody to tips.

The detailed protocol for functionalization process is provided in Appendix B. After functionalization, an immunohistochemical like method has been used to verify the success of the functionalization. By incubating the functionalized tip in PBS which contains anti-rabbit IgG (second antibody) labelled with CY3 dye for 1 hour, the AFM tip can be checked by confocal fluorescence microscope. A clean AFM tip without functionalization is used as a control. The fluorescence microscopy results are shown in Figure 8.5. It can be seen that the functionalized tip has significant

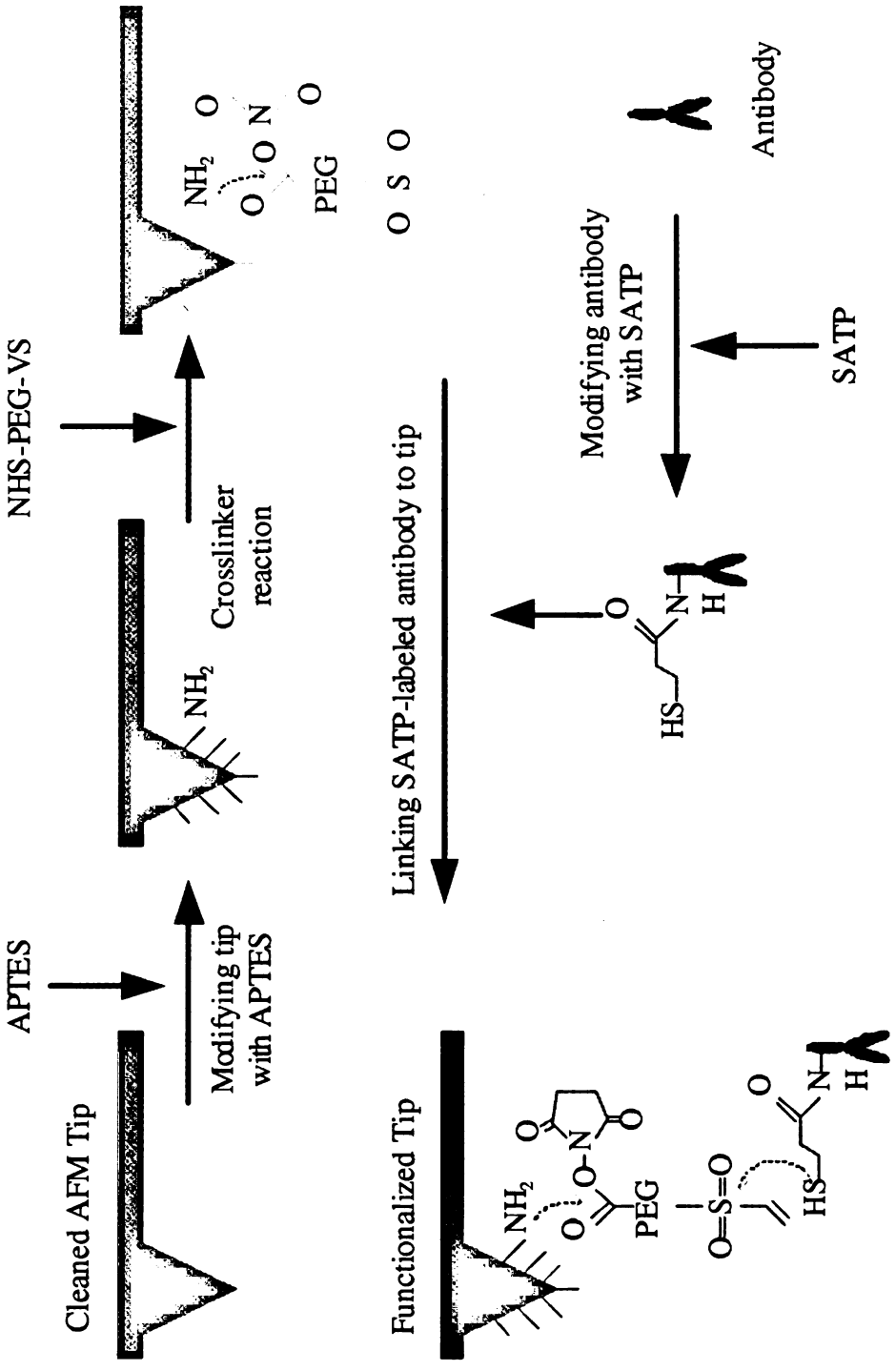

Figure 8.4. The process of functionalizating the tip with antibody via a linker

fluorescence signal but there is no fluorescence signal from the tip without function-alization.

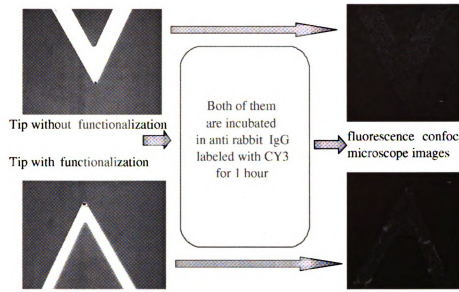

Figure 8.5. The immunohistochemical verification of the probe functionaization. The functionalized tip has significant fluorescence signal but there is no fluorescence signal for the tip without functionalization, which verifies the success of the tip functionalization.

8.6.5 Living Cell Sample Preparation

Given the purpose of this research is to study the functionality of the receptors, a native environment for the receptor has to be maintained during the study. In this study, living sensory neurons are chosen in which AT1 receptors are expressed [119, 120]. The living cell samples are prepared as in the previous chapter.

8.6.6 Single AT1 Receptor Recognition

In order to solve the problem caused by the softness of the cell membrane, the cells are chemically fixed in PFA (4% paraformaldehyde in 0.1M sodium phosphate buffer, pH 7.4) for 30 minutes, and then washed with PBS 3×5 minutes each. Using a lift-up scan method, most interference form topography can be removed. Because the topographical information has low frequency, a band-pass filter can further remove the low frequency topographical information and the high frequency

noise. After filtering the phase contrast image, only the receptors' image will be left on the surface. Figure 8.6 shows a phase contrast image of a neuron membrane obtained by lift-up scan with a functionalized tip. The image has been processed by a band-pass filter. The AT1 receptors are clearly indicated on the image. After adding enough fresh AT1 antibodies in the solution to block all the AT1 receptors on cells' membrane, an image of the same area was obtained by lift-up scan. Using the same band-pass filter to process the phase contrast image, no receptor can be identified on the surface as shown in Figure 8.7. These experimental results show that single bio-molecules such as receptors on the cell membrane surface can be recognized using the biologically functionalized tip.

It is a great breakthrough to identify single receptors *in situ* even though not under living condition. It proves the concept of single receptor recognition. With the rapid advancement of nanotechnology, the cell softness problem will be solved very soon. Once the stable images with high resolution are obtained from living cells, single receptor recognition in living condition would become a trivial problem.

8.7 Discussions

In conclusion, the technique using a functionalized tip to measure the interaction force between ligands and receptors by AFM has been discussed for nearly a decade. Single-molecule recognition from processed samples using a functionalized tip has been possible by recent research study. We also have achieved recognizing single receptors directly from the fixed membrane surface without further sample preparation. Techniques for detecting and characterizing specific individual molecules from a living cell are still under development.

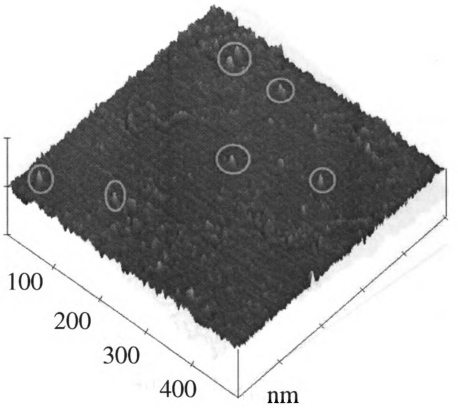

Figure 8.6. 3-D view of a phase contrast imaging of the fixed cell membrane surface using Tapping Mode AFM with scanning range of 500nm. The image is obtained using a functionalized tip with AT1 antibody by lift up scan and then passing through a band-pass filter. The AT1 receptors are clearly identified as shown inside the circles.

As mentioned in Chapter 7, although several approaches have been investigated to "harden" the cell such as low temperature and small force scanning, all these methods seldom work in practice. Chemically fixing the cells is definitely not a good solution since the cells are dead and any real-time life activities are frozen. It may provide better resolution image that may be important for cellular research but the results are not far-reaching considering the TEM provides better resolution and more details underneath the cell membrane. Therefore, finding an innovative way to "fix" the cells without killing them is not only imperative but also crucial. Inspired by the chemical fixation, a heuristic method is proposed to tackle this problem by mechanical fixation.

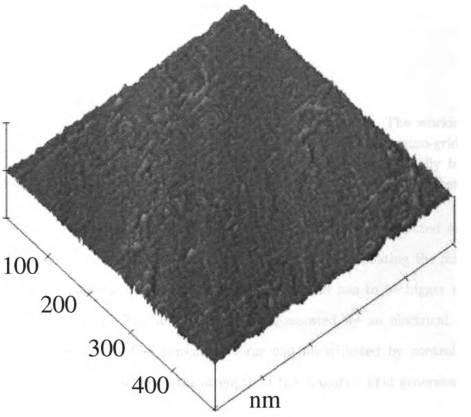

Figure 8.7. 3-D view of a phase contrast imaging of the fixed cell membrane surface using Tapping Mode AFM with scanning range of 500nm. The image is obtained after adding enough AT1 antibodies to block all the AT1 receptors and then passing through the same band-pass filter as that used in Figure 8.6. However, no receptors can be identified in the image.

The working principle of the proposed micro-grid is shown in Figure 8.8. The membrane of the micro-grid serves as a fixture. The micro-grid is supposed to constrain the membrane and to prevent it from deformation caused by the tapping force from the AFM tip. The AFM tip touches the cell membrane through the small openings on the micro-grid provided that the openings are large enough and the thickness is thin enough to allow the AFM tip probing the cell surface through the hole. The micro-grid membrane presses the cells on the substrate by applying

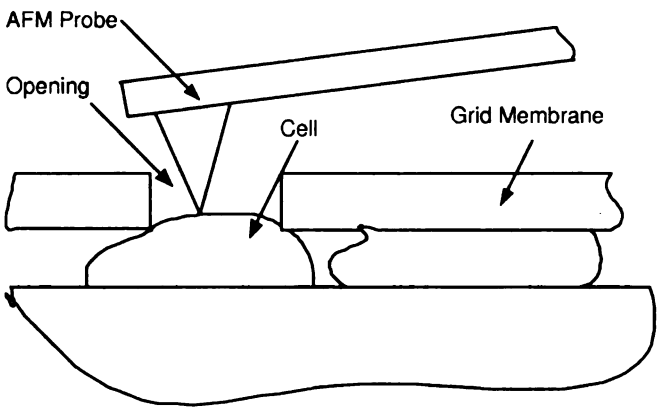

Figure 8.8. The working principle of the micro-grid to fix the cell mechanically by pressing the cell on the substrate

a magnetic field underneath the micro-grid. The pressure is generated either by deposited magnetic beads on top-side of the micro-grid or by coating the micro-grid with a layer of magnetic materials. Obviously, the bead has to be bigger than the hole in the micro-grid. The magnetic field is generated by an electrical solenoid underneath the sample. The constraint force can be adjusted by controlling the number of the magnetic beads or the strength of the magnetic field generated by the electrical solenoid.

The proposed micro-grid is expected to increase the "hardness" of living cells by mechanical constrains. The idea is to mechanically immobilize the surface of living cells by a micro-grid, a polymer membrane with lots of opening on it. The polymer material is chosen because of its bio-compatibility. The grid design is shown in Figure 8.9. The opening size varies from 2μm to 10μm depending on the cell size. The grid thickness varies from 100nm to 2μm, which is limited by the tip height.

The Micro-grid fabrication process starts with a blank double-sided polished GaAs wafer. A layer of 500nm Polyimide PI-2556 from HD MicroSystems, is deposited on top by spinning process. It is baked for 60secs at 150°C (Hotplate). This layer is then patterned by AZ5214E photoresist. The photoresist and polyimide layers are etched together by AZ300 developer. Then, full curing of the polyimide is done

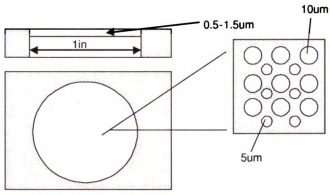

Figure 8.9. The design of polymer micro-grid with both 5μm to 10μm openings

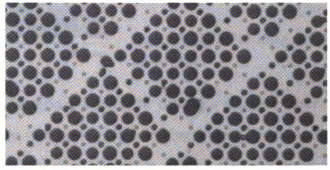

Figure 8.10. Optical image of the micro-grid fabricated with 5μm and 10μm opening

under vacuum at 200°C. After that, the whole substrate is covered with photoresist and holes are patterned at the backside of the wafer. H_3PO_4:H_2O_2:H_2O (1:13:12 in volume) is used to back etch GaAs substrate. As a result, a suspended polyimide membrane can be made. Figure 8.10 shows the optical image of micro-grid fabricated in our laboratory with thickness of 500nm containing 5μm and 10μm holes on it.

The primary experiments show that the micro-beads are moving to the stronger magnetic field while the desired area does not attract enough beads. Fortunately, several beads trapped inside the holes do improve the image quality. Figure 8.11 shows the AFM image of the micro-grid when several beads trapped inside holes. Even though the constraint force is not strong enough, the experiment at least proves that the constraint from magnetic force might be viable if a magnetic layer can be coated on the micro-grid.

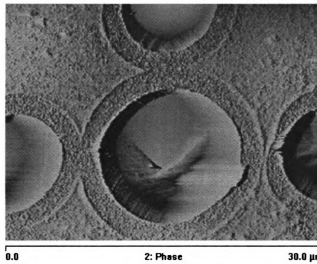

Figure 8.11. AFM image of the micro-grid

Further improvement of the micro-grid is possible by coating a magnetic layer on the micro-grid. The routine process of magnetic layer coating is done by sputtering. A layer of cobalt or iron can be deposited on either side of the micro-grid by sputtering. Another alternative method is to coat a layer of magnetic materials chemically. For example, a magnetic film can be made from diazoresin and Fe_3O_4 nano-particles [121, 122]. The process is a layer-by-layer (LBL) self-assembly.

The cell softness is the major impediment at current stage. Although the TMAFM has significantly improved the resolution, it is still not possible to achieve molecular resolution when imaging the living cells. As long as this problem has been solved, it would become trivial to probe single membrane proteins *in situ* on living cells. The preliminary experiments have proven the effectiveness of the micro-grid for "fixing" without killing. Further comprehensive study using the micro-grid is expected in the future research. Once we reach such a breakthrough, further studies on membrane receptor functionalities including trafficking, signaling, and cross-talk would be possible.

8.8 Summary

In this chapter, the current techniques for characterizing specific single receptor using a functionalized AFM tip is first reviewed thoroughly. When scanning the cell membrane surface using a tip functionalized with antibody, the tip-sample interaction force will increase; thus a significant change of the phase shift will be generated. In order to probe the membrane *in situ*, the necessary techniques are discussed from interleave lift-up, cell fixation, and tip fictionalization. By removing the topographic information of cell surface through a lift-up scanning technique, the location and distribution of a specific receptor can be easily recognized from the lift-up phase image. AT1 receptor has been successfully recognized *in situ* by the redeveloped techniques.

CHAPTER 9

Conclusions and Perspectives

9.1 Conclusions

Manipulation of nano-entities using AFM has been extensively investigated for many years. Most schemes are circumscribed by their impotence of real-time visual feedback during manipulation. The AFM based nano-robotic system developed in this research has solved this problem. All the experimental results show the effectiveness and efficiency of the developed system. The ability of the nano-robotic system to manipulate nano-particles, nano-wires, nanotubes, and DNA molecules makes it an effective machine to fabricate nano-devices and nanosensors. Combining its capability to distinguish specific bio-molecules with its ability to modify the cell by manipulation, the AFM based nano-robotic system will become a powerful tool in cellular research.

Although the research is based on a commercial AFM system (Bioscope AFM from Veeco Metrology, Inc.), all the techniques developed in this dissertation are independent of the specific equipment. They are ready to be grafted onto other AFM systems without any major modifications.

Both the theoretical and experimental studies in this research are in the vanguard of AFM based research. The potential application of this system is far-reaching to nanotechnology research. Further applications of this research are beyond our imagination considering the rapid development of nanotechnology.

9.2 Future Work

Because atomic force microscope is such a novel tool, its applications are undergoing rapid expansion. Due to its less demand on working condition, AFM also becomes a favorable technique to combine with other tools such as fluorescence microscope. The slow scanning speed that prevents its application from real-time imaging is going to be overcome by fast scan AFM soon. AFM with up to 6 probes that are controlled independently is also commercially available now. Considering the rapid development of AFM technology, there is capacious space to further improve and perfect the system.

The immediate perspectives from this research lie in several aspects: active probe for manipulation, automated manipulation, real-time visual feedback for single cell surgery, further improvement of resolution on soft samples in liquid, and so on. Some of these perspectives have been discussed with preliminary results. For example, automated manipulation has been discussed in Section 4.4.2 and the preliminary results are published in [67]; active probe control for manipulation has been discussed in Section 3.7, and the comprehensive results are available from [54]. In the following discussions, several perspectives from this research will be further addressed.

The current augmented reality interface for AFM based nano-robotic system

works better for rigid nano-objects. There is a pressing need to extend the manipulation capability of the system to flexible nano-objects. Although the purely flexible DNA has been modelled in this research, a lot of other useful nano materials such as single walled carbon nanotubes are difficult to model. They are rigid in a short range but behave flexibly in a wide range. In order to predict the deformation and motion behavior of these semi-flexible nano-objects, suitable models to describe their behavior under manipulation are indispensable.

The local scan developed in this research is very effective for rigid nano-objects such as nano-particles and nano-rods. However, many nano-objects are flexible (DNA molecules), semi-flexible (single walled carbon nanotubes), or totally soft (cell membranes). Develop local scan strategies for these nano-objects is very imperative for the system, especially when using the nano-robotic system to manipulate DNA molecules (refer to Chapter 6), to fabricate CNT based nano-devices (refer to Section 4.4.3), and to perform single cell surgery (refer to Chapter 7).

Although the result in Chapter 6 shows that DNA is conductive, the conductivity may be caused by the water molecules in air. Therefore, a controlled condition is necessary to further study the electrical property of DNA molecules. Although a vacuum condition would be an ideal solution, it is difficult and expensive to set up a vacuum measurement chamber. An alternative solution would be a sealed dessicator purged with inertia gas such as argon. Because the DNA molecules are so small (less than 3nm in diameter), a fine electrode with thickness less than 10nm is necessary in order to observe the DNA molecules from the AFM image. Or else, if the electrodes are too high, the contrast may be not enough to make the DNA molecules visible. Practically, such kind of electrodes are very difficult to fabricate. A possible solution is that thick electrodes can be fabricated first,

and followed by depositing a layer of polymer or silicon nitride. The surface can be polished to expose the electrodes. The electrodes fabricated by such way possess very flat surface and may result in a high contrast of DNA in the AFM image.

The cell softness is still the major impediment for high resolution of living cells at current stage. Although a micro-grid has been proposed in Section 8.7 to tackle this problem, its effectiveness is only proved preliminarily. Further experiments need to be conducted in order to completely prove its effectiveness. Efforts are also needed to search other types of fixing without killing methods, especially in a biological way. The technique that we have developed to *in situ* recognize the individual receptors opens a new way to study the functionality of individual receptors. Further study of the trafficking behavior of the receptors and cross talk among them is possible if the cell can be fixed without killing.

E-beam nanolithography is an effective way in making nano patterns, but its position accuracy and efficiency is low. An efficient AFM based nanolithography can be achieved with high position accuracy and at low cost through the tunnelling nanolithography. By combining the nano-robotic techniques developed in this research with the automated assembly techniques as described in [67], AFM based nanolithography could be more efficient and accurate.

Considering the rapid development of the AFM technology, further improvement of the AFM based nano-robotic techniques can be directed to at least three directions in the long term: multi-probe manipulation, authentic real-time visual feedback, and materials delivery by AFM probe.

A multi-probe AFM has been developed by MultiProbe Inc. The system has

up to six scanner heads that are controlled independently. The system is mainly designed for characterization of semiconductor devices. The probes used in this system are different from the most commercially available AFM tips. They are specially designed such that they are close enough to scan the same area at the same time. This kind of design brings the expectation that the probes can be controlled cooperatively to pick up nano-objects and deliver them into their desired locations. This hand-finger type manipulation would be a breakthrough for AFM based manipulation since all the previous AFM manipulation schemes are purely based on pushing objects instead of picking them up and releasing. The pushing strategy often encounters unavoidable obstacles, but the problem can be easily solved by the picking and releasing strategy because theoretically there are no obstacles in this situation. It would be an interesting direction for the research in the AFM based manipulation and a promising way to extend the applications of the AFM based robotic technology.

The scanning speed of commercially available AFMs is relatively slow. It usually takes several minutes to obtain an image. The slow scan of AFM makes it difficult for real-time monitoring on nano scale. Although there are several techniques available to increase the scanning speed such as using active probe or small cantilever, they are still not able to satisfy the real-time requirement. In order to achieve fast scan at real-time frame rate, the AFM architecture has to be redesigned and the advanced control technology has to be adopted. The current local scan technique developed in this research uses the same probe for both scanning and manipulation, and therefore, intermittent switching between scanning and manipulation makes the visual feedback too much depend on the behavior models of the nano-objects which are often unreliable especially for those semi-flexible materials. Combining the multi-probe technology with the fast scan technology, the truly real-time visual feedback becomes possible. For example, when one probe is performing

the manipulation, other probes can perform the local scan with a fast speed. Therefore, the image is updated based on real scanning information instead of prediction by models. Obviously, the visual feedback updated in this way is more reliable.

Not only can the AFM probe be used for scanning and manipulation, it is also possible to use it as a delivery tool to transport nano-materials during nano-fabrication and deliver drugs during biomedical study by AFM. Special designs are needed for the AFM probe that can deliver nano-materials. Micro-channels have to go across the cantilever without significantly affecting the cantilever mechanical properties during scanning. Controlling the flow inside these channel is also a challenge task considering the strong surface tension. Micro fluidics has to be involved in the research.

APPENDIX A

Protocol for Hydrophobization of SiO2 Surface

1. UV light for 15m to remove the organic materials on the sample surface
2. Sample surfaces are soaked in concentrated NH4OH for 1 h and wash 5 times by ultrasonication in distilled DI water (18MΩ*cm)
3. The surfaces are then dried for 1h at 140°C and place directly in methanol to keep the surface free from water vapor and other unwanted adsorbates.
4. The surfaces are then silanized by immersion in a 5mM n-octadecyltrimethoxysilane solution in heptane for 24h
5. The silanized surfaces are washed 3 times with heptane to remove unreacted silane materials.
6. The treated surfaces are then heated for 1h at 70°C.
7. After the coating, the treated surface are rinsed with acetone to remove any unreacted silane and then stored in methanol until used.

APPENDIX B

Protocol for Modifying AFM Tips with Antibodies

1. Modifying Antibody with N-Succinimidyl 3-(Acetylthio)propionate.

   (1) Wash PD-10 column with 30 ml of buffer A (100 mM NaCl/50 mM-NaH2PO4/1 mM EDTA, pH 7.5).

   (2) Load 200 μl (1 ml/ml) of antibody in 300 μl of buffer A onto PD-10 column.

   (3) Pass 500 μl of buffer A through the column nine times.

   (4) Collect fractions seven and eight and pool them.

   (5) Add a 10-fold molar excess of N-succinimidyl 3-(acetylthio)propionate (SATP)/DMSO to antibody solution for 30-60 min under argon.

   (6) Rinse two PD-10 columns with 30 ml of buffer A.

   (7) Add 500 μl of antibody solution into each PD-10 column, and then pass 9×500 μl of buffer A through the columns, collecting fractions seven and eight and storing them in 100 μl aliquots at -70 °C.

2. Modifying Tips with APTES.

   (1) UV-clean MAC levers for 15 min.

   (2) Purge a glass desiccator with argon for 2 min, and place 30 μl of aminopropy-

ltriethoxysilane (APTES) (99%; Sigma-Aldrich) into it in a small container. Place 10 μl of N,N-diisopropylethylamine (99%, distilled; Sigma-Aldrich) into another small container in the desiccator and purge with argon for a further 2 min. Place cleaned probes into the desiccator, purge for another 3 min, and seal for 0.5 to 2 h. Remove reagents, purge with clean argon, and keep probes stored in this environment.

3. Crosslinker Reaction.

   (1) Mix crosslinker and 5 μl of triethylamine in 1 ml of CHCl3.

   (2) Place NH2-modified tips into this solution for 2-3 h.

   (3) Wash tips with CHCl3, and dry with argon.

4. Linking SATP-Labeled Antibody to Tips.

   (1) Incubate the tips in 50 μl of SATP-antibody, 25 μl of NH2OH reagent (500 mM NH2OH HCl/25 mM EDTA, pH 7.5), and 50 μl of buffer A for 1 h.

   (2) Wash tips with buffer A and PBS buffer (150 mM NaCl/5 mM Na2HPO4, pH 7.5) three times. Store tips in PBS buffer at 4 °C.

BIBLIOGRAPHY

[1] G. Binning, C. F. Quate, and C. Gerber. Atomic force microscope. *Phys. Rev. Lett.*, 56(9):930–933, 1986.

[2] E. Henderson. Imaging of living cells by atomic firce microscopy. *Prog. Surf. Sci.*, 46:39–60, 1994.

[3] G. M. Whitesides and B. Grzybowski. Self-assembly at all scales. *Science*, 295:2418–2421, 2002.

[4] R. D. Piner, J. Zhu, F. Xu, S. Hong, and C.A. Mirkin. "dip-pen" nanolithography. *Science*, 283:661–663, 1999.

[5] P. Avouris, T. Hertel, and R. Martel. Atomic force microscope tip-induced local oxidation of silicon: kinetics, mechanism, and nanofabrication. *Appl. Phys. Lett.*, 71:285–287, 1997.

[6] D. Eigler and E. K. Schweizer. Positioning single atoms with a scanning tunnelling microscope. *Nature*, 344:524–526, 1990.

[7] Y. Kim and C. M. Lieber. Machining oxide thin films with an atomic force microscope: pattern and objective formation on the nanometer scale. *Science*, 257(5068):375–377, 1992.

[8] R. Luthi, E. Meyer, H. Haefke, L. Howald, W. Gutmannsbauer, and H.-J. Guntherodt. Sled-type motion on the nanometer scale: Determination of dissipation and cohesive energies of c_{60}. *Science*, 266(5193):1979–1981, 1994.

[9] D. M. Schaefer, R. Reifenberger, A. Patil, and R. P. Andres. Fabrication of two-dimensional arrays of nanometer-size clusters with the atomic force microscope. *Appl. Phys. Lett.*, 66:1012–1014, Feb. 1995.

[10] T. Junno, K. Deppert, L. Montelius, and L. Samuelson. Controlled manipulation of nanoparticles with an atomic force microscope. *Appl. Phys. Lett.*, 66(26):3627–3629, June 1995.

[11] A. A. G. Requicha, C. Baur, A. Bugacov, B. C. Gazen, B. Koel, A. Madhukar, T. R. Ramachandran, R. Resch, and P. Will. Nanorobotic assembly of two-dimensional structures. In *Proc. IEEE Int. Conf. Robotics and Automation*, pages 3368–3374, Leuven, Belgium, May 1998.

[12] L. T. Hansen, A. Kuhle, A. H. Sorensen, J. Bohr, and P. E. Lindelof. A technique for positioning nanoparticles using an atomic force microscope. *Nanotechnology*, 9:337–342, 1998.

[13] M. Sitti and H. Hashimoto. Tele-nanorobotics using atomic force microscope. In *Proc. IEEE Int. Conf. Intelligent Robots and Systems*, pages 1739–1746, Victoria, B. C., Canada, October 1998.

[14] M. Guthold, M. R. Falvo, W. G. Matthews, S. washburn S. Paulson, and D. A. Erie. Controlled manipulation of molecular samples with the nanomanipulator. *IEEE/ASME Trans. on Mechatronics*, 5(2):189–198, June 2000.

[15] C. A. J. Putman, K. O. van der Werf, B. G. de Grooth, N. F. van Hulst, and J. Greve. Viscoelasticity of living cells allows high resolution imaging by tapping mode atomic force microscopy. *Biophys. J.*, 67:1749–1753, 1994.

[16] H. X. You and L. Yu. Atomic force microscopy imaging of living cells: progress, problems and propects. *Methods in Cell Science*, 21:1–17, 1999.

[17] H.-J. Butt, E. K. Wolff, S. A. C. Gould, B. D. Northern, C. M. Peterson, and P. K. Hansma. Imaging the cells with the atomic force microscope. *J. Struct. Biol.*, 105:54–61, 1990.

[18] C. B. Prater, M. R. Wilson, J. Garnaes, J. Massie, V. B. Eling, , and P. K. Hasma. Atomic firce microscopy of biological samples at low temperature. *J. Vac Sci. Tech. B*, 9:989–991, 1991.

[19] C. L. Grimellec, E. Lesniewska, M.-C. Giocondi, E. Finot, V. Vié, and J.-P. Goudonnet. Imaging of the surface of living cells by low-force contact-mode atomic firce microscopy. *Biophys. J.*, 75:695–703, 1998.

[20] P. K. Hansma, J. P. Cleveland, M. Radmacher, D. A. Walters, P. E. Hillner, M. Bezanilla, M. Fritz, D. Vie, and H. G. Hansma. Tapping mode atomic force microscopy in liquids. *Appl. Phys. Lett.*, 64:1738–1740, 1994.

[21] T.E. Schäffer, J.P. Cleveland, F. Ohnesorge, D.A. Walters, and P.K. Hansma. Studies of atomic force microscope cantilevers in liquid. *J. Appl. Phys.*, 80:3662–3667, Oct. 1996.

[22] S. Kumar and J.H. Hoh. Probing the machinery of intracellular traffiking with the atomic force microscope. *Traffic*, 2:746–756, 2001.

[23] D. Fotiadis, S. Scheuring, S. A. Müller, A. Engel, and D. J. Müller. Imaging and manipulation of biological structures with the afm. *Micron*, 33:385–397, 2002.

[24] R. Ros, F. Schwesinger, D. Anselmetti, M. Kubon, R. Schäfer, A. Plückthun, and L. Tiefenauer. Antigen binding forces of individually addressed single-chain fv antibody molecules. *Proc. Natl. Acad. Sci. USA*, 95:7402–7405, June 1998.

[25] A. A. Baker, W. Helbert, J. Sugiyama, and M. J. Miles. New insight into cellulose structure by atomic force microscopy shows the i_α crystal phase at near-atomic resolution. *Biophys. J.*, 79:1139–1145, 2000.

[26] E. L. Florin, V. T. Moy, and H. E. Gaub. Adhesion forces between individual ligand-receptor pairs. *Sciene*, 264:415–417, Apr. 1994.

[27] G. U. Lee, D. A. Kidwell, and R. J. Colton. Sensing discrete streptavidin-biotin interactions with atomic force microscopy. *Langmuir*, 10:354–357, 1994.

[28] P. Hinterdofer, W. Baumgartner, H. J. Gruber, K. Schilcher, and H. Schilcher. Detection and localization of individual antibody-antigen recognition events by atomic force microscopy. *Proc. Natl. Acad. Sci. USA*, 93:3477–3481, Apr. 1996.

[29] V. T. Moy, E. L. Florin, and H. E. Gaub. Intermolecular forces and energies between ligands and receptors. *Sciene*, 266:257–259, Oct. 1994.

[30] O. H. Willemsen, M. M. E. Snel A. Cambi, J. Greve, B. G., and C. G. Figdor. Biomolecular interactions measured by atomic force microscopy. *Biophys. J.*, 79:3267–3281, 2000.

[31] M. Ludwig, W. Dettmann, and H. E. Gaub. Afm imaging contrast based on molecular recognition. *Biophys. J.*, 72:445–448, 1997.

[32] J. P. Cleveland, B. Anczykowski, A. E. Schmid, and V. B. Elings. Energy dissipation in tapping-mode scanning force microscopy. *Appl. Phys. Lett.*, 72(20):2613–2615, 1998.

[33] J. Tamayo and R. Garcia. Relationship between phase shift and energy dissipation in tapping-mode scanning force microscopy. *Appl. Phys. Lett.*, 73(20):2926–2928, 1998.

[34] P. J. James, M. Antognozzi, J. Tamayo, T. J. McMaster, J. M. Newton, and M. J. Miles. Interpretation of contrast in tapping mode afm and shear force microscopy. a study of nafion. *Langmuir*, 17:349–360, 2001.

[35] A. Raab, W. Han, D. Badt, S. J. Smith-Gill, S. M. Lindsay, H. Schindler, and P. Hinterdorfer. Antibody recognition imaging by force microscopy. *Nat. Biotechnol.*, 17:902–905, Sep. 1999.

[36] C. Stroh, H. Wang, R. Bash, B. Ashcroft, J. Nelson, H. Gruber, D. Lohr, S. M. Lindsay, and P. Hinterdorfer. Single-molecule recognition imaging microscopy. *Proc. Natl. Acad. Sci. USA*, 101(34):12503–12507, Aug. 2004.

[37] T.R. Albrecht and C.F. Quate. Atomic resolution imaging of a nonconductor by atomic force microscopy. *J. Appl. Phys.*, 62:2599–2602, 1987.

[38] T.R. Albrecht, S. Akamine, T.E. Carver, and C.F. Quate. Microfabrication of cantilever styli for the atomic force microscope. *J. Vac. Sci. Technol. A*, 8:3386–3396, 1990.

[39] G. Meyer and N.M. Amer. Novel optical approach to atomic force microscopy. *Appl. Phys. Lett.*, 53:1045–1047, 1988.

[40] S. Alexander, L. Hellemans, O. Marti, and et al. An atomic-resolution atomic-force microscope implemented using an optical lever. *J. Appl. Phys.*, 65:164–167, 1989.

[41] G. Meyer and N.M. Amer. Simultaneous measurement of lateral and normal forces with an optical-beam-deflection atomic force microscope. *Appl. Phys. Lett.*, 57:2089–2091, 1990.

[42] J. L. Hutter and J. Bechhoefer. Calibration of atomic-force microscope tips. *Rev. Sci. Instrum.*, 64:1868–1873, 1993.

[43] J. P. Cleveland, S. Manne, D. Bocek, and P. K. Hansma. A nondestructive method for determing the spring constant of cantilevers for scanning force microscopy. *Rev. Sci. Instrum.*, 64(2):3967–3969, 1993.

[44] J. E. Sader, J. W. M. Chon, and P. Mulvaney. Calibration of rectangular atomic force microscope cantilever. *Rev. Sci. Instrum.*, 70(10):403–405, 1999.

[45] R. G. Cain, M. G. Reitsma, S. Biggs, and N. W. Page. Quantitative comparison of three calibration techniques for the lateral force microscope. *Rev. Sci. Instrum.*, 72:3304–3312, 2001.

[46] E. Liu, B. Blanpain, and J. P. Celis. Calibration procedures for frictional measurements with a lateral force microscope. *Wear*, 192:141–150, 1996.

[47] R. G. Cain, S. Biggs, and N. W. Page. Force calibration in lateral force microscope. *Journal of Colloid and Interface Science*, 227:55–65, 2000.

[48] D. F. Ogletree, R. W. Carpick, and M. Salmeron. Calibration of frictional forces in atomic force microscopy. *Rev. Sci. Instrum.*, 67:3298–3306, 1996.

[49] B. Aruk, H. Hashimoto, and M. Sitti. Man-machine interface for micro/nano manipulation with afm probe. In *Proc. IEEE Int. Conf. Nanotechnology*, pages 151–156, Hawaii, Oct. 2001.

[50] B. Mokaberi and A. A. G. Requicha. Towards automatic nanomanipulation: drift compensation in scanning probe microscopes. In *Proc. IEEE Int. Conf. Robotics and Automation)*, pages 416–421, New Orleans, April 2004.

[51] S.R.Manalis, S. C. Minne, and C. F. Quate. Atomic force microscopy for high speed imaging using cantilevers with an integrated actuator and sensor. *Applied Physics Letters*, 68:871–873, 1996.

[52] T. Sulchek, S. C. Minne, J. D. Adams, D. A. Fletcher, A. Atalar, C. F. Quate, and D. M. Adderton. Dual integrated actuators for extended range high speed atomic force microscopy. *Applied Physics Letters*, 75:1637–1639, 1999.

[53] T. Sulchek, R. Hsieh, J. D. Adams, G. G. Yaralioglu, S. C. Minne, C. F. Quate, J. P. Cleveland, A. Atalar, and D. M. Adderton. High-speed tapping mode imaging with active qcontrol for atomic force microscopy. *Applied Physics Letters*, 76:1473–1475, 2000.

[54] G.Y. Li J. Zhang, N. Xi and et al. Adaptable end effector for atomic force microscopy based nanomanipulation. *IEEE T. Nanotechnology*, 5:628–642, 2006.

[55] E. Volterra and E. C. Zachmanoglou. *Dynamics of Vibrations.* Charles E. Merrill, Ohio, USA, 1965.

[56] Thomas Bailey and James E. Hubbard Jr. Distributed piezoelectric-polymer active vibration control of a cantilever beam. *J. Guidance, Control and Dynamics*, 8:605–611, 1985.

[57] S Chonan, Z W Jiang, and M Koseki. Soft-handling gripper driven by piezoceramic bimorph strips. *Smart Materials and Structures*, 5:407–414, 1996.

[58] S.B. Choi and C.H. Lee. Force tracking control of a flexible gripper driven by piezoceramic actuator. *ASME Journal of Dynamic Systems, Measurement, and Control*, 119:439–446, 1997.

[59] Dong Sun and James K. Mills. Combined pd feedback and distributed piezoelectric-polymer vibration control of a single-link flexible manipulator. In *Proc. IEEE/RSJ International Conference on Intelligent Robots and Systems*, pages 667–672, Victoria, B.C., Canada, Oct. 1998.

[60] A.N. Singh and Y.M. Ram. Dynamic absorption in a vibrating beam. *Journal of Mechanical Engineering Science*, 217:187–197, 2003.

[61] M. Sitti and H. Hashimoto. Controlled pushing of nanoparticles: modeling and experiments. *IEEE/ASME Trans. on Mechatronics*, 5:199–211, June 2000.

[62] J. Israelachvili. *Intermolecular and surface forces.* Academic Press London, London, UK, 1991.

[63] F. Arai, D. Ando, and T. Fukuda. Micro manipulation based on micro-physics: Strategy based on attractive force reduction and stress measurement. In *Proc. IEEE Int. Conf. Robotics and Automation*, pages 236–241, Pittsburgh, PA, May 1995.

[64] M. R. Falvo, R. M. Taylor, A. Helser, V. Chi, F. P. Brooks, S. Washburn, and R. Superfine. Nanometer-scale rolling and sliding of carbon nanotubes. *Nature*, 397:236–238, January 1999.

[65] H. Chen, N. Xi, W. Sheng, and Y. Chen. General framework of optimal tool trajectory planning for free-form surfaces in surface manufacturing. *Journal of Manufacturing Science and Engineering*, Feburary 2005.

[66] J. H. Makaliwe and A. A. G. Requicha. Automatic planning of nanoparticle assembly tasks. In *Proc. IEEE Int'l Symp. on Assembly and Task Planning*, pages 288–293, Fukuoka, Japan, May 2001.

[67] H. Chen, N. Xi, G.Y. Li, and M. Prokos. Automated nanomanufacturing using afm based nano robotic system. *IEEE Transactions on automation science and Technology*, 3:208–217, 2006.

[68] Y. Zhang, A. Chang, J. Cao, Q. Wang, W. Kim Y. Li, N. Morris, E. Yenilmez, J. Kong, and H. Dai. Electric-field-directed growth of aligned single-walled carbon nanotubes. *Appl. Phys. Lett.*, 79:3155–31572, 2001.

[69] M. Iqbal B. Babic and C. Schonenberger. Ambipolar field-effect transistor on as-grown single-wall carbon nanotubes. *Nanotechnology*, 14:327–331, 2003.

[70] R. Krupe, F. Hennrich, H. B. Weber, M. M. Kappes, and H. V. Lohneysen. Simultaneous deposition of metallic bundles of single-walled carbon nanotubes using ac-dielectrophoresis. *Nano Lett.*, 3(8):1019–1023, 2001.

[71] K. M. Fung, T. S. Wong, H. M. Chan, and W. J. Li. Dielectrophoretic bath fabrication of bundled carbon nanotube thermal sensors. *IEEE T. Nanotechnology*, 3:395–403, 2004.

[72] S. Uryu Y. Aoyagi A. Kanda Y. Ootuka B. W. Alphenaar K. Tsukagoshi, N. Yoneya. Carbon nanotube devices for nanoelectronics. *Physica B*, 323:107–114, 2002.

[73] M. Deshmukh, D. C. Ralph, M. Thomas, and J. Silcox. Nanofabrcation using a stencil mask. *Appl. Phys. Lett.*, 75:1631–1633, 1999.

[74] S. G. Rao, L. Huang, W. Setyawan, and S. Hong. Large-scale assembly of carbon nanotubes. *Nature*, 425:36–37, 2003.

[75] M. Hazani, F. Hennrich, M. Kappes, R. Naaman, D. Peled, V. Sidorov, and D. Shvarts. Dna-mediated self-assembly of carbon nanotube-based electronic devices. *Chem. Phys. Lett.*, 391:389–392, 2004.

[76] N.C. Seeman. Dna in a material world. *Nature*, 421:427–431, Jan. 2003.

[77] D. D. Elley and D. I. Spivey. Semiconductivity of organic substances. *Trans. Faraday Sco.*, 58:407–410, 1962.

[78] E. Wilson. Dna charge migration: no longer an issue. *Chemical & Engineering View*, 29, Jan. 2001.

[79] J. Jortner, M. Bixon, T. Langenbacher, and M. E. Michel-Beyerle. Charge transfer and transport in dna. *Proc. Natl. Acad. Sci. USA*, 95:12759, 1998.

[80] B. Giese, J. Amaudrut, A.-K. Köhler, M. Sporman, and S. Wessely. Direct observation of hole transfer through dna by hopping between adenine bases and by tunnelling. *Nature*, 412:318–320, July 2001.

[81] J. M. Warman, M. P. de Haas, and A. Rupprecht. Dna: a molecular wire? *Chem. Phys. Lett.*, 249:319–322, Feb. 1996.

[82] S. O. Kelley and J. K. Barton. Electron transfer between bases in double helical dna. *Science*, 283:375–381, Jan. 1999.

[83] P. Tran, B. Alavi, and G. Grüner. Charge transport along the λ dna double helix. *Phys. Rev. Lett.*, 85:1564–1567, Aug. 2000.

[84] C. Gómez-Navarro, F. Moreno-Herrero, P. J. de Pablo, and J. Colchero. Contactless experiments on individual dna molecules show no evidence for molecular wire behavior. *Proc. Natl. Acad. Sco. USA*, 99:8484–8487, 2002.

[85] H.-W. Fink and C. Schönenberger. Electrical conduction through dna molecules. *Nature*, 398:407–410, Apr. 1999.

[86] A. Y. Kasumov, M. Kociak, S. Guéron, and B. Reulet. Proximity-induced superconductivity in dna. *Science*, 291:280–282, Jan. 2001.

[87] R. S. Snart. The electrical properties and stability of dna to uv radiation and aromatic hydrocarbons. *Biopolymers*, 12:1493, 1973.

[88] D. Porath, A. Bezryadin, S. de Vries, and C. Dekker. Direct measurement of electrical transport through dna molecules. *Nature*, 403:635–638, Feb. 2000.

[89] L.T. Cai, H. Tabata, and T. Kawai. Probing electrical properties of oriented dna by conducting atomic force microscopy. *Nanotechnology*, 12:211–216, 2001.

[90] K.-H. Yoo, D.H. Ha, J.-O. Lee, J.W. Park, and J. Kim. Electrical conduction through poly(da)-poly(dt) and poly(dg)-poly(dc) dna molecules. *Phys. Rev. Lett.*, 87:198102, Nov. 2001.

[91] P. J. de Pablo, F. Moreno-Herrero, and J. Colchero. Absence of dc-conductivity in -λ-dna. *Phys. Rev. Lett.*, 85:4992–4995, 2000.

[92] A. J. Storm, J. van Noort, S. de Vries, and C. Dekker. Insulating behavior for dna molecules between nanoelectrodes at the 100nm length scale. *Appl. Phys. Lett.*, 79(23):3881–3883, Dec. 2001.

[93] Y. Zhang, R. H. Austin, J. Kraeft, E. C. Cox, and N. P. Ong. Insulating behavior of λ-dna on the micro scale. *Physical Review Letter*, 89:198102, 2002.

[94] A. Bensimen, A. Simon, A. Chiffaudel, V. Croquette, F. Heslot, and D. Bensimon. Alignment and sensitive detection of dna by a moving interface. *Science*, 265:2096–2098, Sep. 1994.

[95] M. Washizu and O. Kurosawa. Electrostatic manipulation of dna in microfabricated structures. *IEEE Trans. on Industry Application*, 26:1165–1172, Nov. 1990.

[96] M. Washizu, O. Kurosawa, I. Arai, S. Suzuki, and N. Shimamoto. Applications of electrostatic stretch-and-positioning of dna. *IEEE Trans. on Industry Application*, 31:447–456, May 1995.

[97] W. A. Germishuizen, C. Wälti, R. Wirtz, M. B. Johnston, M. Pepper, A. G. Davies, and A. P. J. Middelberg. Selective dielectrophoretic manipulation of surface-immobilized dna molecules. *Nanotechnology*, 14:896–902, 2003.

[98] H. Yokota, F. Johnson, H. Lu, R. M. Robinson, and *et al.* A new method for straightening dna molecules for opitcal restriction mapping. *Phys. Rev. Lett.*, 87:198102, Nov. 2001.

[99] K. Hirano, Y. Baba, Y. Matsuzawa, and A. Mizuno. Manipulation of single coiled dna molecules by laser clustering of microparticles. *Appl. Phys. Lett.*, 80(3):515–517, Jan. 2002.

[100] T. Muir, E. Morales, J. Root, and I. Kumar. The morphology of duplex and quadruplex dna on mica. *J. Vac. Sci. Tech. A*, 16(3):1172–1177, May/Jun 1998.

[101] A. Y. Kasumov, D. V. Klinov, P.-E. Roche, S. Guéron, and H. Bouchiat. Thickness and low-temperature conductivity of dna molecules. *Appl. Phys. Lett.*, 84:1007–1009, Feb. 2004.

[102] C. Bustamante, J. F. Marko, E. D. Siggia, and S. Smith. Entropic elasticity of λ-phage dna. *Science*, 256(5178):1599–1600, 1994.

[103] G. Y. Li, N. Xi, M. Yu, and W. K. Fung. Modeling of 3-d interactive forces in nanomanipulation. In *Proc. IEEE Int. Conf. Intelligent Robots and Systems*, pages 2127–2132, Las Vegas, NV, Oct. 28-30 2003.

[104] K. W. Hipps. It's all about contact. *Science*, 294:536–537, Oct. 2001.

[105] W. Han, S. Lindsay, and J. Tianwei. A magnetic driven oscillating probe microscope for operation in liquids. *Appl. Phys. Lett.*, 69:4111–4113, 1996.

[106] A. Buguin, O. Du Roure, and P. Silberzan. Active atomic force microscopy cantilevers for imaging in liquids. *Appl. Phys. Lett.*, 78:2982–2984, 2001.

[107] E. Florin, M. Radmacher, B. Fleck, and H. Gaub. Adhesion forces between individual ligand-receptor pairs. *Rev. Sci. Instrum*, 65:639–643, 1994.

[108] I. Revendo and R. Proksch. Magnetic and acoustic tapping mode microscopy of liquid phase phospholipid bilayer and dna molecules. *J. Appl. Phys.*, 87(1):526–533, 2000.

[109] L. Schmitt, M. Ludwig, H. E. Gaub, and R. Tampe. A metal-chelating microscopy tip as a new toolbox for single-molecule experiments by atomic force microscopy. *Biophys. J.*, 78:3275–3285, June 2000.

[110] J. Fritz, A. G. Katopodis, F. Kolbinger, and D. Anselmetti. Force-mediated kinetics of single p-selection/ligand complexes observed by atomic force microscopy. *Proc. Natl. Acad. Sci. USA*, 95:12283–122888, Oct. 1998.

[111] O. H. Willemsen, M. M. E. Snel K. O. van der Werf, B. G. de Grooth, J. Greve, P. Hinterdorfer, H. J. Gruber, H. Schindler, Y. van Kooyk, and C. G. Figdor. Simultaneous height and adhesion imaging of antibody-antigen interactions by atomic force microscopy. *Biophys. J.*, 75:2220–2228, Nov. 1998.

[112] B. Bunnemann, K. Fuxe, and D. Ganten. The rennin-angiotensin system in the brain: an update 1993. *Regul. Pept.*, 46:487–509, 1993.

[113] W. F. Ganong. Blood, pituitary and brain rennin-angiotensin systems and regulation of secretion of anterior pituitary gland. *Front. Neuroendocrinol.*, 14(3):232–249, 1993.

[114] F. H. Messerli, M. A. Weber, and H. R. Brunner. Angiotensin ii receptor inhibition. a new therapeutic principle. *Arch Intern Med.*, 156:1957–1965, Sep. 1996.

[115] C. I. Johnston and L. M. Burrel. Evolution of blockade of the rennin-angiotensin system. *J. Hum. Hypertens.*, 9:375–380, 1995.

[116] M. De Gaspero, S. Whitebread, M. Mele, A. S. Motani, P. J. Whitcombe, H. P. Ramjoue, and B. Kamber. Biochemical characterization of two angiotensin ii receptor subtypes in the rat. *J Cardiovasc Pharmacol*, 16:S31–S35, 1990.

[117] T. J. Murphy, R. W. Alexander, K. K. Griendling, M. S. Runge, and K. E. Bernstein. Isolation of a cdna encoding the vascular type-1 angiotensin ii receptor. *Nature*, 351:233–236, May 1991.

[118] D. F. Guo, Y. L. Sun, P. Hamet, and T. Inagami. The angiotensin ii type 1 recetor and receptor-associated proteins. *Cell Research*, 11(3):165–180, 2001.

[119] M. A. Thomas, G. Fleissner, M. Hauptfleisch, and B. Lemmer. Subcellular identification of angiotensin i/ii- and angiotensin ii (at1)-receptor-immunoreactivity in the central nervous system of rats. *Brain Res.*, 962:92–104, 2003.

[120] M. A. Thomas, G. Fleissner, M. Stöhr, Hauptfleisch, and B. Lemmer. Localization of components of the rennin-angiotensin system in the suprachiasmatic nucleus of normotensive sprague-dawley rats part b. angiotensin ii (at1)-receptors, a light and electron microscopic study. *Brain Res.*, 1008:224–235, 2004.

[121] Y. Liu, A. Wang, and R.O. Claus. Layer-by-layer electrostatic self-assembly of nano-scale fe_3o_4 particles and polyimide precursor on silicon and silica surface. *Appl. Phys. Lett.*, 71:2265–2267, 1997.

[122] C. Lu, C. Luo, and W. Cao. Self-assembly of a covalently attached magnetic film from diazoresin and fe_3o_4 nanoparticles. *J. Mater. Chem*, 13:382–384, 2003.